On the origin and evolution of the asteroid Ryugu: A comprehensive geochemical perspective

By Eizo NAKAMURA,[*1,†] Katsura KOBAYASHI,[*1] Ryoji TANAKA,[*1] Tak KUNIHIRO,[*1]
Hiroshi KITAGAWA,[*1] Christian POTISZIL,[*1] Tsutomu OTA,[*1] Chie SAKAGUCHI,[*1]
Masahiro YAMANAKA,[*1] Dilan M. RATNAYAKE,[*1] Havishk TRIPATHI,[*1] Rahul KUMAR,[*1]
Maya-Liliana AVRAMESCU,[*1] Hidehisa TSUCHIDA,[*1] Yusuke YACHI,[*1] Hitoshi MIURA,[*2]
Masanao ABE,[*3,*4] Ryota FUKAI,[*3] Shizuho FURUYA,[*3,*5] Kentaro HATAKEDA,[*3] Tasuku HAYASHI,[*3]
Yuya HITOMI,[*3,*6] Kazuya KUMAGAI,[*3,*6] Akiko MIYAZAKI,[*3] Aiko NAKATO,[*3]
Masahiro NISHIMURA,[*3] Tatsuaki OKADA,[*3,*5] Hiromichi SOEJIMA,[*3,*6] Seiji SUGITA,[*5,*7]
Ayako SUZUKI,[*3,*6,⁑] Tomohiro USUI,[*3] Toru YADA,[*3] Daiki YAMAMOTO,[*3] Kasumi YOGATA,[*3]
Miwa YOSHITAKE,[*3,‡] Masahiko ARAKAWA,[*8] Atsushi FUJII,[*3] Masahiko HAYAKAWA,[*3]
Naoyuki HIRATA,[*8] Naru HIRATA,[*9] Rie HONDA,[*10] Chikatoshi HONDA,[*9] Satoshi HOSODA,[*3]
Yu-ichi IIJIMA,[*3,#] Hitoshi IKEDA,[*11] Masateru ISHIGURO,[*12] Yoshiaki ISHIHARA,[*3]
Takahiro IWATA,[*3,*4] Kosuke KAWAHARA,[*3] Shota KIKUCHI,[*3,*7] Kohei KITAZATO,[*9]
Koji MATSUMOTO,[*13] Moe MATSUOKA,[*3,*14] Tatsuhiro MICHIKAMI,[*15] Yuya MIMASU,[*3]
Akira MIURA,[*3] Tomokatsu MOROTA,[*16] Satoru NAKAZAWA,[*3] Noriyuki NAMIKI,[*13]
Hirotomo NODA,[*13] Rina NOGUCHI,[*3,*17] Naoko OGAWA,[*3,*18] Kazunori OGAWA,[*3]
Chisato OKAMOTO,[*8,#] Go ONO,[*11] Masanobu OZAKI,[*3] Takanao SAIKI,[*3] Naoya SAKATANI,[*19]
Hirotaka SAWADA,[*3] Hiroki SENSHU,[*7] Yuri SHIMAKI,[*3] Kei SHIRAI,[*3,*8] Yuto TAKEI,[*3]
Hiroshi TAKEUCHI,[*3] Satoshi TANAKA,[*3,*4,*20] Eri TATSUMI,[*5,*21] Fuyuto TERUI,[*3,*22]
Ryudo TSUKIZAKI,[*3] Koji WADA,[*7] Manabu YAMADA,[*7] Tetsuya YAMADA,[*3] Yukio YAMAMOTO,[*3]
Hajime YANO,[*3] Yasuhiro YOKOTA,[*3] Keisuke YOSHIHARA,[*3] Makoto YOSHIKAWA,[*3,*4]
Kent YOSHIKAWA,[*11] Masaki FUJIMOTO,[*3] Sei-ichiro WATANABE[*16] and Yuichi TSUDA[*3,*5]

(Edited by Ikuo KUSHIRO, M.J.A.; Communicated by Yoshio FUKAO, M.J.A.)

Abstract: Presented here are the observations and interpretations from a comprehensive analysis of 16 representative particles returned from the C-type asteroid Ryugu by the Hayabusa2 mission. On average Ryugu particles consist of 50% phyllosilicate matrix, 41% porosity and 9% minor phases, including organic matter. The abundances of 70 elements from the particles are in close agreement with those of CI chondrites. Bulk Ryugu particles show higher δ^{18}O, Δ^{17}O, and ε^{54}Cr values than CI chondrites. As such, Ryugu sampled the most primitive and least-thermally processed protosolar nebula reservoirs. Such a finding is consistent with multi-scale H-C-N isotopic compositions that are compatible with an origin for Ryugu organic matter within both the protosolar nebula and the interstellar medium. The analytical data obtained here, suggests that complex soluble organic matter formed during aqueous alteration on the Ryugu progenitor planetesimal (several 10's of km), <2.6 Myr after CAI formation. Subsequently, the Ryugu progenitor planetesimal was fragmented and evolved into the current asteroid Ryugu through sublimation.

Keywords: sample return, Hayabusa2, Ryugu, interstellar medium, protosolar nebula, comprehensive analysis

doi: 10.2183/pjab.98.015

1. Introduction

Sample return missions represent great opportunities to study materials from known locations on the targeted extraterrestrial body. The Hayabusa mission returned material to Earth from the asteroid Itokawa in 2010. The geochemistry and micropetrography of the returned material revealed that it is genetically related to ordinary chondrite meteorites, and that the surface of the modern-day asteroid is being actively bombarded by hypervelocity small particles.*e.g.,* 1),2) The Hayabusa2 mission returned material to Earth from the asteroid Ryugu on the 6th of December, 2020.3) Based on the very low geometric albedo indicated by remote observations,4),5) it was suggested that abundant organic matter (OM) on Ryugu might be expected.6) The initial uncontaminated and non-destructive observations for the entire set of returned samples from the Phase-1 Curation at the Extraterrestrial Sample Curation Center, ISAS, JAXA (P1C),7) demonstrated that Hayabusa2 retrieved representative and unprocessed (albeit slightly fragmented) Ryugu particles. The data further expanded on the indications from the remote sensing observations that Ryugu is dominated by hydrous carbonaceous chondrite-like materials, similar to CI chondrites.

This paper presents the observations and interpretations from a comprehensive analysis of 16 representative particles returned from the C-type asteroid Ryugu, performed at the Hayabusa2 Phase-2 Curation facility at the Pheasant Memorial Laboratory (P2C-PML), Institute for Planetary Materials, Okayama University at Misasa. In this study, the following analyses were performed: density measurement; petrological and mineralogical descriptions; elemental, isotopic, chronological and organic analyses of bulk particles; *in situ* elemental, isotopic, and chronological analyses; 2D mapping of elements,

---

[*1] The Pheasant Memorial Laboratory for Geochemistry and Cosmochemistry, Institute for Planetary Materials, Okayama University, Misasa, Tottori, Japan.

[*2] Department of Information and Basic Science, Nagoya City University, Nagoya, Aichi, Japan.

[*3] Institute of Space and Astronautical Science, Japan Aerospace Exploration Agency, Sagamihara, Kanagawa, Japan.

[*4] The Graduate University for Advanced Studies (SOKENDAI), Hayama, Kanagawa, Japan.

[*5] Graduate School of Science, The University of Tokyo, Tokyo, Japan.

[*6] Marine Works Japan, Ltd., Yokosuka, Kanagawa, Japan.

[*7] Planetary Exploration Research Center (PERC), Chiba Institute of Technology, Narashino, Chiba, Japan.

[*8] Graduate School of Science, Kobe University, Kobe, Hyogo, Japan.

[*9] Faculty of Computer Science and Engineering, The University of Aizu, Aizu-Wakamatsu, Fukushima, Japan.

[*10] Faculty of Science and Technology, Kochi University, Kochi, Japan.

[*11] Research and Development Directorate, JAXA, Sagamihara, Kanagawa, Japan.

[*12] Department of Physics and Astronomy, Seoul National University, Seoul, Korea.

[*13] National Astronomical Observatory of Japan, Mitaka, Tokyo, Japan.

[*14] Observatoire de Paris, Meudon, France.

[*15] Faculty of Engineering, Kindai University, Higashi-Hiroshima, Hiroshima, Japan.

[*16] Graduate School of Environmental Studies, Nagoya University, Nagoya, Aichi, Japan.

[*17] Faculty of Science, Niigata University, Niigata, Japan.

[*18] JAXA Space Exploration Center, Japan Aerospace Exploration Agency, Sagamihara, Kanagawa, Japan.

[*19] College of Science, Rikkyo University, Tokyo, Japan.

[*20] The University of Tokyo, Kashiwa, Chiba, Japan.

[*21] Instituto de Astrofisica de Canarias, University of La Laguna, Tenerife, Spain.

[*22] Faculty of Engineering, Kanagawa Institute of Technology, Atsugi, Kanagawa, Japan.

[#] the deceased.

[⁑] Present address: Toyo University, Tokyo, Japan.

[‡] Present address: Japan Patent Office, Tokyo, Japan.

[†] Correspondence should be addressed to: E. Nakamura, The Pheasant Memorial Laboratory for Geochemistry and Cosmochemistry, Institute for Planetary Materials, Okayama University, 827 Yamada, Misasa, Tottori 682-0193, Japan (e-mail: eizonak@gmail.com).

Non-standard abbreviation list: AOA: amoeboid olivine aggregate; BSE: back-scattered electron; CAI: calcium-aluminum-rich inclusion; CAM-H: the small monitor camera; CRE: cosmic ray exposure; DESI: desorption electrospray ionization; EC: enstatite chondrite; EIC: extracted ion chromatogram; FTIR: Fourier transform infrared spectrometry; FWHM: full width at half maximum; GCR: galactic-cosmic ray; HMT: hexamethylenetetramine; HREE: heavy rare earth elements; HR-SIMS: high-resolution secondary ion mass spectrometry; ICP-MS: inductively coupled plasma mass spectrometry; IDPs: interplanetary dust particles; IOM: insoluble organic matter; IRMS: isotope ratio mass spectrometry; ISM: interstellar medium; LOM: labile organic matter; LREE: light rare earth element; Ma: million years ago; MREE: middle rare earth elements; MS: mass spectrometry; MS/MS: tandem mass spectrometry; MSWD: mean square weighted deviation; OC: ordinary chondrite; OM: organic matter; ONC-T: the optical navigation camera telescope; ONC-W1: the optical navigation camera for a wide-angle nadir view; OT-MS: orbitrap-mass spectrometry; P1C: Phase-1 Curation at ESCuC (the Extraterrestrial Sample Curation Center, ISAS, JAXA); P2C-PML: Phase-2 Curation facility at the Pheasant Memorial Laboratory; PAH: polycyclic aromatic hydrocarbon; PML: The Pheasant Memorial Laboratory; PSN: protosolar nebula; RC: R chondrite; REE: rare earth elements; ROM: refractory organic matter; SCI: small carry-on impactor; SCR: solar-cosmic ray; SEM: scanning electron microscopy; SIMS: secondary ion mass spectrometry; SOM: soluble organic matter; SW: solar wind; TC: total carbon; TD1: first touchdown; TD2: second touchdown; TEM: transmission electron microscopy; TIMS: thermal ionization mass spectrometry; TNR: trans-Neptunian region; TOC: total organic carbon.

isotopes, the Raman spectrum, and organic compounds; and compound-specific analysis of OM. The findings of the current comprehensive study will provide a guide for future investigations of Ryugu particles.

Based on the comprehensive data set obtained in this study, the authors will answer the science goals that were determined as the aims of the Hayabusa2 mission.[8)] The aims include understanding the origin and evolution of materials in the asteroid Ryugu and the early solar nebula, and constraining the physical properties of planetesimals during the planetary accretion process. Furthermore, the main goal has been set to elucidate the origin of water in the Earth and organic matter as a building block of life because the particles returned from Ryugu are expected to be entirely free from contamination from the Earth's environment.

2. An overview of the surface characteristics of Ryugu and the sampling sites

Watanabe *et al.*[9)] and Sugita *et al.*[5)] first reported the results of remote-sensing observations on the near-Earth C-type asteroid Ryugu. The data obtained, which had been conducted by the multiple instruments onboard the Hayabusa2 spacecraft, revealed the shape, mass and geomorphology of Ryugu. Ryugu has an oblate "spinning top" shape associated with a prominent circular equatorial ridge, an equatorial radius of 502 m and a polar-to-equatorial axis ratio of 0.82, resulting in a volume of $0.377\,\mathrm{km}^3$. The mass estimated by the gravity measurement is $4.50 \times 10^{11}\,\mathrm{kg}$ giving a bulk density of $1190\,\mathrm{kg\,m}^{-3}$.

Due to the high porosity and the large boulders on the surface of Ryugu, the interior was considered to consist of boulders that were weakly agglomerated gravitationally,[9)] similar to Itokawa as investigated by the preceding Hayabusa mission.[10)] It has been proposed that such a rubble-pile structure was formed by the re-accumulation of collisional debris after a catastrophic collision between larger asteroids.[11),12)] Many impact craters with a diameter of up to 200 m were found on the surface.[5),13)] The age estimated from the crater-size frequency distributions indicates that the 1 m thick surface layer was formed within the last six million years (Myr).[5)] The geometric albedo obtained by the photometric measurements is similar to the albedo of a typical comet[14)] and characteristic of the darkest Cb-type asteroid.[5)] The global map of the spectral b-x slope indicates that the area near the center of the ridge is predominantly blue, with a red spectral slope seeming to predominate as the distance from the ridge increases (Fig. 1a in ref. 13). This feature would suggest that mass wasting after spin-down of Ryugu exposed fresh subsurface materials on the equatorial ridge.[9)] As described below, Hayabusa2 succeeded in sampling two points on the surface of Ryugu, ~870 m apart, near the equator.

2.1. Sampling by the first touchdown (TD1). On the 22nd of February 2019, the first sampling by the Hayabusa2 spacecraft was carried out during its touchdown on the surface of Ryugu at 4.30°N and 206.47°E of the equatorial region. The touchdown site was dominated by an area that had a slightly bluish spectral slope, compared to the more reddish features which are increasingly dominant towards the mid-latitude region, based on the surface color quantified using the spectral slope from the *b*-band (0.48 µm) to the *x*-band (0.86 µm).[5),9),13)] Hayabusa2's thrusters disturbed the surface, revealing dark material immediately after touchdown, probably because the reddish fine regolith was blown away.[13)] The movie of the touchdown maneuver by Hayabusa2 was clearly recorded by the onboard small monitor camera (CAM-H) (https://www.hayabusa2.jaxa.jp/en/galleries/movie/pages/td1-l08e1_cam-h_movie_190222_speedx5.html). The camera footage allowed an investigation of the surface response to the physical disturbances caused by the touchdown, including the projectile collision and the firing of the spacecraft's thruster gas jets.[13)] The surface just before the touchdown appears to be covered with slab-like rock fragments. At the same time as the tip of the sampler horn with a diameter of 0.2 m touched the surface of Ryugu, a tantalum metal bullet was fired to destroy the surface. The sample fragments were concentrated through the sampling horn and stored in sample chamber-A. Hayabusa2 photographed the disturbed surface of Ryugu via the optical navigation camera for a wide-angle nadir view (ONC-W1), from approximately 30 m above the surface immediately after the touchdown (https://www.hayabusa2.jaxa.jp/en/galleries/ryugu/pages/fig28_touchdown.html), and showed that the surface became darker than the surrounding area following the maneuver. This indicates that the subsurface materials of Ryugu are darker than the surface as discussed elsewhere.[6)]

2.2. Sampling by the second touchdown (TD2). The second touchdown operation was designed to collect the subsurface materials near an artificial crater, formed by a small carry-on impactor

(SCI).[15] During the SCI impact operation, which was undertaken on the 5th of April 2019, a 2 kg copper projectile was fired at a velocity of 2 $\mathrm{km\,s^{-1}}$ and successfully impacted the asteroid surface to form an artificial crater at 7.9°N and 313.3°E, in the northern part of Ryugu's equatorial ridge. This operation successfully created a semi-inverted conical crater with a rim-to-rim diameter of 17.6 m, a rim height of ∼0.4 m around the crater, an apparent diameter of 14.5 m and a pit point depth of 1.7 m from the initial surface.[16)–18)]

The low-velocity materials ejected, from the crater formed by the SCI, were deposited around the crater. The difference in the optical navigation camera telescope (ONC-T) v-band (0.55 µm) reflectance before and after the SCI impact indicated the exposure of subsurface materials and ejecta deposited outside of the crater. This change was observed only in and very near the crater within 2R (R is referred to as the radius of the crater, 7.25 m).[16] Based on the observation of the SCI crater wall, Arakawa *et al.*[16] inferred that the subsurface layer is dominated by regolith with rock sizes smaller than 0.2 m.

On the 11th of July 2019, Hayabusa2 succeeded in collecting samples from an area 0.2 m in diameter, through an amazingly precise landing at 10.130°N and 300.595°E.[19] Looking at the video taken with the CAM-H just before TD2, the boulders that make up the surface layer are more gravel-like than slab-like (https://www.hayabusa2.jaxa.jp/en/galleries/movie/pages/CAMH_PPTD_Timelapse_full_x1020190726.html), in comparison to TD1. The distance of the TD2 sampling point from the SCI crater center was measured to be 22 m, equivalent to 3R,[19),20)] and thus it is too far for the Hayabusa2 spacecraft to detect the change in ONC-T v-band reflectance before and after the SCI impact. However, Honda *et al.*[20] investigated resurfacing processes caused by the ejected materials from the artificial crater and revealed that the number of new boulders decreased with increasing distance from the crater center. The change in the thickness of the ejecta layer as a function of the distance from the crater was also calculated. As a result, the ejecta thickness was found to change from 0.3 m at the crater rim to ∼50 mm at 13 m from the crater center and further decrease to ∼1 mm at 30 m.

Arakawa *et al.*[21] made a preliminarily estimate of the ratio of the samples recovered from the top 50 mm of the surface at different distances, from 7.5 to 15 m from the impact point, assuming the formation of a crater radius of 5 m. The TD2 site is 22 m from the center of the SCI crater, with the crater radius being 7.5 m. It was revealed that the sample may be recovered from not only the ejecta deposit, but also the pre-impact surface below the deposit, when the ejecta thickness is thinner than 50 mm at 15 m from the crater center. The crater radius of the actual SCI experiment, carried out on the surface of Ryugu, was larger than that of the simulation experiment. When the larger crater radius is taken into account, it is expected that the ejected/original volume ratio in the sample collected by Hayabusa2 (at 22 m from the crater center) is similar to the simulation ratio calculated for 15 m from the crater center. Accordingly, the sample collected by TD2 is expected to consist of an SCI ejecta deposit to pre-impact basement ratio of ∼1:3 and should have been collected from a maximum depth of ∼1.3 m.[21]

3. Samples and analytical protocol

The 16 Ryugu particles, comprising a total of 55 mg, selected by P1C[7] were transferred to the ultimate clean room (nominal class: ISO 6; measured class: ISO 3–4) of the P2C-PML, specifically designed for handling Ryugu particles. The selected particles comprised seven from chamber A collected by TD1 (A0022, A0033, A0035, A0048, A0073, A0078, and A0085) and nine from chamber C collected by TD2 (C0008, C0019, C0027, C0039, C0047, C0053, C0079, C0081, and C0082) (Table S1 and Fig. 1). In this paper, particles from chambers A and C are denoted as TD1 and TD2 particles, respectively. At the P2C-PML the following analyses were performed using the analytical protocol shown in Fig. SA1: petrological, mineralogical, OM distribution and *in situ* elemental, isotopic and chronological analyses were obtained from X-ray diffraction (XRD), optical, scanning and transmission electron microscopy (SEM and TEM), micro-Raman and Fourier transform infrared spectroscopy (FTIR), desorption electrospray ionization-orbitrap-mass spectrometry (DESI-OT-MS) and secondary ion mass spectrometry (SIMS and HR-SIMS). Bulk elemental and isotopic analyses were determined via thermal ionization (TIMS), inductively coupled plasma (ICP-MS), isotope ratio mass spectrometry (IRMS) and noble gas mass spectrometry (noble gas MS). Compound-specific OM analysis was carried out using ultra-high-performance liquid chromatography-orbitrap-mass spectrometry (UHPLC-OT-MS). Artificial surfaces and sample powders were simultaneously prepared using an ultra-microtome instru-

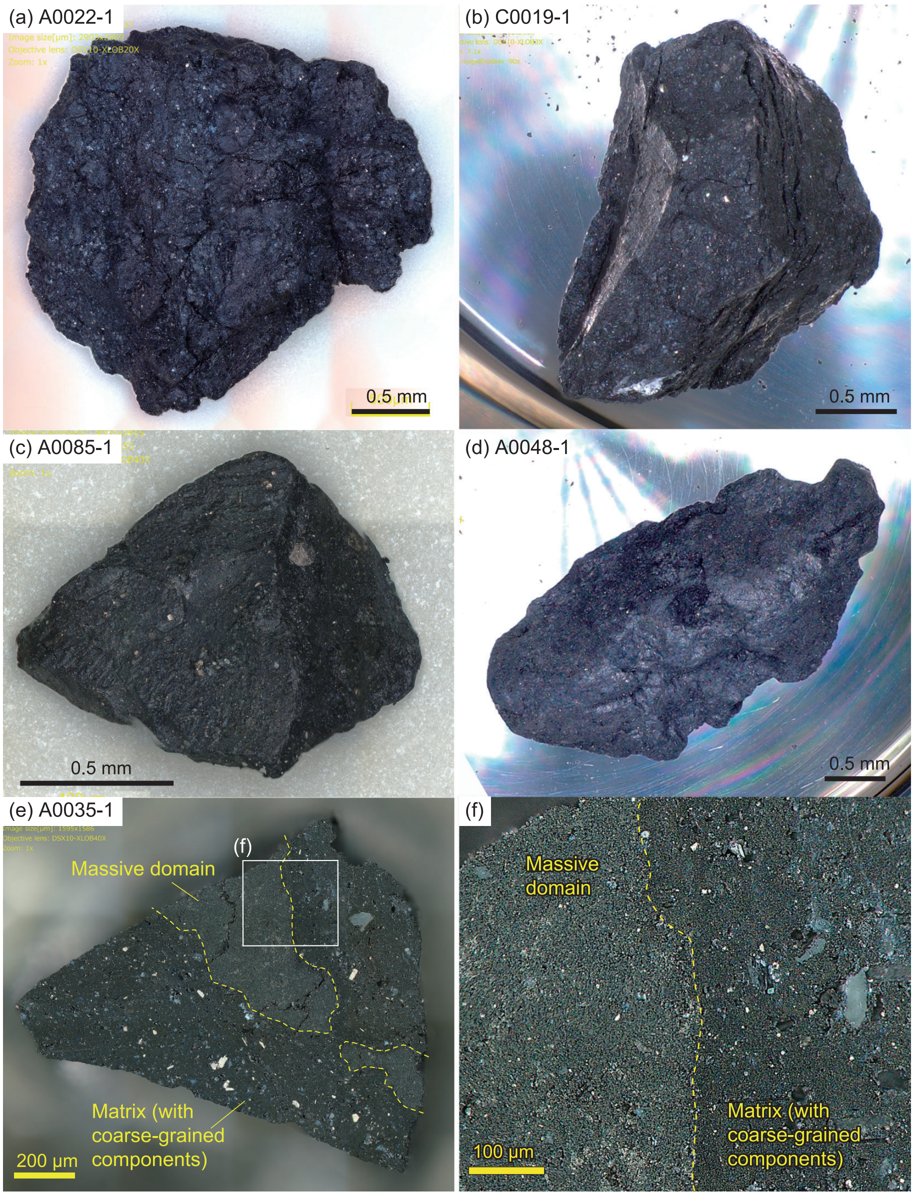

Fig. 1. Optical microscope images showing the surface and interior features. (a) A grain with a rugged and finely-cracked surface morphology. (b) A comparatively solid grain with planar fractures. (c) A solid grain with a smooth surface morphology. (d) A solid grain with a curved and smooth surface morphology. (e) The internal texture on the flat surface of A0035-1 prepared by ultramicrotome. The particle is characterized by components up to several 10's of μm in size, which are encapsulated in a fine-grained 'matrix' that is dominated by phyllosilicates. A unique distinctive domain is present within A0035 (surrounded by dashed lines). The domain is massive in nature with more fine-grained components than the surrounding areas and includes abundant Fe-sulfide and no coarse-grained components. As such, this domain is termed the 'massive domain'. (f) An enlarged view of the rectangle in (e). The massive domain is separated by a curved boundary (dashed lines) from the surrounding matrix.

ment, equipped with a diamond knife. Each analytical procedure is described in the Supplementary Text. Note that sub-aliquots of particles are indicated by the particle number followed by a hyphen and number.

4. Results

4.1. Textural and phase description. To understand the physicochemical characteristics of the 16 particles, we observed both the natural and artificial surfaces of the particles at the mm- to nm-

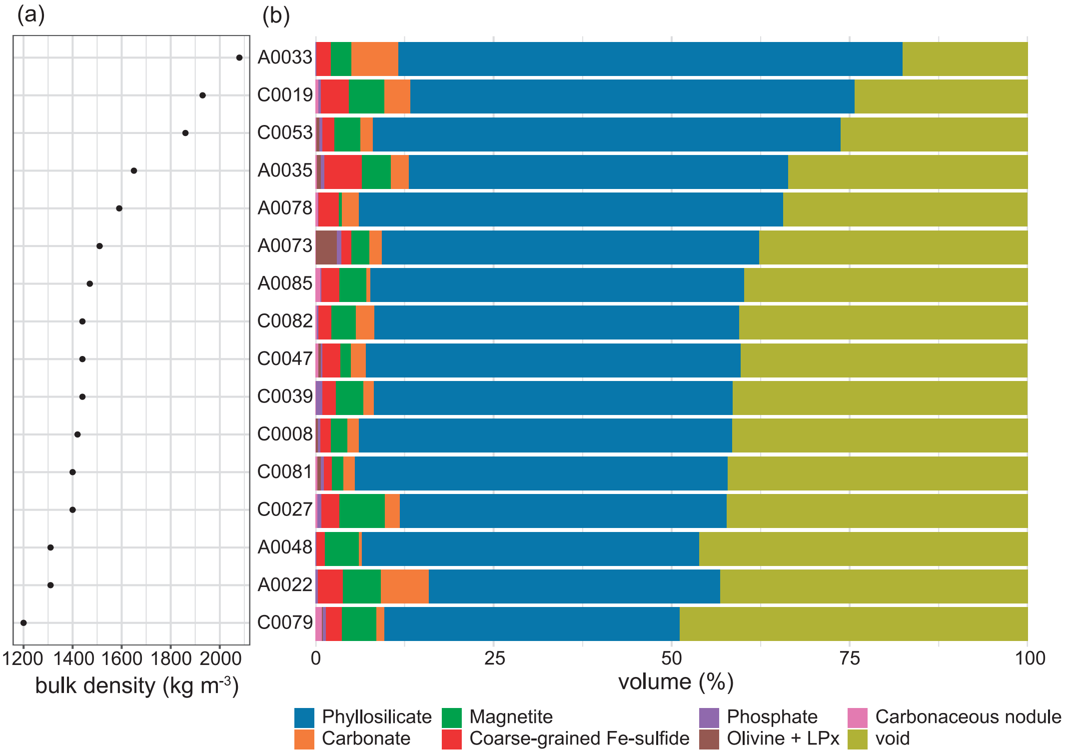

Fig. 2. The (a) bulk densities and (b) modal abundances of major components including void space. Major components include phyllosilicate, carbonate, magnetite, coarse-grained Fe-sulfide, phosphate, olivine + low-Ca pyroxene (LPx), and carbonaceous nodule.

scales (Figs. 1 and SA2), and analyzed the elemental abundances and isotopic compositions of the components in the particles. In addition, when combining the observations and the analytical data it was possible to estimate the modal abundances of all the components (Fig. 2 and Tables S2 and S3) and to produce a map illustrating their distribution (phase map; Fig. SB1–24) for each particle. The details are described below.

4.1.1. Petrology and mineralogy. All 16 particles appear very dark to the naked eye, but vary in appearance, with two main styles of surface morphology present. The first style has a rough, irregular surface and is finely cracked, which results in particles with this morphology being fragile in nature (Fig. 1a). Some particles developed parallel, nearly planar cracks (Fig. 1b). This texture implies that these particles were formed by agglomeration of regolith material at either the surface of Ryugu or within its progenitor body and subsequently inherited by Ryugu. The second style is surrounded by a smooth surface without significant cracks, which makes particles with this morphology less fragile. The surface of particles with the second morphological style is also often striated (Fig. 1c) with a distinctive luster (Fig. 1d). Both styles are recognized irrespective of the sampling site and the particle size.

The Ryugu particles are composed of predominantly fine-grained 'matrix' with numerous several micrometer (µm) to sub-µm-sized voids that surround coarse-grained components of 10's of µm to ~100 µm in size (Fig. 3). Such a texture is observed in the particles from both sampling sites and thus appears to be representative of Ryugu particles.

The matrix occupies ~90% of the particles excluding void space and its modal abundance does not differ between TD1 (88 ± 3 vol%, 1SD) and TD2 (82 ± 9 vol%) particles (Fig. 2). The matrix is predominantly composed of phyllosilicate, of the inter-layered smectite-group and serpentine-group minerals (Figs. 4c and SA3), which were confirmed by using scanning TEM and XRD. The matrix also includes sub-µm-sized OM (nano-OM), Fe-sulfide, carbonate and phosphate minerals and irregularly shaped µm to sub-µm-sized interstitial voids

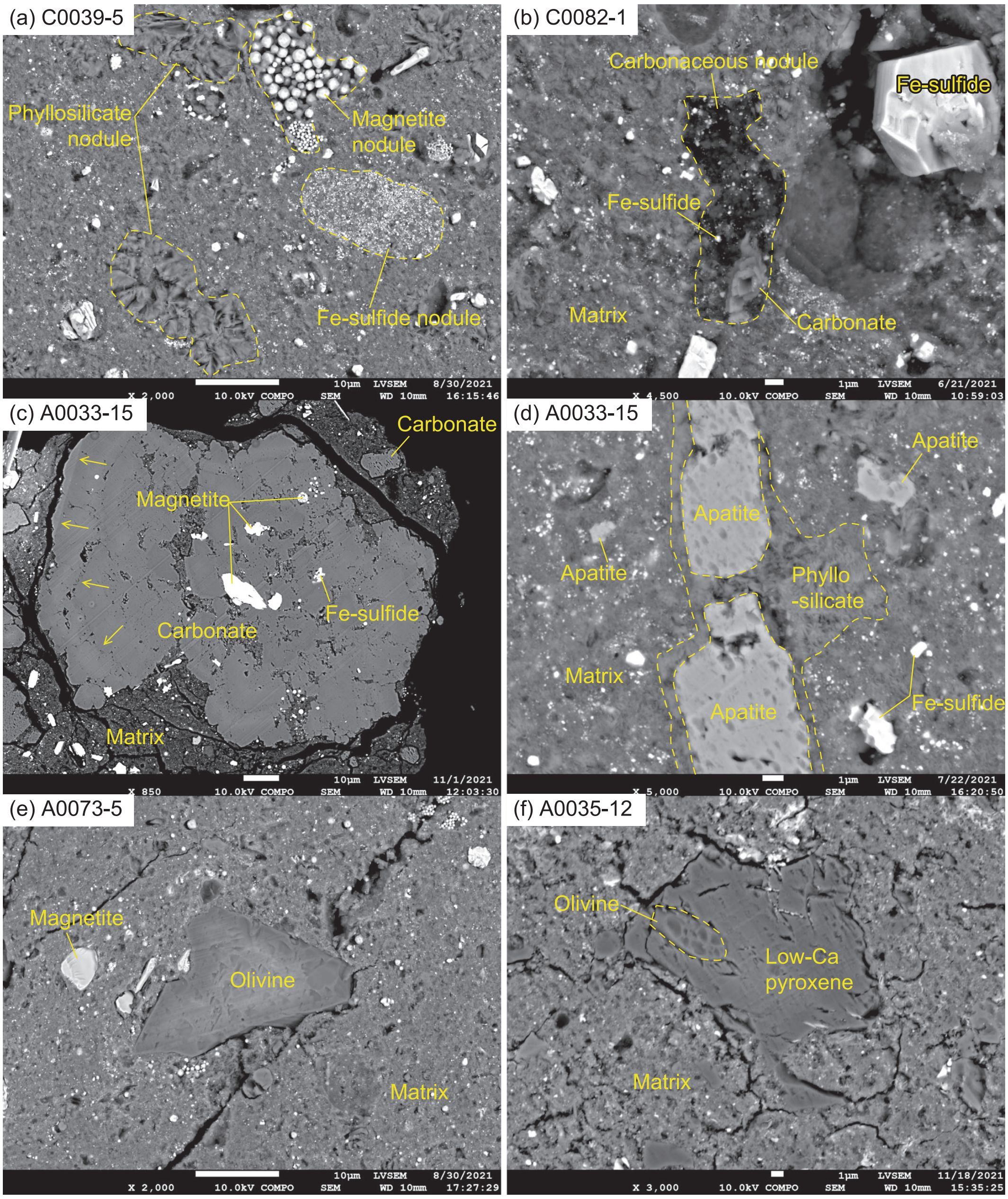

Fig. 3. The modes of occurrences of coarse-grained components. (a) Phyllosilicate nodules, a framboidal magnetite nodule, and a Fe-sulfide nodule. (b) A carbonaceous nodule, associated with a carbonate crystal and Fe-sulfides. (c) A coarse-grained carbonate nodule, with magnetite- and Fe-sulfide-inclusions at the core, and concentric chemical zonation (shown by arrows) at the rim. (d) Apatite crystals wrapped in a phyllosilicate film. (e) An angular fragment of olivine, where the surface is slightly altered by the ultra-microtome operation, causing the occurrence of fish-scale-like chips. Note that the olivine appears to be bright at the core due to charging. The chemical composition differs little between the core and the margin of the grain. (f) A composite grain of low-Ca pyroxene and olivine.

(Fig. 4a). Phyllosilicates are sometimes found arranged in the µm to sub-µm-sized yarn ball-like spheres (Fig. 4a). Such a texture could represent nucleation and growth features associated with phyllosilicates, but it may also represent pseudomorphs after the alteration of amorphous silicate grains. Both soluble and insoluble OM (SOM and IOM, respectively) are widely distributed in the

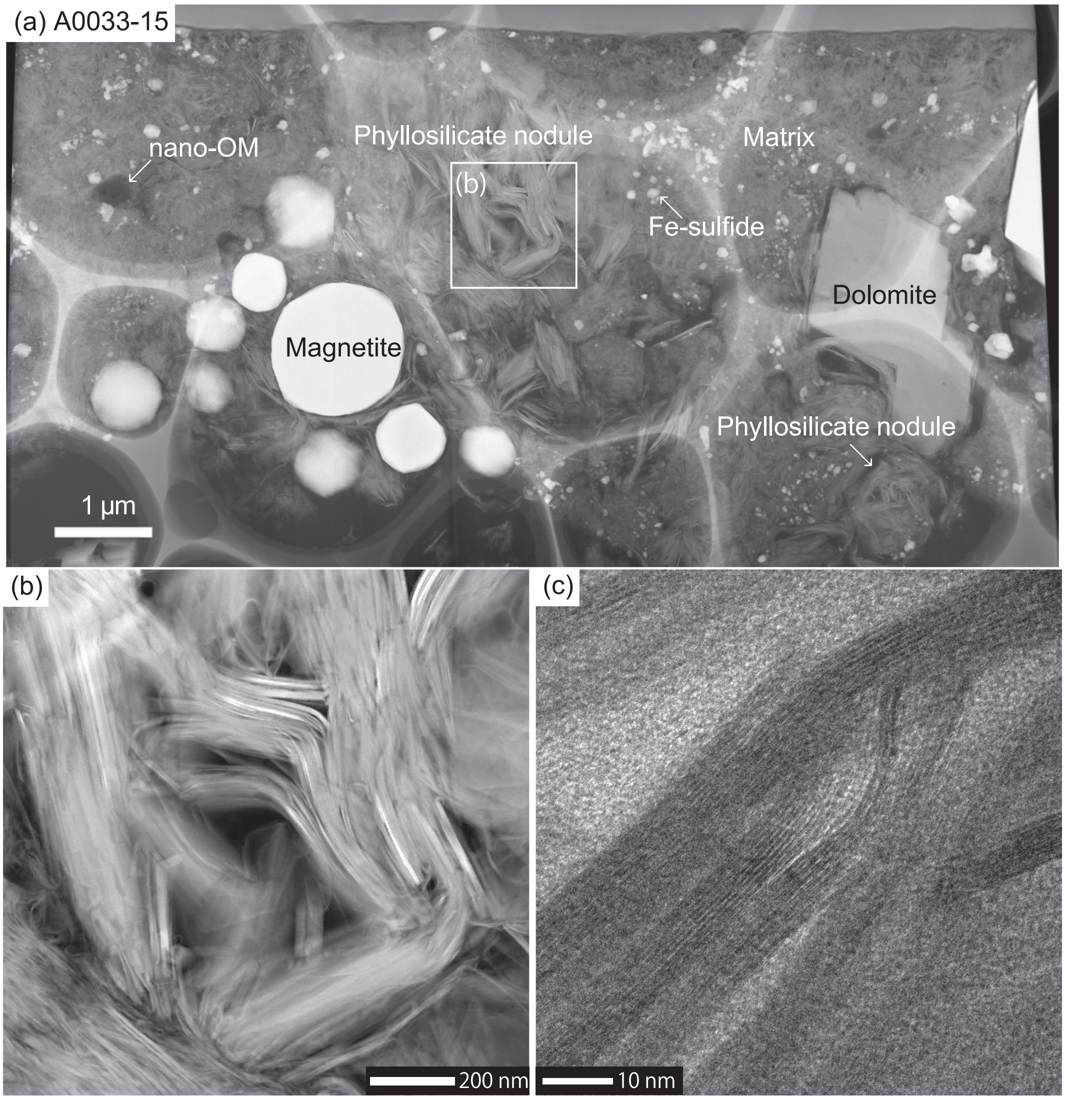

Fig. 4. Scanning TEM images of a film of matrix from A0033-15, prepared by a focused ion beam. (a) A whole view of the film. Besides the μm-sized magnetite and dolomite and phyllosilicate nodules, a nano-OM and Fe-sulfides are widespread in the matrix, which is composed mainly of fine-grained phyllosilicates. The phyllosilicate nodule sometimes forms μm to sub-μm-sized yarn ball-like spheres (shown at the lower right of the image). (b) An enlarged view of a μm-sized phyllosilicate nodule. (c) A high-resolution view of the phyllosilicate. The width of the interlayers is ∼0.75 nm, corresponding to that of a Fe-bearing serpentine-group mineral.

matrix, as indicated by micro-Raman spectroscopy and DESI-OT-MS, which are described later.

The coarse-grained components are isolated from the matrix with sharp boundaries, and their modal abundances reach up to ∼15 vol%. Such components can be mono-phase or poly-phase in nature. The mono-phase components are aggregates or grains consisting of a single mineral which can include phyllosilicate (both serpentine- and smectite-group minerals occur together), carbonate, phosphate, Fe-sulfide, magnetite, olivine, or pyroxene (Figs. 3a, 3e, and 5e). The poly-phase components are nodular aggregates (hereafter referred to as nodules) of OM, Fe-sulfides, carbonates, and magnetite (Figs. 3b, 6d, and SA2b), and these nodules are often accompanied by phyllosilicates. Neither refractory components, such as Ca-Al-rich inclusions (CAI), nor chondrules were found in the particles examined by textural observation. But the relicts retaining their O isotope signatures were detected as described later. In the following paragraphs, we describe the components and then their constituents.

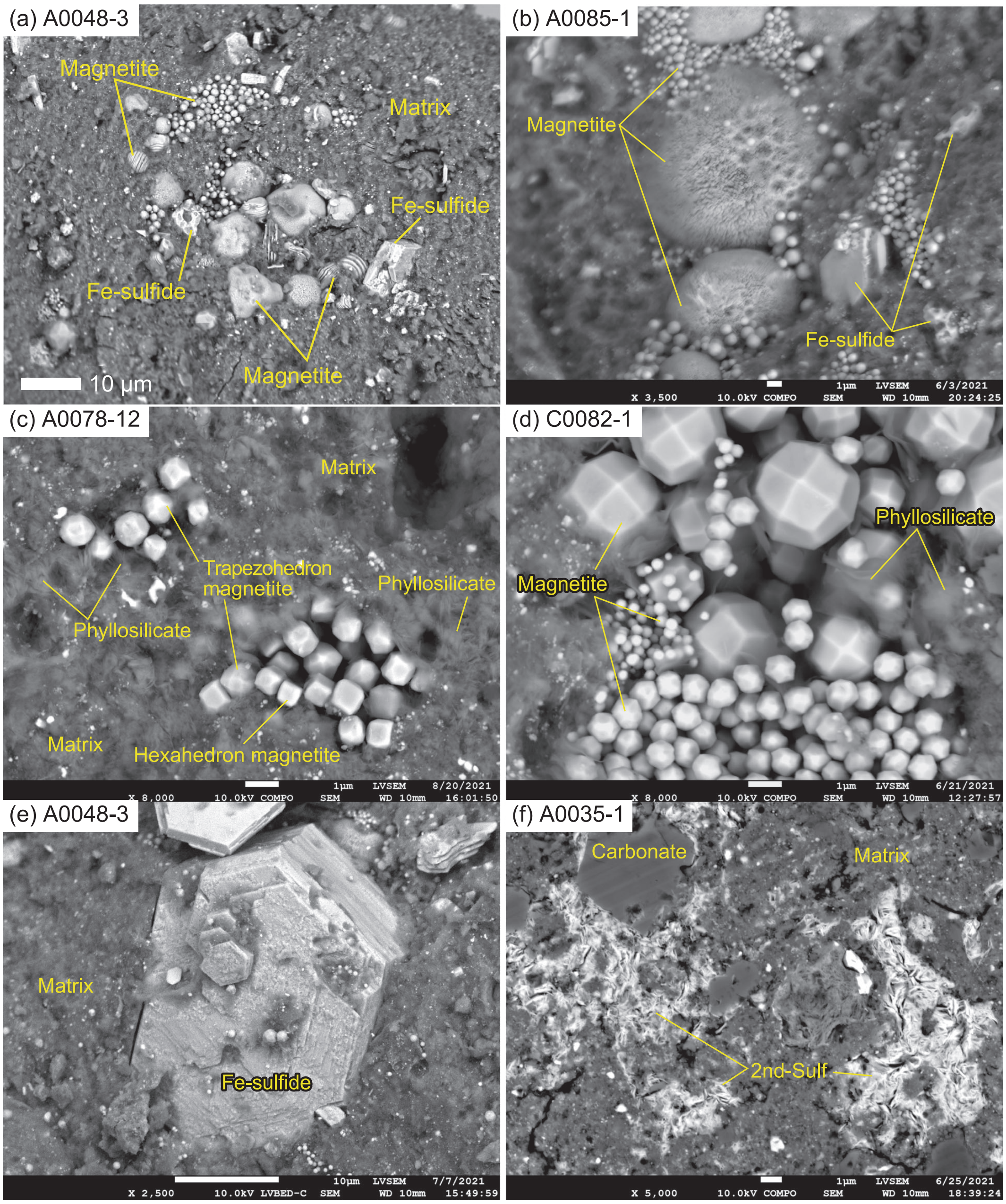

Fig. 5. The modes of occurrences of the coarse-grained components in Ryugu particles. (a) A cluster of magnetite showing various forms. (b) An enlarged view of a spherical magnetite. A spherulic magnetite represents a radial aggregate of nm-sized needle-like magnetite grains. On the surface of the magnetite there are µm-sized circular pits, which correspond to the shape of adjoining framboidal magnetite. (c) Framboidal magnetite grains, accompanied by phyllosilicate. The hexahedron magnetite grains (cube-shaped) occur as relatively small grains, with larger trapezohedron magnetite grains (high number of facets) occurring within several-µm, as shown toward the lower right of the image. (d) Clusters of framboidal magnetite grains. Irrespective of their size, the trapezohedron crystal faces are well developed. (e) A Fe-sulfide grain exhibiting well-developed crystal faces. (f) Secondary Fe-sulfides (2nd-Sulf), surrounding a carbonate grain and infilling micro-cracks in a matrix.

Carbonaceous nodules are identical in their mineral assemblage to the matrix, but enriched in OM (Figs. 3b and 6c). In the nodules, OM occurs also as micrometer- or nanometer-sized aggregates with sharp boundaries (micro-OM or nano-OM; Figs. 4a and 7a).

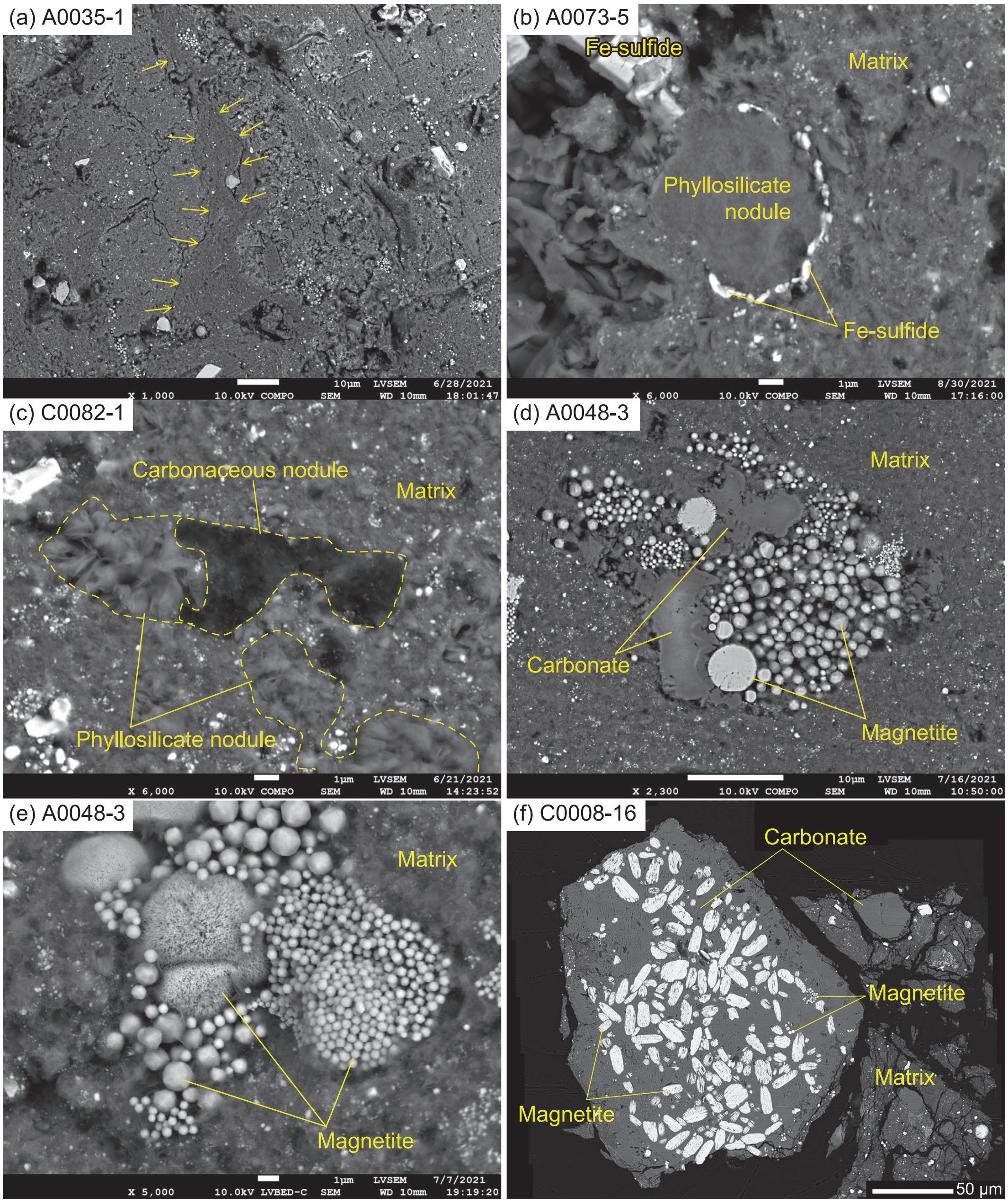

Fig. 6. The different textures recorded by the matrix and the modes of occurrences of the coarse-grained components. (a) The phyllosilicate-dominated matrix. Note that there are locally-foliated domains (shown by arrows) in the matrix surrounding the massive domain. (b) A phyllosilicate nodule, surrounded by Fe-sulfide, in a phyllosilicate-dominated matrix. (c) A composite of a carbonaceous nodule and a phyllosilicate nodule. (d) A magnetite nodule with various forms of magnetite. (e) A magnetite nodule with spherical and framboidal magnetite grains. Note that framboidal magnetite grains which vary in size coexist in a single nodule. (f) A magnetite carbonate nodule, which includes platy and framboidal magnetite grains.

Iron-sulfide nodules are highly enriched in Fe-sulfide grains (Fig. 3a), but otherwise identical in their mineral assemblage to the matrix. Iron-sulfides that often occur within the Fe-sulfide nodules, but which also occur independently, exhibit at least three modes of occurrence. The first type occurs as a coarse-grained crystal (a few to several 10's of µm in size). In most cases, the first type exhibits an euhedral shape in the matrix (Fig. 5e), but some are observed as an inclusion in the coarse-grained carbonate nodule

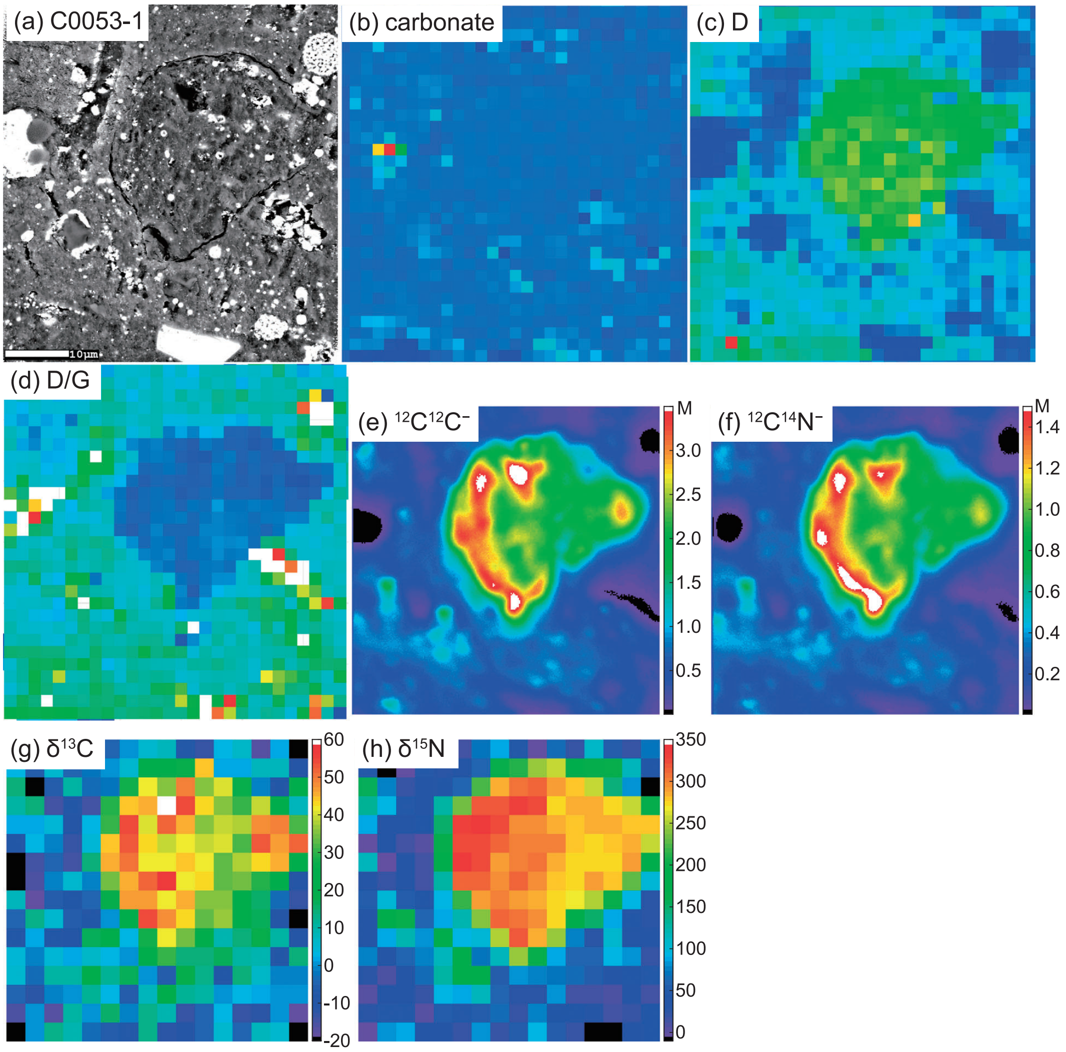

Fig. 7. A carbonaceous nodule in the matrix of C0053-1. (a) BSE image, (b) Raman carbonate band (1098 cm^{-1}) map, (c) Raman D-band map, and (d) Raman D/G map, (e) $^{12}C^{12}C^-$ map, (f) $^{12}C^{14}N^-$ map, (g) $\delta^{13}C$ map, and (h) $\delta^{15}N$ map from SIMS. The presence of micro-OM inside of the nodule is suggested by an intense $^{12}C^{12}C^-$ signal.

(Fig. 3c) and occur as partially dissolved, anhedral crystals nearby the magnetite nodules (Fig. 5a). The euhedral and hexagonal-disc-shaped Fe-sulfides exhibit well-developed crystal faces (Fig. 5e), suggesting that their growth is also linked to the presence of open spaces. The second type is the most common type in the Ryugu particles, and occurs as fine-grained phases (<1 µm in size) scattered throughout the matrix (Fig. 4a), and in Fe-sulfide and carbonaceous nodules (Figs. 3a and 3b). A large number of these sub-µm-sized, Fe-sulfide grains are observed, but they were too small to estimate the modal abundance accurately. The third type is also fine-grained (<1 µm in size), but infills micro-cracks and surrounds the coarse-grained components in the matrix (Fig. 5f). We refer to this third type as "secondary". The first and second type of Fe-sulfides were observed in both TD1 and TD2 particles, but the third "secondary" type was found only in a distinct 'massive' domain of A0035, which will be described later. The modal abundance of Fe-sulfide in TD1 particles shows a larger variation (2.7 ± 1.4 vol%) than in TD2 particles (2.1 ± 0.8 vol%). The Fe-sulfides are present as pyrrhotite (major phase) and pentlandite (minor phase), with Ni/(Fe + Ni) of 0–0.14 and 0.20–0.57, respectively (Fig. SA4d). The pyrrhotite of the first type tends to occur as a coarse-grained euhedral crystal (several 10's of µm in size) compared with the pentlandite (~10 µm); some of the pyrrhotite include the pentlandite, and overgrow the euhedral crystals. In terms of geochemistry, pyrrhotite is the major reservoir of S, but makes only a minor contribution to the bulk rare earth element (REE) budget of Ryugu particles (Fig. SA5).

Phyllosilicate nodules consist of two types: the first is composed only of coarse-grained 'fluffy' phyllosilicate minerals (Figs. 3a and 4), and the other is a dense aggregate of fine-grained phyllosilicate minerals, with a fringe of Fe-sulfide grains (Fig. 6b). The 'fluffy' phyllosilicate nodule, as well as the Fe-sulfide nodules and the carbonaceous nodules, could have been formed prior to their incorporation into the matrix. Alternatively, the aforementioned nodules could have been accreted as aggregates, which were then aqueously altered and recrystallized to form the nodule without mixing with the surrounding material in the matrix. Such a scenario is preferred here, because it does not require the nodules to be previously aqueously altered and thus requires less assumptions to be made. An example of the second scenario for nodule formation is demonstrated by the dense phyllosilicate nodule in A0073-5 (Fig. 6b). The dense phyllosilicate nodule appears to have formed through recrystallization of a ~5 µm silicate grain, with formation of Fe-sulfide grains along the relict grain boundary with the matrix. Phyllosilicate nodules (Fig. 6c) and carbonate nodules (Fig. 3b) often occur next to the carbonaceous nodules, suggesting that such nodules were formed through interactions with silicate, fluid components and OM.

The matrix that is dominated by phyllosilicate has a chemical composition indicative of a serpentine-smectite mixture, which extends to a Fe-rich composition possibly due to the incorporation of sub-µm-sized Fe-rich phases (Fig. SA4a). On the other hand, the phyllosilicate nodules, without visible accessory minerals (Figs. 3a and 4), show chemical compositions that plot consistently in the Fe-poor and slightly (Si + Al)-rich region of Fig. SA4a. Phyllosilicate smectite/serpentine ratios and Mg/(Fe + Mg) ratios exhibit certain degrees of variation, but TD1 and TD2 phyllosilicates are largely consistent with each other in those ratios (Fig. SA4a). The matrix which is mainly composed of phyllosilicate exhibits trace element abundances that are almost the same as the bulk particle, but enriched in Li, Sr, Y, Zr, Nb, and Ba (Tables S4 and S5 and Fig. SA5). Whereas the phyllosilicate nodules are depleted in Sr, Y, Ba, and REE relative to the matrix. This suggests that accessory phases in the matrix, including nm-sized unidentified phases, are highly enriched in Li, Zr, Nb, and REE, or that the phyllosilicates in the nodules are different in terms of their trace element abundances from those in the matrix.

Carbonate nodules range in size from several µm to hundreds of µm, and they often contain magnetite with or without Fe-sulfide (Figs. 3c, 6d, and 6f). The modal abundances of carbonates vary more in TD1 particles (3.1 ± 2.7 vol%) than in TD2 particles (2.0 ± 0.8 vol%). There could be a negative correlation in modal abundances between carbonate nodules and carbonaceous nodules. A0022 and A0033 contain significant amounts of carbonate nodules (6.9 and 6.8 vol%) and no observable carbonaceous nodule. Meanwhile, A0085 contains small amounts of carbonate nodules (0.6 vol%), but significant carbonaceous nodules (0.7 vol%).

Carbonate in the carbonate nodules is present mainly as dolomite, and includes minor calcite and magnesite. The carbonate minerals also contain ~15 mol% of siderite component ($FeCO_3$) and ~9 mol% of rhodochrosite component ($MnCO_3$) (Fig. SA4b). Coarse-grained dolomite (~100 µm in size) exhibits concentric zonation (Fig. 3c), and its magnesite component increases toward the rim, indicating that the composition of the fluid from which it formed changed over time. The carbonate is enriched in Ba and Sr, and depleted in Li, Zr, and Nb; dolomite is enriched in REE compared to magnesite (Fig. SA5). The REE abundances vary within and among the dolomite grains; the coarse-grained dolomite (A0033-15) is depleted in REE at the rim, which is enriched in the magnesite component. Whereas in another particle (C0053-1), the dolomite, enriched in the magnesite component (Fig. SA4b), shows a light rare earth element (LREE: La–Nd) enriched pattern (Fig. SA5). Such variations among particles suggest that the fluid evolution from which the carbonates formed was also variable.

Magnetite nodules are present in various forms (Figs. 3a and 5a), and magnetite itself also shows various crystal habits: spherule, framboid, and plaquette.[22] The three habits of magnetite coexist in the matrix (Figs. 5a, 5b, 5c, and 5d), and are also found within the carbonate nodule (Fig. 3c) and the carbonate-magnetite nodule (Fig. 6f). On the surface of the spherulitic magnetite, sub-µm-sized circular pits are occasionally present (Fig. 5b). The pits correspond to the form of adjoining framboidal magnetite, and indicate that some of the framboidal magnetite grains formed through partial dissolution of the spherulitic magnetite. Such an observation indicates that the altering fluid composition varied spatially and or temporally (discussed in Section 5.2.3 in detail). The framboidal magnetite grains vary not only in size but also in crystal form (Figs. 5b, 5c, 5d, and 6e). The crystal habits of magnetite vary depending on the physicochemical environments during their crystallization.[e.g., 23)] In most cases, the magnetite grains with different forms and the framboidal magnetite with different sizes cluster at the ~10 µm-scale (Figs. 6e and 6d). At such a scale, there is no significant difference in pressure and temperature. Therefore, the magnetite nodules with different forms, and those of framboidal magnetite of different sizes and crystal habits must have formed in different chemical systems. As discussed in Section 5.2.3 in detail, the chemical systems must operate within open spaces (voids) that are filled with gas or liquid phases for magnetite to grow with well-developed crystal faces (Fig. 5d).[24)] The gas or liquid phases likely included organic matter, because solvable organic matter facilitates the formation of magnetite crystals with a high-index of facets (Figs. 5c and 5d).[25)]

No significant difference was observed in the modal abundances of magnetite between TD1 (3.4 ± 1.6 vol%) and TD2 (3.7 ± 1.7 vol%) particles. The magnetite all contain a trace amount of Ni ($\mathrm{Ni/(Fe + Ni)} \approx 0.05$, in molar ratio), irrespective of their crystal form. In addition to magnetite, rare Mn-bearing ilmenite ($\mathrm{Mn/(Fe + Mn)} \approx 0.11$) was also observed.

Phosphate minerals occur occasionally as poly-phase components with phyllosilicate and carbonate. The modal abundances of phosphates are 0.6 ± 0.5 and 0.9 ± 0.4 vol% for TD1 and TD2 particles, respectively. Both Ca-phosphate and Na-Mg-phosphate were identified (Fig. SA4c). The former is hydroxyapatite with trace amounts of halogens ([F] <0.1 wt% and [Cl] <0.2 wt%); hereafter, we simply refer to it as apatite. Apatite sometimes occurs with a phyllosilicate fringe (Fig. 3d) and appears to have formed through a process similar to the phyllosilicate nodules with coarse-grained 'fluffy' phyllosilicate (Fig. 3a). The grain size of Na-Mg-phosphate is too small to characterize it fully. Nonetheless, the position of the Raman band relating to $\mathrm{PO_4}^{3-}$ at 970 cm^{-1}, and the major element abundances of [Na_2O] 9.7 ± 1.3 (1SD), [MgO] 26.1 ± 0.6 (1SD), [P_2O_5] 44.2 ± 1.6 (1SD), and [H_2O] 19.9 wt%, suggests that the Na-Mg phosphate is mejillonesite, $\mathrm{NaMg_2(PO_3OH)(PO_4)(OH) \cdot H_5O_2}$.[26)] Where the major element abundances measured and the [H_2O] estimated, based on an ideal chemical formula, were normalized to a total of 100 wt%. Major element abundances of apatite extend toward that of merrillite, but this could be related to the small size of the targeted grains and the presence of phyllosilicates in the probed area during quantitative analysis (Fig. 3d). Apatite is the major reservoir of REE, but unlike what is commonly observed in chondrites,[27)] it shows a REE pattern, that is flat with slight enrichments of middle rare earth elements (MREE: Sm–Dy) or heavy rare earth elements (HREE: Ho–Lu), and no Eu-anomaly (Fig. SA5).

Olivine and low-Ca pyroxene occur as angular-shaped fragments (Figs. 3e and 3f), in seven out of the 16 Ryugu particles. A0073 contains abundant olivine and low-Ca pyroxene (2.9 vol%). The modal abundances of the remaining six particles are 0.4 ± 0.2 vol%. Most of the olivine and low-Ca pyroxene are in contact with the phyllosilicate-dominated matrix through smooth and sharp boundaries (Figs. 3e, SA6a, and SA6b). A rare olivine grain with an irregular surface (uneven at the sub-µm-scale) occurs in the Fe-sulfide nodule (Fig. SA6c). The olivine grain adjoins the phyllosilicate in the matrix, forming a sharp boundary, and expresses no distinct reaction rim, even at the nm-scale (Fig. SA6d). In fact, the olivine is not altered in terms of its major element abundance, and is as Mg-rich as the other olivine and low-Ca pyroxene grains with $\mathrm{Mg/(Fe + Mg)}$ of 0.97–1.0 and 0.97–0.99, respectively. The O isotopic composition determined by SIMS was $\delta^{18}\mathrm{O} = -1.1$ to -4.7‰, $\delta^{17}\mathrm{O} = -49.3$ to -6.0‰, and $\Delta^{17}\mathrm{O} = -23.3$ to -3.5‰ for olivines, and $\delta^{18}\mathrm{O} = -4.5$ to -4.3‰, $\delta^{17}\mathrm{O} = -7.8$‰, and $\Delta^{17}\mathrm{O} = -5.5$‰ for the low-Ca pyroxene (Table S6), where $\delta^{17 \text{ or } 18}\mathrm{O} = (^{17 \text{ or } 18}\mathrm{O}/^{16}\mathrm{O}_{\mathrm{sample}})/(^{17 \text{ or } 18}\mathrm{O}/^{16}\mathrm{O}_{\mathrm{VSMOW}}) - 1$ and $\Delta^{17}\mathrm{O} = \ln(\delta^{17}\mathrm{O} + 1) - 0.528 \times \ln(\delta^{18}\mathrm{O} + 1)$. The olivine grains fall into clusters with either $\delta^{18}\mathrm{O} \approx -50$‰ and $\Delta^{17}\mathrm{O} \approx -23$‰ or $\delta^{18}\mathrm{O} \approx -5$‰ and $\Delta^{17}\mathrm{O} \approx -5$‰, with all low-Ca pyroxene grains falling into the latter cluster. The O isotopic values of olivine and low-Ca pyroxene grains are distinct from that of the bulk value for all the Ryugu particles analyzed here (Fig. 8, discuss later). The O TD1 composition of clusters with $\Delta^{17}\mathrm{O} = -23$‰ and $\Delta^{17}\mathrm{O} = -5$‰ fall within the ranges exhibited by olivine grains in the amoeboid olivine aggregates (AOAs) and the chondrules of carbonaceous chondrites including their relicts, respectively.[e.g., 28),29)] The chondrule-like O isotope signature was found in olivine and low-Ca

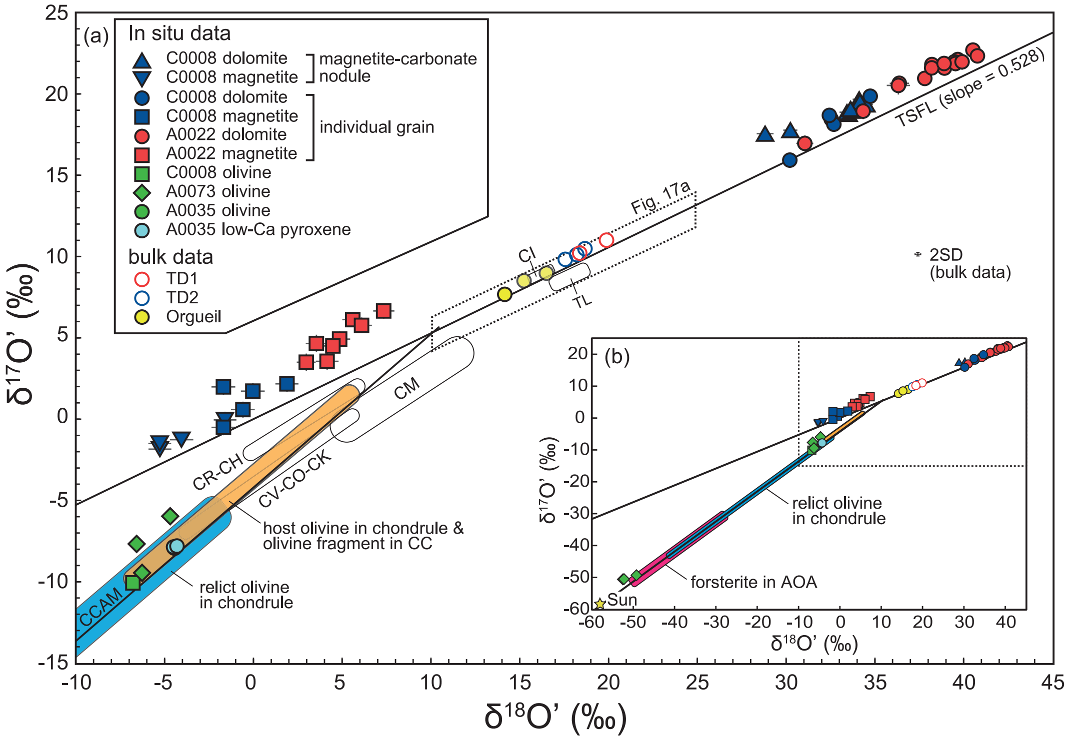

Fig. 8. The O isotopic compositions of magnetite, dolomite, olivine and low-Ca pyroxene grains and the bulk values for Ryugu particles. δ^{17}O' = ln(δ^{17}O* + 1) where δ^{17}O* = δ^{17}O + 0.033 × 10^{-3}, and δ^{18}O' = ln(δ^{18}O + 1). Compiled data for carbonaceous chondrites (CC) are from the literature.190)–194) Data for host olivines in chondrules and olivine fragments in CC are from previous studies,194)–196) data for relict olivine in CC chondrules are from the literature,197),198) and data for AOA are from a previous study.199) The error bar for bulk analysis values is 2SD. CCAM and TSFL denote carbonaceous chondrite anhydrous mineral line200) and terrestrial silicate fractionation line.201) TL is Tagish Lake (C2 ungrouped).

pyroxene grains in the matrix (Fig. SA6a), whereas the AOA-like signatures were confirmed in olivine grains in both the matrix and the Fe-sulfide nodule (Figs. SA6b and SA6c). All of the above findings indicate that the olivine and low-Ca pyroxene in the Ruygu particles were derived from chondrules or AOAs, and were physically mixed into the matrix after the major phase of aqueous alteration.

The massive domain occurs as a distinct region of the TD1 particle A0035. An aliquot of this particle, A0035-1 contains a light-colored domain (several 100's of µm in size) in the matrix with a sharp, but intricate boundary (Figs. 1e and 1f). The matrix surrounding the massive domain is locally foliated subparallel to the outline of this domain (Fig. 6a). The domain, which is rather massive and lacking in coarse-grained components larger than several 10's of µm (Fig. 1f), contains Fe-sulfide phases, carbonate, magnetite, phosphate and phyllosilicate nodules. Therefore, the components are the same as those enclosed within the typical matrix, except rare >10 µm olivine and low-Ca-pyroxene were also observed, making the massive domain unlike any components observed in the other Ryugu particles examined.

4.1.2. Density and porosity. The average bulk density of TD1 material (11 aliquots from 7 particles) and of TD2 material (10 aliquots from 9 particles) were 1539^{+166}_{-161} kg m^{-3} and 1491^{+187}_{-171} kg m^{-3} (95% of Bayesian credible interval), respectively (Fig. 2 and Table S3). The difference in the bulk density between the TD1 and TD2 particles was −31 to 285 kg m^{-3} (95% of Bayesian credible interval), with the TD1 particles being slightly denser (Fig. 9). The average bulk density of all particles yields 1528 ± 242 (1SD) kg m^{-3}, which is 246 kg m^{-3} greater than that measured at the P1C (1282 ± 231 kg m^{-3}, $n = 156$).7) The difference that is barely significant could be attributed to the different analytical methods of the bulk volume estimation. Unlike the method employed at the P1C, our method considers the actual irregularities of the particle for the determination of the bulk volume estimation (see Supplementary Text ST1.1 in detail). The average bulk density of the

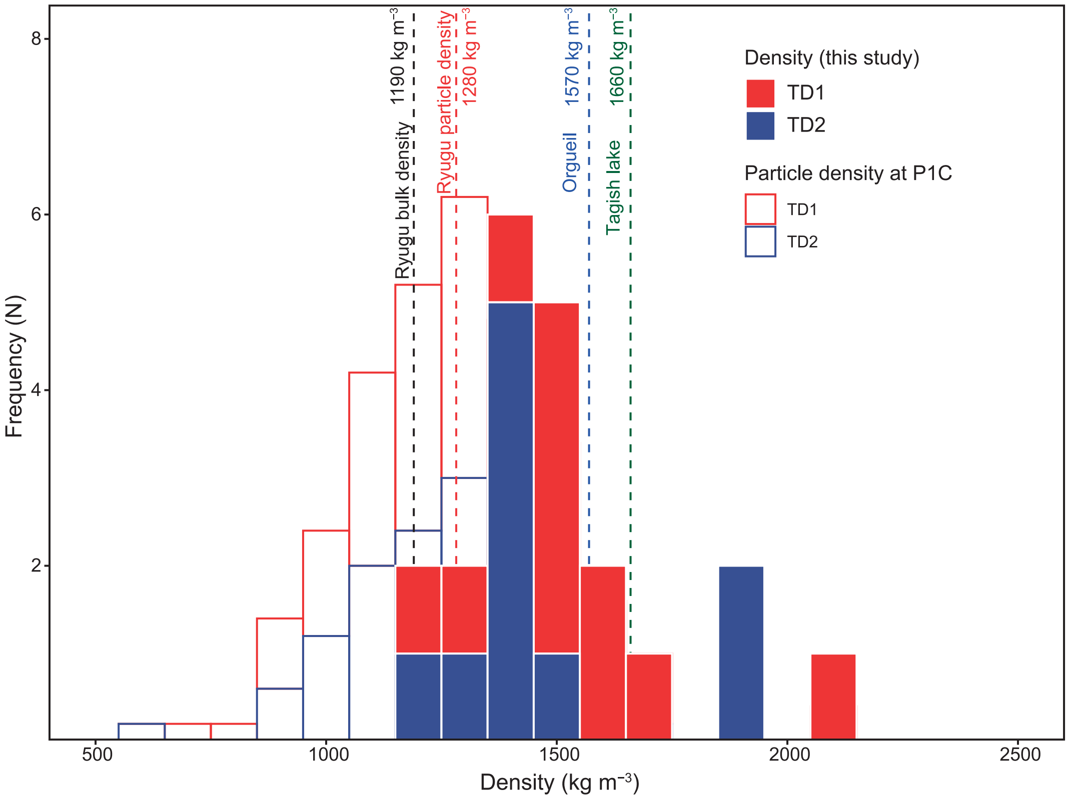

Fig. 9. Density distributions of 16 particles. The density histogram measured at the P1C[7)] is also shown. The frequency (N) of the P1C[7)] was rescaled by a factor of 0.2 to match the apparent scale. The average density of the 16 particles is 1528 ± 242 (1SD) $\mathrm{kg\,m^{-3}}$. The density difference between TD1 and TD2 particles is -32 to 143 $\mathrm{kg\,m^{-3}}$ (50% of Bayesian credible interval), suggesting that there is no significant difference between the densities of TD1 and TD2 particles. As references, Ryugu bulk density,[9)] and bulk densities of Orgueil (CI1)[30)] and Tagish Lake (C2 ungrouped)[31)] meteorites are also shown in the figure.

Ryugu particles does not differ significantly from that of the Orgueil (CI1, 1570 $\mathrm{kg\,m^{-3}}$)[30)] and Tagish Lake (C2 ungrouped, 1660 $\mathrm{kg\,m^{-3}}$).[31)]

The Ryugu particles were collected from the asteroid surface, which had been destroyed by a Ta bullet. Thus, the particles might record a higher density than the surface materials that they were derived from, because an impactor destroys a target to produce fragments, which would have separated along planes with a lower strength such as pre-existing cracks. Accordingly, the resulting fragments, namely the Ryugu particles collected, might have a relatively higher strength. Therefore, the bulk density obtained here may be higher than the typical bulk density of materials near the surface of Ryugu, including fine-grained materials such as regolith and materials with less strength.

The grain density of the Ryugu particles ranges from 2504 to 2679 $\mathrm{kg\,m^{-3}}$, with an average value of 2587^{+32}_{-32} $\mathrm{kg\,m^{-3}}$ (Table S3). The microporosity ranges between 19 and 54 vol%, with an average value of $40.9^{+5.0}_{-5.1}$ vol% (Table S3). The modal abundances of components and void are shown in Fig. 2. The microporosity is similar to that (46%) obtained by P1C.[7)] The macroporosity was estimated to be 7% using the bulk density of the asteroid Ryugu, 1190 ± 20 $\mathrm{kg\,m^{-3}}$.[9)] Using the result in this study, the macroporosity is estimated to be 22%, which may be an upper limit given the strength bias of the collected particles. Note that Grott *et al.*[32)] estimated a macroporosity of 16 ± 3% based on the size-frequency distribution of boulders on the surface of Ryugu.

4.1.3. Light-element isotope characteristics of micro-OM. The C and N isotope maps were obtained by SIMS with a scanning probe for 15 µm × 15 µm or 50 µm × 50 µm areas (Figs. 10b, 10c, 11b, and 11c). The primary beam diameter is ∼1 µm. The δ^{15}N and δ^{13}C values from the maps, as well as the average isotopic compositions of the areas, were processed pixel-by-pixel (Fig. SA7), where $\delta^{15}\mathrm{N} = (^{15}\mathrm{N}/^{14}\mathrm{N}_{\mathrm{sample}})/(^{15}\mathrm{N}/^{14}\mathrm{N}_{\mathrm{air}}) - 1$ and

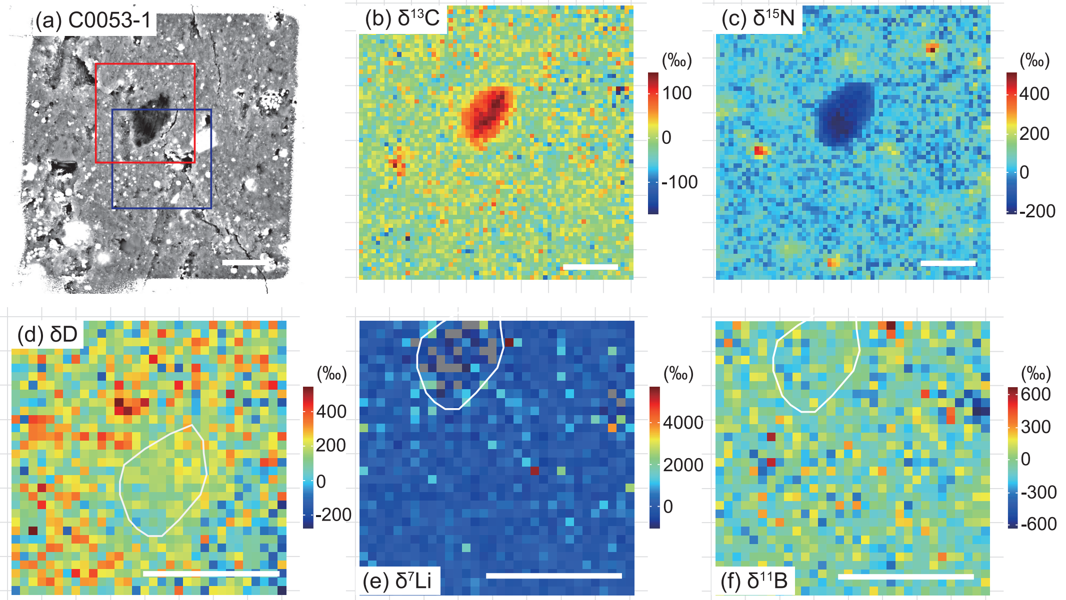

Fig. 10. C, N, H, Li, and B isotope maps of micro-OM in C0053-1. (a) BSE image. A 10 µm-sized dark object located in the center is the largest micro-OM in the area. The squares correspond to the regions where H (red) and Li and B (blue) isotope maps were obtained. (b) C isotope map. The δ^{13}C value of the largest micro-OM is 96 ± 6‰ (1SE). (c) N isotope map. The δ^{15}N value of the largest micro-OM is -147 ± 10‰ (1SE). Micrometer-sized ^{15}N-rich objects are also micro-OM, some of which exceed $\delta^{15}\mathrm{N} \approx 400$‰. (d) H isotope map. The δD value of the largest micro-OM is 158 ± 30‰ (1SE). (e) Li isotope map. The δ^{7}Li value of the largest micro-OM is 139 ± 404‰ (1SE). (f) B isotope map. The δ^{11}B value of the largest micro-OM is -33 ± 80‰ (1SE). The area corresponding to the largest micro-OM is outlined in (d), (e), and (f). The scale bar in each figure corresponds to 10 µm.

$\delta^{13}\mathrm{C} = (^{13}\mathrm{C}/^{12}\mathrm{C}_{\mathrm{sample}})/(^{13}\mathrm{C}/^{12}\mathrm{C}_{\mathrm{V\text{-}PDB}}) - 1$. The matrix effect correction was carried out so that the average C and N isotopic compositions, of matrix areas within a particle determined by SIMS, are equal to those determined by the whole-rock analysis for each particle.

The variations of the δ^{15}N and δ^{13}C values (1SD) among the 15 µm × 15 µm area analyses within the particles A0073-5, A0078-12, C0019-10, and C0053-1 are (δ^{15}N: 89.7‰, δ^{13}C: 9.9‰, $n_{\mathrm{area}} = 25$), (46.1‰, 6.6‰, $n_{\mathrm{area}} = 28$), (12.4‰, 6.5‰, $n_{\mathrm{area}} = 15$) and (16.0‰, 4.7‰, $n_{\mathrm{area}} = 37$), respectively, and those of Orgueil (CI1) are (22.0‰, 7.3‰, $n_{\mathrm{area}} = 31$), where n_{area} is the number of areas analyzed (Fig. SA7 and Table S7; Note that variation is not discussed for A0085-1 due to the small number of analysis areas). The variation of δ^{13}C values is less than 10‰ both for Ryugu and Orgueil samples. Variation of δ^{15}N values in C0019-10 and C0053-1 are smaller, and in A0073-5 and A0078-12 are larger than those of Orgueil.

The pixel-by-pixel analyses formed a cluster of data points located at the center of the bulk Ryugu particle value, with arrays deviating towards either heavy C and N or heavy C and light N compositions (Fig. SA7). The distribution of points in the main cluster is dominated by counting statistics, but the compositions of the points in the arrays reflect mixing with components with isotopically anomalous compositions. We refer to the δ^{15}N-rich and δ^{13}C-rich components as the ^{15}N-hotspot and the δ^{15}N-poor and δ^{13}C-rich components as the ^{15}N-coldspot. According to SEM imaging, the areas with elevated δ^{15}N values include micro-OM, identified as darker regions (*i.e.*, composed of lighter elements on average) than the surrounding matrix (Fig. 10a). Since micro-OM is enriched in C relative to bulk matrix, a region consisting of pixels with ion signal ratio $(^{12}\mathrm{C}^{12}\mathrm{C}^{-}/\mathrm{Si}^{-}) > 2$ is identified as micro-OM. The C and N isotopic compositions of micro-OM are shown in Figs. 10, 11, and 12 and Tables S7 and S8. From A0078-12 it is inferred that the ^{15}N-hotspot is at least as heavy as $\delta^{15}\mathrm{N} = 1131 \pm 38$‰, with $\delta^{13}\mathrm{C} = 66 \pm 38$‰. From C0053-1 it is inferred that the ^{15}N-coldspot is at least as light as $\delta^{15}\mathrm{N} = -147 \pm 10$‰, with $\delta^{13}\mathrm{C} = 96 \pm 6$‰. The δ^{15}N values determined for the area analysis could be explained by contribution from several OM components with distinct isotopic compositions, including those of the ^{15}N-

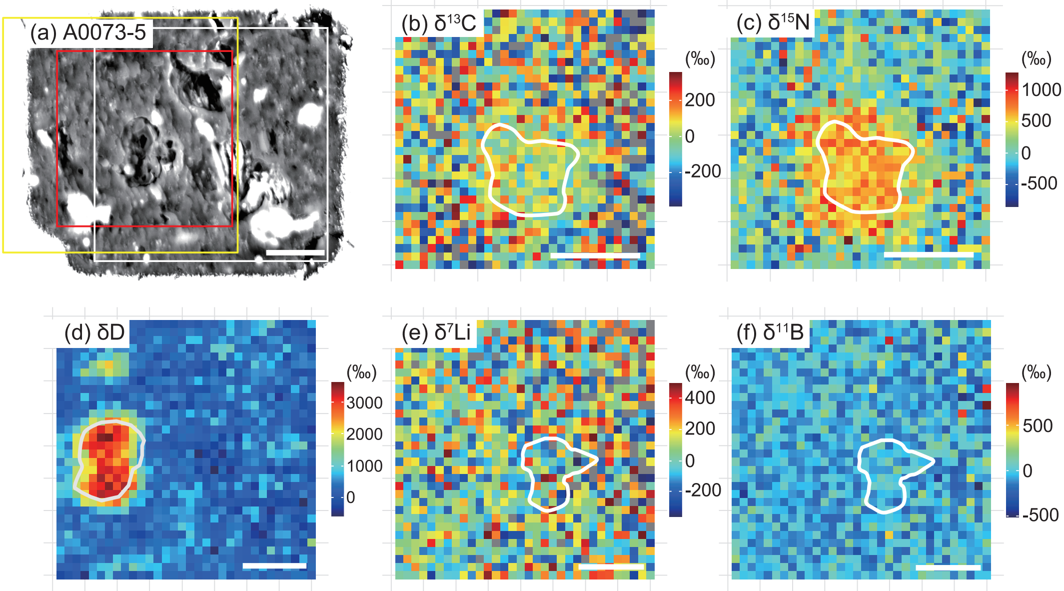

Fig. 11. C, N, H, Li, and B isotope maps of micro-OM in A0073-5. (a) BSE image. A 10 µm-sized dark object located in the center is the largest micro-OM in the area. The squares correspond to the regions where C and N (white), H (red), and Li and B (yellow) isotope maps were obtained. (b) C isotope map. The δ^{13}C value of the largest micro-OM is 27 ± 69‰ (1SE). (c) N isotope map. The δ^{15}N value of the largest micro-OM is 610 ± 78‰ (1SE). (d) H isotope map. The δD value of the largest micro-OM is 2983 ± 84‰ (1SE). (e) Li isotope map. The δ^{7}Li value of the largest micro-OM is 29 ± 568‰ (1SE). (f) B isotope map. The δ^{11}B value of the largest micro-OM is 0 ± 314‰ (1SE). The area corresponding to the largest micro-OM is outlined in (d), (e), and (f). The scale bar in each figure corresponds to 10 µm. Note that the shape of the largest micro-OM changed slightly because of spattering during analysis.

hotspots and ^{15}N-coldspots, which are much smaller than the area analyzed, and micro- and nano-OM with bulk Ryugu-like values.

Micro-OM with distinctly higher δ^{13}C values (96 ± 6‰) and lower δ^{15}N values (-147 ± 10‰) than the surrounding matrix was found in C0053-1 (Fig. 10) and is recognized here as a ^{15}N-coldspot, as described above. The BSE image of the micro-OM also confirms the presence of a sharp boundary, which separates it from the surrounding matrix. A small number of micro-OM with low δ^{15}N values are also observed in A0073-5 and A0078-12 (Fig. 12). The micro-OM (circled by the white line in Fig. 10) showed $\delta\mathrm{D} = 158 \pm 30$‰, $\delta^{7}\mathrm{Li} = 139 \pm 404$‰, and $\delta^{11}\mathrm{B} = -33 \pm 80$‰, respectively, where $\delta\mathrm{D} = (\mathrm{D}/\mathrm{H}_{\mathrm{sample}})/(\mathrm{D}/\mathrm{H}_{\mathrm{VSMOW}}) - 1$, $\delta^{7}\mathrm{Li} = (^{7}\mathrm{Li}/^{6}\mathrm{Li}_{\mathrm{sample}})/(^{7}\mathrm{Li}/^{6}\mathrm{Li}_{\mathrm{LSVEC}}) - 1$, and $\delta^{11}\mathrm{B} = (^{11}\mathrm{B}/^{10}\mathrm{B}_{\mathrm{sample}})/(^{11}\mathrm{B}/^{10}\mathrm{B}_{\mathrm{SRM951}}) - 1$. The results indicate that the H, Li, and B isotopic compositions of the micro-OM are almost the same as those of the surrounding matrix.

In addition to the micro-OM, round-shaped carbonaceous nodules ($20 \times 20\,\mu\mathrm{m}^2$-sized lithic fragments) with C and N isotopic compositions distinctly different from the surrounding matrix were found in C0053-1 (Fig. 7). There is no significant difference in the abundance of phyllosilicate and Fe-sulfide phases between the carbonaceous nodule and surrounding matrix. In the BSE image, the nodule is darker than the surrounding matrix (Fig. 7a), which is attributed to the enrichment of C in the carbonaceous nodule evidenced by the $^{12}\mathrm{C}^{12}\mathrm{C}^{-}$ ion map (Fig. 7e). The Raman spectrum shows that the carbonaceous nodule is enriched in OM (Fig. 7c) and depleted in carbonate (Fig. 7d) relative to the surrounding matrix. The lower Raman D/G value of the nodule compared to the surrounding matrix reveals that the OM that dominates in the nodule is more ordered and graphite-like than that in the matrix. Nitrogen is ubiquitous in both the matrix and nodule (Figs. 7e and 7f). The C and N are heterogeneously distributed in both domains, and their distributions appear correlated (Figs. 7e and 7f). The δ^{13}C and δ^{15}N values of the nodule ($\delta^{15}\mathrm{N} = 312 \pm 18$‰ and $\delta^{13}\mathrm{C} = 37 \pm 7$‰) are significantly higher than those of the matrix (Figs. 7f and 7g). The δ^{15}N value of the carbonaceous nodule is significantly enriched in ^{15}N and similar to the whole rock value of Bells (C2 ungrouped) and the most ^{15}N-enriched IOM.[33)]

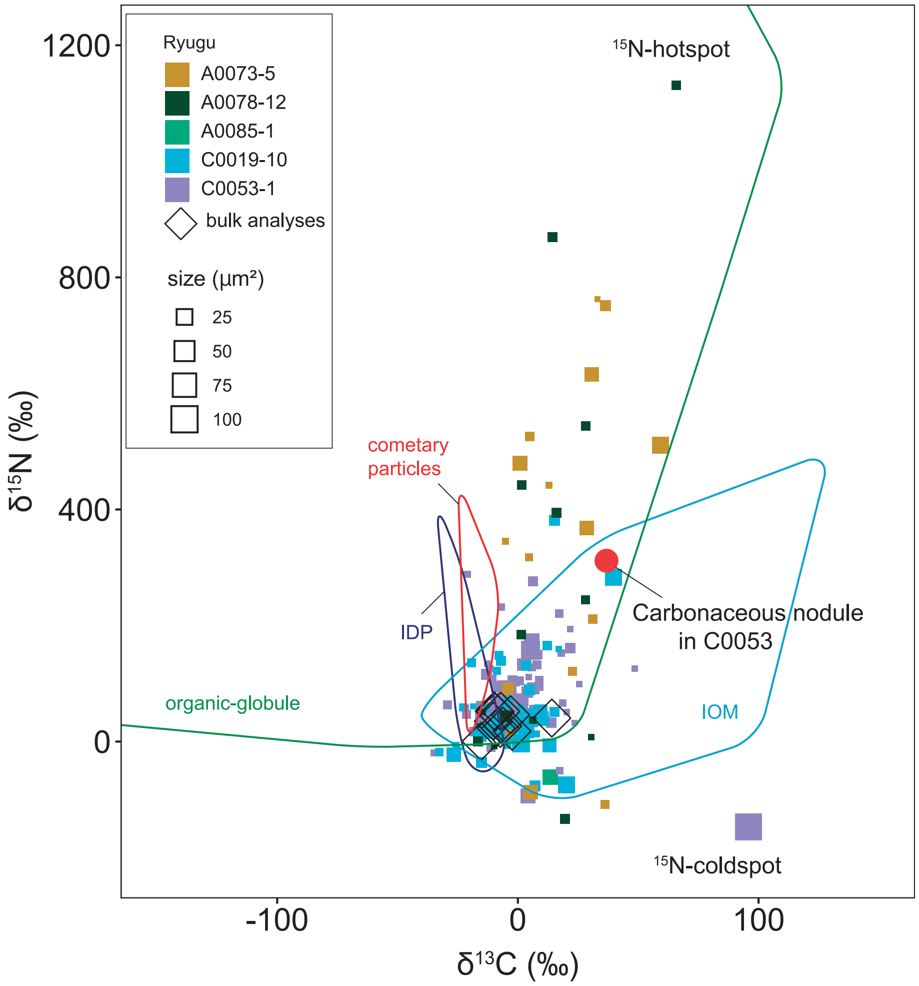

Fig. 12. C and N isotopic compositions (δ^{13}C *vs.* δ^{15}N) of micro-OM and a carbonaceous nodule. The size of the symbols is proportional to that of the object analyzed. The δ^{13}C and δ^{15}N values from bulk analyses (this study) and the ranges for IOM,[33] IDP,[106),202] cometary particles,[203] and organic-globules[107] are also shown.

Usually ^{15}N-enriched IOM is in negative correlation with δ^{13}C,[33] but this is not the case for the carbonaceous nodule and thus the high δ^{13}C value makes the nodule unique in terms of known solar system material.

4.1.4. Oxygen isotope thermometry. The coexistence of magnetite and dolomite is observed in the Ryugu particles (*e.g.*, Figs. 6d and 6f). Therefore, the crystallization temperatures of the magnetite-dolomite pairs were determined using O-isotope thermometry (*e.g.*, Fig. SA8b). The δ^{18}O values of magnetite and dolomite determined by SIMS are -2.0 ± 4.8‰ and 33.3 ± 3.9‰, respectively, for C0008-16 and 4.9 ± 2.9‰ and 38.4 ± 5.8‰, respectively, for A0022-15 (errors are 2SD) (Table S6). The average δ^{18}O values of dolomite and magnetite in A0022-15 are ∼5‰ higher than those in C0008-16, suggesting the O isotopic composition of the source reservoir (*i.e.*, co-existing fluid) differs between C0008-16 and A0022-15. The variability of δ^{18}O values within phases is significantly larger than analytical uncertainty, indicating that not all magnetite and dolomite grains formed in equilibrium. Thus, the magnetite and dolomite grains likely formed from reservoirs with temporally varying O isotopic compositions and temperatures. The change in the O isotopic composition and temperature may reflect a series of aqueous alteration events, with a specific series of dolomite and magnetite grains being formed in equilibrium with one another at a given time. Thus, the possible minimum and maximum temperatures that could be plausibly explained

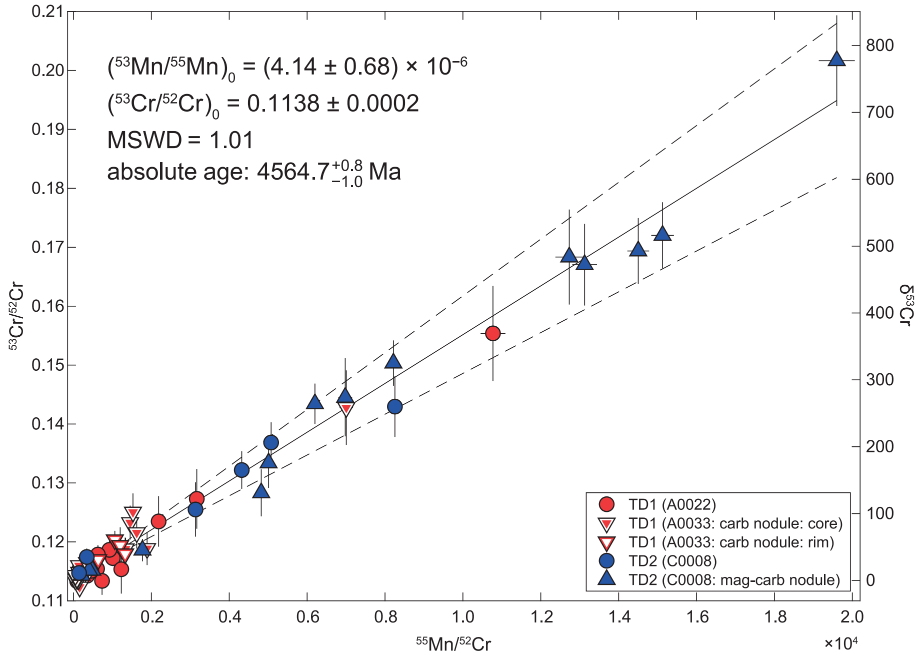

Fig. 13. Mn-Cr isochron diagram for dolomite grains. By assuming a homogeneous distribution of the (^{53}Mn/^{55}Mn)$_0$ in the early solar system, the ^{53}Mn-^{53}Cr age of dolomites, was calculated by the (^{53}Mn/^{55}Mn)$_0$ = 4.14 × 10^{-6} relative to the D'Orbigny angrite with (^{53}Mn/^{55}Mn)$_0$$^{\text{D'Orbigny}}$ = (3.24 ± 0.04) × 10^{-6} 36) and the decay constant of ^{53}Mn.37) The absolute age of dolomite grains was estimated to be 4564.7$^{+0.8}_{-1.0}$ Ma by referring to the Pb-Pb age of the D'Orbigny angrite with $t^{\text{D'Orbigny}}$ = 4563.37 ± 0.25 Ma.38),39)

by potential magnetite-dolomite pairs are calculated to yield a maximum range of temperatures that Ryugu could have experienced during aqueous alteration.

The $\Delta\delta^{18}$O ($\equiv \delta^{18}\text{O}_{\text{dolomite}} - \delta^{18}\text{O}_{\text{magnetite}}$) value was evaluated statistically using Bayesian estimation. The posteriori median $\Delta\delta^{18}$O values of C0008-16 and A0022-15 were estimated to be 35.4‰ and 33.5‰, respectively, and the corresponding Bayesian credible intervals (95%) for the median values are 32.9–37.8‰ and 31.4–35.5‰, respectively. Oxygen-isotope thermometry of magnetite and dolomite (Fig. 8) yielded estimated crystallization temperatures of 9^{+15}_{-13} °C (C0008-16) and 20^{+14}_{-12} °C (A0022-15) (Table S9).

4.1.5. ^{53}Mn-^{53}Cr dating of carbonates. The crystallization age of carbonates was determined using the ^{53}Mn-^{53}Cr chronometry. The ^{53}Cr/^{52}Cr and ^{55}Mn/^{52}Cr of dolomites in A0022-15, A0033-15, and C0008-16 are shown in Fig. 13 and Table S10. In Fig. 13, there is no significant difference in the slope (*i.e.*, age) of the regression line in the dolomites within and among TD1 and TD2 particles. No systematic differences were observed even within the 100-µm-sized coarse-grained and chemically-zoned carbonate nodule in A0033-15 (Figs. 3c and SA8a). Dolomite in the carbonate-magnetite nodule in C0008-16 (Fig. SA8b, from which O isotopic compositions were also determined) also plots on the same slope as the other dolomites, although it has a broad and systematically higher ^{55}Mn/^{52}Cr and ^{53}Cr/^{52}Cr. Since there are no significant differences in the formation ages of dolomites with different textures, all the measured data were used to calculate the formation age of the dolomite grains.

The initial ^{53}Mn/^{55}Mn [≡ (^{53}Mn/^{55}Mn)$_0$] was estimated as a slope of all datasets in the diagram, which was determined to be (4.14 ± 0.68) × 10^{-6} with MSWD (mean square weighted deviation) of 1.01 (Fig. 13) using a fitting algorithm.34) By assuming a homogeneous distribution of the (^{53}Mn/^{55}Mn)$_0$ in the early solar system, the ^{53}Mn-^{53}Cr age of dolomites, was calculated by the (^{53}Mn/^{55}Mn)$_0$ = 4.14 × 10^{-6} relative to the D'Orbigny angrite with (^{53}Mn/^{55}Mn)$_0$$^{\text{D'Orbigny}}$ = 3.24 × 10^{-6} 35),36) and the decay constant of ^{53}Mn.37) The absolute age of dolomites was estimated to be 4564.7$^{+0.8}_{-1.0}$ Ma (million years ago) by referring to the U-corrected Pb-Pb age of the D'Orbigny angrite with $t^{\text{D'Orbigny}}$ = 4563.37 ± 0.25 Ma.38),39)

The model age of dolomites was estimated to be 4564.7$^{+0.8}_{-1.0}$ Ma, which corresponds to 2.6$^{+1.0}_{-0.8}$ Myr after the formation of the solar system relative to the U-corrected Pb-Pb age of Ca-Al-rich inclusions (CAI) (4567.30 ± 0.16 Ma).40) The determined age overlaps with the oldest end of range reported for CI chondrites ($3.3^{+1.0}_{-0.9}$ to $5.0^{+0.9}_{-0.7}$ Myr after the formation of the solar system41),42)).

4.2. Bulk chemistry. The abundances (mass fractions, expressed as [Z] for element Z) of up to 70 elements were determined for aliquots of the 16 particles (Tables S1, S11, and S12). A aliquot of each particle was further divided into up to 8 aliquots and each aliquot was then used to determine the abundances of different groups of elements (see detail in Supplementary Text ST1.4 and Tables S11 and S12). The number of groups applied to each particle depends on the total mass of the particle available for the bulk analysis. A maximum 70 elements were measured from 6 particles (A0022, A0033, A0048, C0008, C0019, and C0079), with the total consumed weights for each aliquot being 1.7–3.3 mg. From the remaining ten particles, 42–59 elements were measured using 0.3–1.6 mg of the aliquots. Abundances of all determined elements relative to CI chondrites43) are shown in Fig. 14.

The isotopic compositions of eight elements (H, C, N, O, Ne, Ca, Cr, and Os) were determined. Hydrogen, C, and N isotopes were determined simultaneously with their abundance measurements (13 aliquots for H, using 0.057–0.317 mg and 14 aliquots for C and N using 0.103–0.765 mg). Neon isotopes were determined simultaneously with their abundance measurements from all 16 Ryugu particles using aliquots of 0.011–0.126 mg. Oxygen isotopes were determined from 5 particles using aliquots of 0.330–0.568 mg. Calcium and Cr were separated from 2 particles using aliquots of 0.444 and 0.457 mg, and their mass-independent isotopic compositions were determined. Osmium was separated from 6 particles using aliquots of 0.139–0.276 mg and their isotopic composition was determined. The total amount of sample consumed to obtain the above data was ~26 mg out of the 55 mg received.

4.2.1. Abundances of refractory to volatile lithophile and siderophile elements. Overall, the abundances of lithophile and siderophile elements in Ryugu particles are in close agreement with the weighted mean of CI chondrites,43) for three out of seven TD1 and all TD2 particles (Fig. 14). However, a detailed comparison of the differences between the Ryugu particles and the weighted mean of CI chondrites (Fig. 14c) shows that most of the refractory siderophile and refractory lithophile elements and B in Ryugu particles are higher than in the weighted mean of CI chondrites. The [Ta] in A0022, C0081, and C0019 are 4, 50, and 100 times higher than the others, respectively, while the other elements in these three particles do not show significant enrichments (Fig. 14). Such a finding suggests that these particles were contaminated by the Ta bullet that was used to impact the Ryugu surface during sample collection. Thus, the [Ta] of these three particles were excluded from the weighted mean values shown in Fig. 14c. However, no Cu contamination was observed, which was expected due to its inclusion in the projectile of SCI.

The TD1 particles show greater variations in their [REE], [Y], [P], [U], [Ca], [Sr], [Th], [Tl], and [B] compared with those of the TD2 particles (Figs. 14a and 14b). The abundances of these elements, except Tl and B, in the TD1 particles are correlated with each other. The correlation coefficients (R) with [P] are 0.97–0.96 for [HREE] and [Y], 0.94–0.91 for [MREE], 093–0.88 for [LREE], 0.88 for [Sr], 0.84 for [Ca], 0.79 for [Th], 0.77 for [U]. These correlations can be explained if there are variable abundances of apatite in the TD1 particles, because REE, Y, Sr, U, and Th are enriched in apatite (Fig. SA5).27)

While the elemental abundances of the TD2 particles are less heterogeneous relative to those of the TD1 particles, considerable variations were observed in the [B], [Be], [Bi], [Pd], [Re], and [Ir] (Figs. 14a and 14b) for the TD2 particles. The Be and Bi in TD2 particles are present in CI to sub-CI abundances, while B is present in CI to super-CI abundances. Furthermore, the [Be] and [B] demonstrate a negative correlation with one another ($R = -0.94$; Fig. 15a). Such a feature is not observed in the TD1 particles. Among elements with similar volatility to Be and B, no anomaly relative to the CI abundance is observed. Thus, the correlation is not caused by volatility-dependent processes, such as condensation processes in the inner protosolar nebula (PSN). Alternatively, B is a fluid-mobile element, which can easily fractionate during solid-fluid reaction processes, such as aqueous alteration. However, there is no evidence to suggest the elemental fractionation of other highly mobile elements (*e.g.*, Li, Na, K, Rb and Cs) among the TD2 particles, through an open-system fluid-solid interaction process. Thus, the correlation is not caused by a solubility-dependent process.

The [Bi] in TD2 particles shows a high correlation with [Mo] ($R = 0.96$, Fig. 15b). From a gas of solar composition, Bi and Mo are condensed as pure

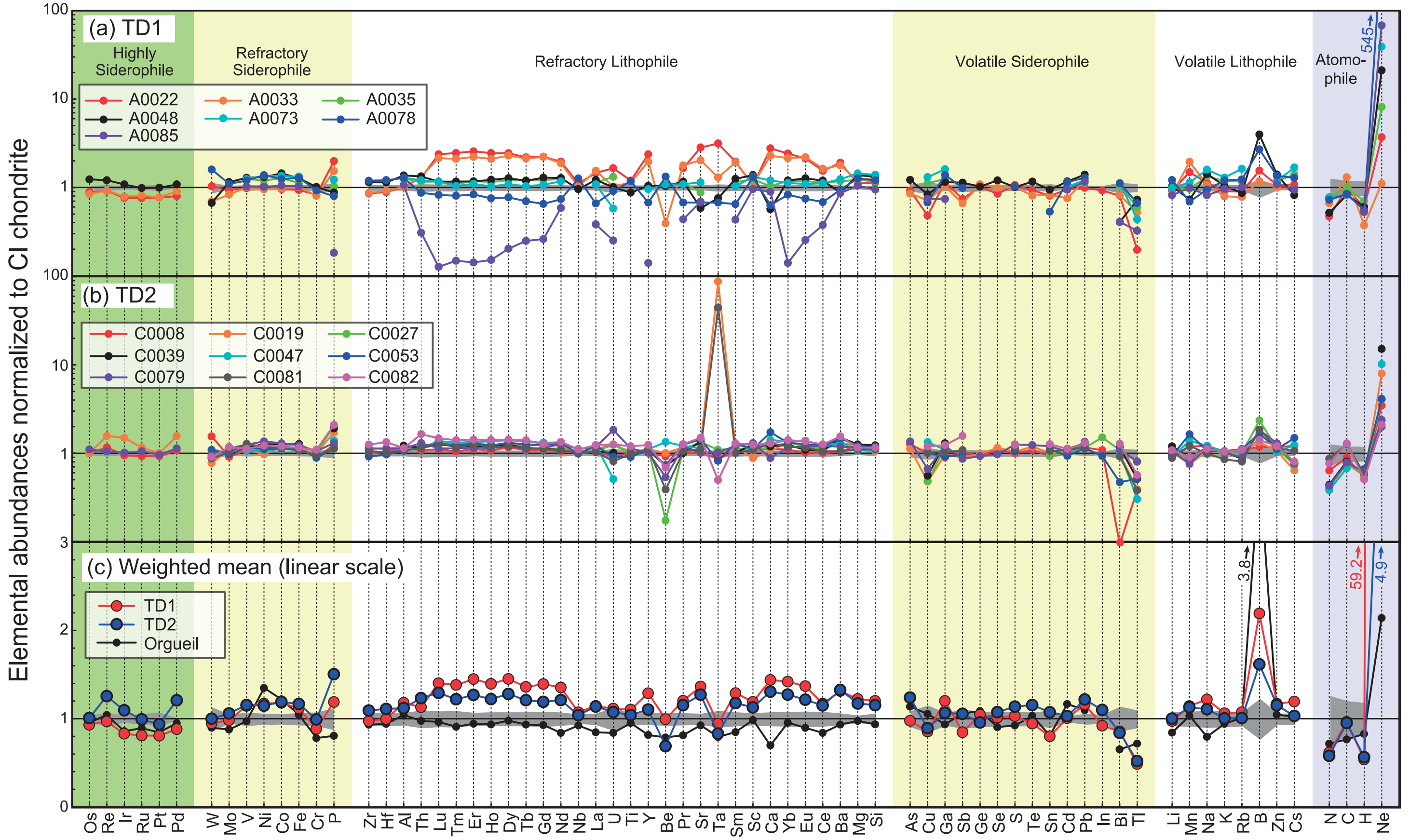

Fig. 14. (a) Elemental abundances of TD1 particles, (b) elemental abundances of TD2 particles, and (c) the weighted mean of the elemental abundances of TD1 and TD2 particles (Table S14). In (c), the elemental abundances of Orgueil (CI1) analyzed by this study are shown for comparison. The elemental abundances of all particles are normalized to the weighted mean value of CI chondrites.[43] The 2 sigma range of CI chondrites[43] is shown in gray. Note that the scales in (a) and (b) are logarithmic, and that in (c) is linear. The elements are ordered in terms of their volatility, which is defined by the 50% condensation temperature of each element in each element group.[44] The particles A0022, C0019 and C0039 were contaminated by the Ta bullet, and the [Ta] of these particles were not included for the calculation of the weighted mean for the TD1 and TD2 particles.

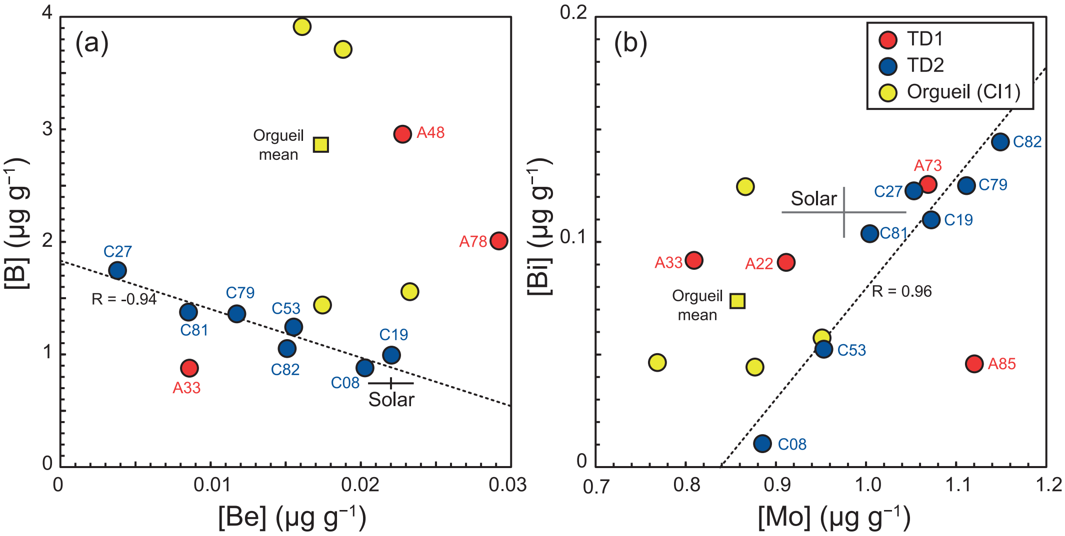

Fig. 15. (a) [Be] *vs.* [B] and (b) [Mo] *vs.* [Bi]. The broken lines represent the regression line for TD2 particles in (a) and (b). The yellow square represents the mean values of Orgueil (CI1) determined in this study. Cross is the Si-normalized solar abundance with a 1SD range are from Lodders.[43] Note that the particle names have the first two zeros removed.

metals,[44] and therefore, should be independent of one another. Thus, the positive correlation between [Bi] and [Mo] may be due to the heterogeneous distribution of Bi-Mo compounds (*e.g.*, bismuth molybdate, $Bi_2[MoO_4]_3$) which may have formed on the asteroid.

4.2.2. Abundances of highly siderophile elements and Os isotopes. Since nugget heterogeneity is significant for the highly siderophile elements (HSE: Ru, Pd, Re, Os, Ir, and Pt) in chondrites,[45] HSE were measured for more than two aliquots from each particle, except for C0079. Some of the Os-extracted residues, after the inverse aqua regia digestion, were further desilicified with HF.[46] The result shows that there were no significant differences in HSE abundances among the multiple aliquots, except for C0019 (Fig. SA9 and Table S13).

The $^{187}Os/^{188}Os$ among bulk Ryugu particles is quite uniform (0.124–0.127 with an uncertainty of 0.006–0.012; Fig. SA10), and comparable to the mean $^{187}Os/^{188}Os$ of CI chondrites (0.1262 ± 0.0002[47])). Except for one aliquot (C0019-16), the $^{187}Re/^{188}Os$ values (0.36–0.49 with an uncertainty of 0.06–0.11) are also indistinguishable from the mean $^{187}Re/^{188}Os$ of CI chondrites (0.392).[47] The $^{187}Re/^{188}Os$ and $^{187}Os/^{188}Os$ of most CI chondrites plot on the 4.558-Ga isochron of the IIIA iron meteorites,[48] suggesting that Re/Os was not disturbed since their formation.

C0019-16 has an exceptionally high $^{187}Re/^{188}Os$ (0.60 ± 0.09), and plots away from the 4.558-Ga isochron. The [Os] in C0019-16 (477 ng g^{-1}) falls within the range of all Ryugu bulk particles (400–583 ng g^{-1}) and is comparable to the mean [Os] of CI chondrites (460 ± 4 ng g^{-1}).[47] Whereas, the [Re] in C0019-16 (59 ng g^{-1}) is significantly higher than that of the other Ryugu particles (29–48 ng g^{-1}) and the mean [Re] of CI chondrites (38.1 ± 1.9 ng g^{-1}).[47] It is, therefore, considered that the elevated $^{187}Re/^{188}Os$ in C0019-16 is due to Re addition rather than Os loss in this aliquot. The $^{187}Os/^{188}Os$ ratio of C0019-16 (0.126 ± 0.007) is comparable to the other Ryugu particles and suggests that the Re addition should have occurred recently.

The major reservoir of HSE among the identified minerals in the Ryugu particles appear to be Fe-sulfides. However, the bulk HSE abundance does not depend on the modal abundance of coarse-grained (>1 µm) Fe-sulfides. For example, A0022 and A0033, which have lower HSE values (Fig. 14), contain a greater abundance of Fe-sulfide than the others, except for C0019. In the matrix of Ryugu particles, sub-µm-sized Fe-sulfides are also widespread, but their modal abundances have not been estimated due to their small grain size. Furthermore, there could be HSE-enriched metal and/or oxide minerals, which are fine-grained (<1 µm) and have not been identified.

To clarify this discrepancy, HSE abundance ratios were measured for the coarse-grained euhedral Fe-sulfide grains, separated from C0019 (Fig. SA9). The Pd/Ru, Ir/Ru, Os/Ru, and Pt/Ru in the Fe-sulfide separate are 0.1, 0.4, 0.4, and 1.5 times, respectively, relative to the mean value of the Ryugu bulk particles (Re/Ru could not be determined because of the low [Re]) (Table S13). This result suggests that the HSE abundance of the bulk particles depends not on those of the coarse-grained Fe-sulfide minerals, but on the sub-µm sized Fe-sulfide grains or the unidentified HSE-rich phases in the matrix. Such phases would be high in Pd/Ru, Ir/Ru, Os/Ru, and probably Re/Ru. Among the two bulk aliquots from C0019, C0019-16 shows extremely high [Ir] and [Pd], and a high ^{187}Re/^{188}Os, compared to bulk Ryugu particles. The result could be attributed to the heterogenous distribution of the fine-grained HSE-rich phases in the matrix, which would have resulted from a recent as yet unknown process.

4.2.3. Hydrogen, C, and N isotopes. The elemental abundances and isotopic compositions for Ryugu particles were determined by IRMS, including H ([H] and δD for 13 particles), total carbon (TC; $[C]_{TC}$ and $\delta^{13}C_{TC}$ for 14 particles) and N ([N] and δ^{15}N for 14 particles using the same aliquot for the TC measurement). In addition, the [C] and δ^{13}C of the total organic carbon (TOC; $[C]_{TOC}$ and $\delta^{13}C_{TOC}$) was determined for 13 Ryugu particles with aliquot weights of 0.027–0.122 mg. Ryugu particles exhibit variations of $[H] = 0.69$ to 1.30 wt%, $[C]_{TC} = 2.79$ to 5.39 wt%, $[C]_{TOC} = 1.77$ to 4.00 wt%, $[N] = 0.10$ to 0.22 wt%, $\delta D = 100$ to 345‰, $\delta^{13}C_{TC} = -15.3$ to 14.1‰, $\delta^{13}C_{TOC} = -23.1$ to -15.4‰, and $\delta^{15}N = 0.4$ to 53.0‰ (Fig. 16 and Table S14). There were no systematic differences of such values between the TD1 and TD2 particles.

The [H] of Ryugu (weighted average: 1.03 wt%) is lower than that of Orgueil (CI1) measured in this study (average: 1.54 wt%) and the CI chondrites analyzed by Alexander *et al.*[49] (average: 1.55 wt%). Whereas the [H] of Ryugu (except for A0033) is comparable to or higher than the CI chondrites measured by Vacher *et al.*[50] (average: 0.95 wt%) and Kerridge[51] (average: 0.63 wt%). The δD values of most Ryugu particles are higher than those of CI chondrites and lower than those of the Tagish Lake (C2 ungrouped). The discrepancy of [H] between Orgueil analyzed by this and among all the CI chondrites analyzed by other studies is probably due to different sample treatments prior to the analyses. The H_2O in a sample includes that which is adsorbed from the terrestrial atmosphere and that which resided intrinsically in the interlayer of phyllosilicates and Fe-(oxy)hydroxides. In previous studies, the carbonaceous chondrite samples were pre-treated by either storage within a desiccator for days to weeks at room temperature,[49] heating at 120 °C for 48 hours *in vacuo*,[50] or heating at 200 °C overnight in air,[51] to remove atmospheric H_2O contamination. Separation of atmospheric water is difficult as degassing of part of the intrinsic water occurs at a similar temperature (100–200 °C or lower).[52] Subtle differences in the preheating temperature or duration may result in loss of indigenous water to various extents, hence a large discrepancy among labs usually occurs. The Ryugu particles are little affected by atmospheric contamination. They were captured at the asteroidal surface while in the vacuum of space, and handled in a terrestrial laboratory with minimal exposure to the atmosphere. The Ryugu particles could have been heated up to ~100 °C[53] before sampling on the asteroidal surface. Hence, we employed preheating at 110 °C *in vacuo* for 6 hours, followed by cooling at room temperature for a further 6 hours, as not to overheat the aliquots relative to asteroidal conditions.

The main reservoir of H in the Ryugu particles is phyllosilicates, with minor amount being present within OM. Assuming that all H exists in phyllosilicates and OM and the [H]/[C] of OM is 0.061,[49] a mass balance calculation, using the $[C]_{TOC}$ and bulk [H] value, the modal abundance of the mineral components, and bulk density of Ryugu particles, yielded the [H] in Ryugu phyllosilicates to be 1.2 ± 0.7 wt% (2SD). In this calculation, the porosity in the matrix was calculated to fit the bulk density of Ryugu particles. The stoichiometric [H] of lizardite (serpentine group mineral) and saponite (smectite group mineral) are 1.45 and 2.10 wt%, respectively. Although the mean values of the calculated [H] in the phyllosilicate is lower than the stoichiometric [H], they agree within the 2SD range. Thus, the determined bulk [H] of the Ryugu particles is consistent with the petrography.

Variations in the $[C]_{TC}$ and $\delta^{13}C_{TC}$ of Ryugu particles largely overlap with those of CI chondrites (Fig. 16c). The one exception is A0022, which shows a significantly higher $\delta^{13}C_{TC}$ similar to Tagish Lake. The restricted $\delta^{13}C_{TOC}$ values relative to the $\delta^{13}C_{TC}$ values for all particles suggest that the variation of $\delta^{13}C_{TC}$ among the particles is primarily controlled by carbonates. Through mass balance calculations, using the data of five Ryugu particles (A0022, A0033, A0078, C0081, and C0082), $[C]_{carb}$ (the [C] of carbonate) and $\delta^{13}C_{carb}$ (the δ^{13}C of carbonate) are estimated to be 1.2 ± 0.5 to 3.0 ± 0.5 wt%

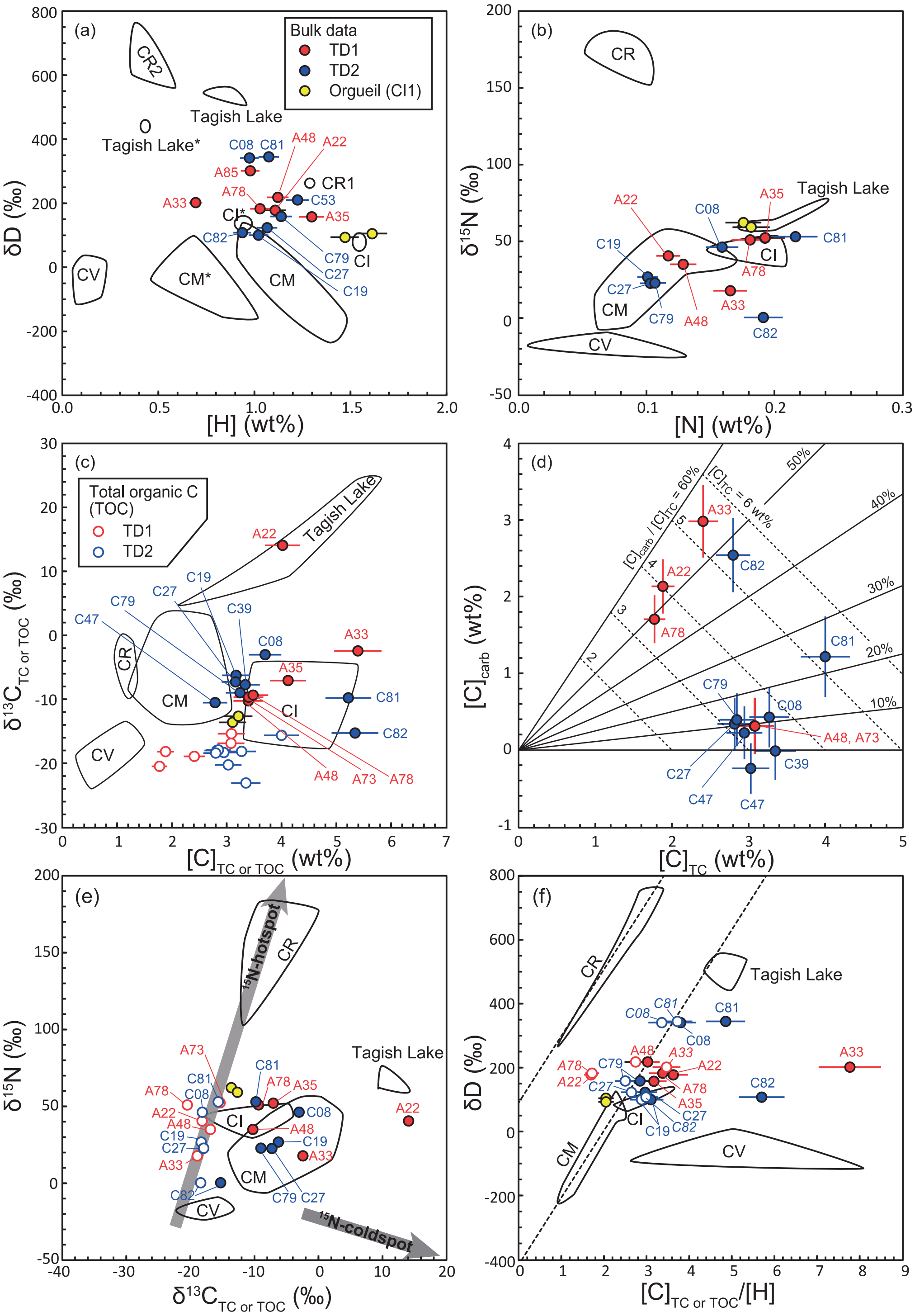

Fig. 16. (a) [H] *vs.* δD, (b) [N] *vs.* δ^{15}N, (c) [C] *vs.* δ^{13}C, and (d) $[C]_{TOC}$ *vs.* $[C]_{carb}$ (TOC and carb denote total organic C and carbonate C), (e) δ^{13}C *vs.* δ^{15}N and (f) [C]/[H] *vs.* δD. Error bars are 2SD. In (c), (e), and (f), values of both total C (TC) and TOC are presented. Data for carbonaceous chondrites are from refs. 49, 50, 204–206. The regions of CI, CM, and Tagish Lake (C2 ungrouped) indicated with * are from ref. 50 (see the main text for more details). Solid and dashed lines in (d) are the mass fraction of calculated carbonate C in TOC and that of TC, respectively. The gray thick arrows in (e) indicate trajectories toward the ^{15}N-hotspots and ^{15}N-coldspots shown in Fig. 12. The dashed lines in (f) represent the fitting lines for CR and CM chondrites.[49] Note that the particle names have the first two zeros removed.

(Fig. 16d), and -12 ± 4‰ to 43 ± 8‰, respectively (Table S14). The same approach could not be applied to the other particles, since the carbonates were too small to quantitatively estimate their modal abundance.

The [N] and δ^{15}N of the Ryugu particles mostly fall within the ranges of CI and CM chondrites that form a broad linear array in Fig. 16b. However, two particles (A0033 and C0082) show a deviation from the array to lower δ^{15}N values.

The $\delta^{13}C_{TC}$ and δ^{15}N values of Ryugu particles (except for A0022) show variability that is within or near the range of CM and CI chondrites (Fig. 16e). On the other hand, $\delta^{13}C_{TOC}$ and δ^{15}N values demonstrated a relatively restricted range of compositions and their trend extends toward the composition of the ^{15}N-hotspots. This result, combined with the data for the pixel-by-pixel and area analyses by SIMS, indicates that the bulk $\delta^{13}C_{TC}$ and δ^{15}N values of Ryugu particles can be explained by mixing between the ^{13}C- and ^{15}N-poor OM components, which are dominant in the phyllosilicate-rich matrix, and the ^{15}N-rich OM. The bulk isotopic composition of two particles (A0033 and C0082), which deviate from the others in Fig. 16b, could be influenced by the presence of ^{15}N-coldspots in these particles. The elevated and variable $\delta^{13}C_{TC}$ values relative to $\delta^{13}C_{TOC}$ are due to the presence of carbonates (Fig. 16e).

Linear correlations of $[C]_{TC}/[H]$ *vs.* δD are found for CR and CM chondrites,[49] which were interpreted as the result of mixing between hydrogen from water/OH in phyllosilicates with different δD values and hydrogen from OM. In the case of Ryugu particles, a higher abundance of carbonate results in a higher $[C]_{TC}/[H]$ value for a given particle. Therefore, it is appropriate to use the $[C]_{TOC}/[H]$ to evaluate the mixing relationship of H (Fig. 16f). Although $[C]_{TOC}/[H]$ and δD of Ryugu particles plot on and around the linear array extending from the range of CM chondrites to higher δD values (CM line), they do not form a linear trend in Fig. 16f. Furthermore, the wide range of δD values of OM (150–3000‰, Figs. 10 and 11) makes it difficult to represent the bulk δD values as a mixture of two unique endmember components. Assuming a $H/C = 0.061$[49] and δD value of 150–3000‰ for Ryugu OM, δD values for Ryugu phyllosilicate minerals can range between -600 and 400‰, which includes the δD ranges of the Earth, Oort Cloud Comets, and Jupiter Family Comets.[54]

4.2.4. Bulk O, Ca, and Cr isotopes. Bulk O isotopic compositions were determined by IRMS for five particles: two from the TD1 site (A0022 and A0033) and three from the TD2 site (C0008, C0019, and C0079), yielding $\delta^{18}O = 17.72$–20.08‰, $\delta^{17}O =$ 9.84–11.03‰, and $\Delta^{17}O = 0.503$–0.614‰ (Figs. 8 and 17a and Table S14). The range of Δ^{17}O values covering all the particles measured is 0.111‰, which is nearly equivalent to the 2SD external precision (±0.054). Thus, the Δ^{17}O value of the Ryugu particles was found to be nearly homogeneous on the scale of >0.3 mg. Whereas, the range of δ^{18}O values (2.36‰) is an order of magnitude larger than the 2SD external precision (±0.16‰).

The mass-independent isotopic compositions of $^{54}Cr/^{52}Cr$ and $^{48}Ca/^{44}Ca$ were measured for two particles: A0022 and C0081 with aliquot weights of 0.444 and 0.457 mg, respectively. The ε^{54}Cr and ε^{48}Ca values of A0022 were 1.49 ± 0.16 and 1.97 ± 0.33, respectively, and of C0081 were 1.77 ± 0.10 and 2.21 ± 0.27, respectively (Figs. 17b and 17c), where $\varepsilon^{54}Cr = [(^{54}Cr/^{52}Cr_{sample})/(^{54}Cr/^{52}Cr_{SRM979}) - 1] \times 10^4$ and $\varepsilon^{48}Ca = [(^{48}Ca/^{44}Ca_{sample})/(^{48}Ca/^{44}Ca_{SRM915a}) - 1] \times 10^4$.

The O, Cr, and Ca isotopic compositions of Ryugu particles most closely resemble the CI chondrites out of all known meteorite groups, but show distinctively higher δ^{18}O and Δ^{17}O values than those of CI chondrites ($\delta^{18}O = 14.26$–16.70‰ and $\Delta^{17}O = 0.201$–0.453‰, Fig. 8). The ε^{54}Cr value of the A0022 is within the range of that of CI chondrites ($\varepsilon^{54}Cr = 1.44$–1.65),[55)–58)] but that of C0081 is slightly higher than the CI chondrites (Fig. 17). The ε^{48}Ca value of the Ryugu particle is within the range of CI, (2.06 ± 0.09 to 2.30 ± 0.80),[59)–61)] CR (2.07 ± 0.05 and 2.23 ± 0.04),[61] and CM (2.1 ± 0.9 and 3.14 ± 0.14)[59),61)] chondrites.

4.2.5. Neon. Neon elemental abundances and isotopic compositions are shown in Fig. 18 and Table S15. The [Ne] in TD1 and TD2 particles range from 2.0×10^{-7} to 1.1×10^{-4} and from 4.0×10^{-7} to 3.5×10^{-6} ccSTP g^{-1}, respectively. The variation of the [Ne] of TD1 particles is larger than that of TD2 particles (Figs. 14, 18a, and 18b). A0033 has the lowest [Ne], and A0078 and A0085 have the two highest [Ne]. The [Ne] and [REE] of TD1 particles are anti-correlated (Figs. 14 and 19). The two particles with the lowest-[Ne] (A0022 and A0033) have the two highest [REE], and the two particles with the highest-[Ne] (A0078 and A0085) have the two lowest [REE]. Furthermore, the weight of the aliquot used for the determination of [Ne] and [REE] shows no correlation with the magnitude of the abundance measured and thus the above negative correlations

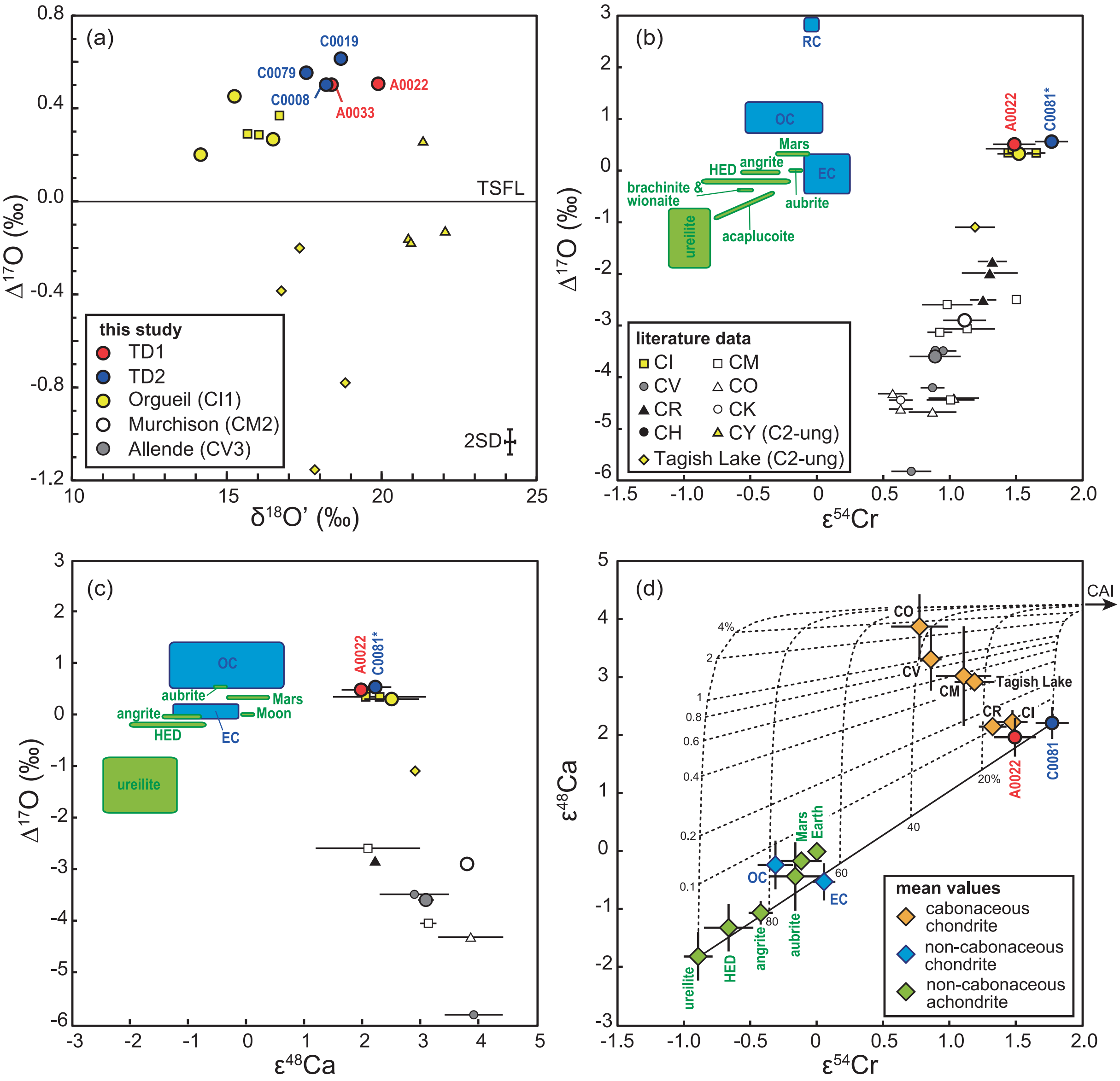

Fig. 17. (a) δ^{18}O' *vs.* Δ^{17}O, corresponding to the dashed rectangle in Fig. 8, (b) ε^{54}Cr *vs.* Δ^{17}O, (c) ε^{48}Ca *vs.* Δ^{17}O, and (d) ε^{54}Cr *vs.* ε^{48}Ca, with the values of terrestrial and extraterrestrial materials also included.55)–61),79),190),191),193),194),207)–230) *: Since the oxygen isotopic composition of C0081 was not determined, the average Δ^{17}O of Ryugu was used for C0081. The error bars for data in this study and compiled data for carbonaceous chondrites from the literature are 2SE. The ranges of data for non-carbonaceous chondrites (OC, EC and RC) and achondrites are shown as blue and green areas in (b) and (c), where OC, EC, and RC denote ordinary, enstatite, and R chondrites, respectively. For other classes, error bars are either 2SE of an analysis (when only one analysis is available for a class), a range of two analyses (when only two analyses are available), or 1SD of the analyses (when more than three analyses are available). The solid line in (d) represents a mixing line between a highly thermally-processed disk reservoir (ureilite) and a disk reservoir that has experienced low thermal processing (C0081). Dashed lines in (d) represent mixing curves between CAI and the disk reservoirs, and the numbers represent the proportion of mixed CAI in percent. The Ca/Cr, ε^{54}Cr, and ε^{48}Ca values of CAI are 291, 6.2, and 4.3,231)–235) respectively. The ε^{54}Cr, and ε^{48}Ca values of ureilite are −0.9 and −1.8, respectively. The Ca/Cr value of the ureilite-Ryugu mixture is fixed as 1.1 (the solar value) because the Ca/Cr of ureilite does not represent that of the parent body.236)

are not related to a sampling bias. Therefore, the negative correlations are not related to heterogeneity within a particle.

The TD1 and TD2 particles show a correlation among their [Ne], ^{20}Ne/^{22}Ne, and ^{21}N/^{22}Ne (Fig. 18). The ^{20}Ne/^{22}Ne and ^{21}Ne/^{22}Ne of particles enriched in

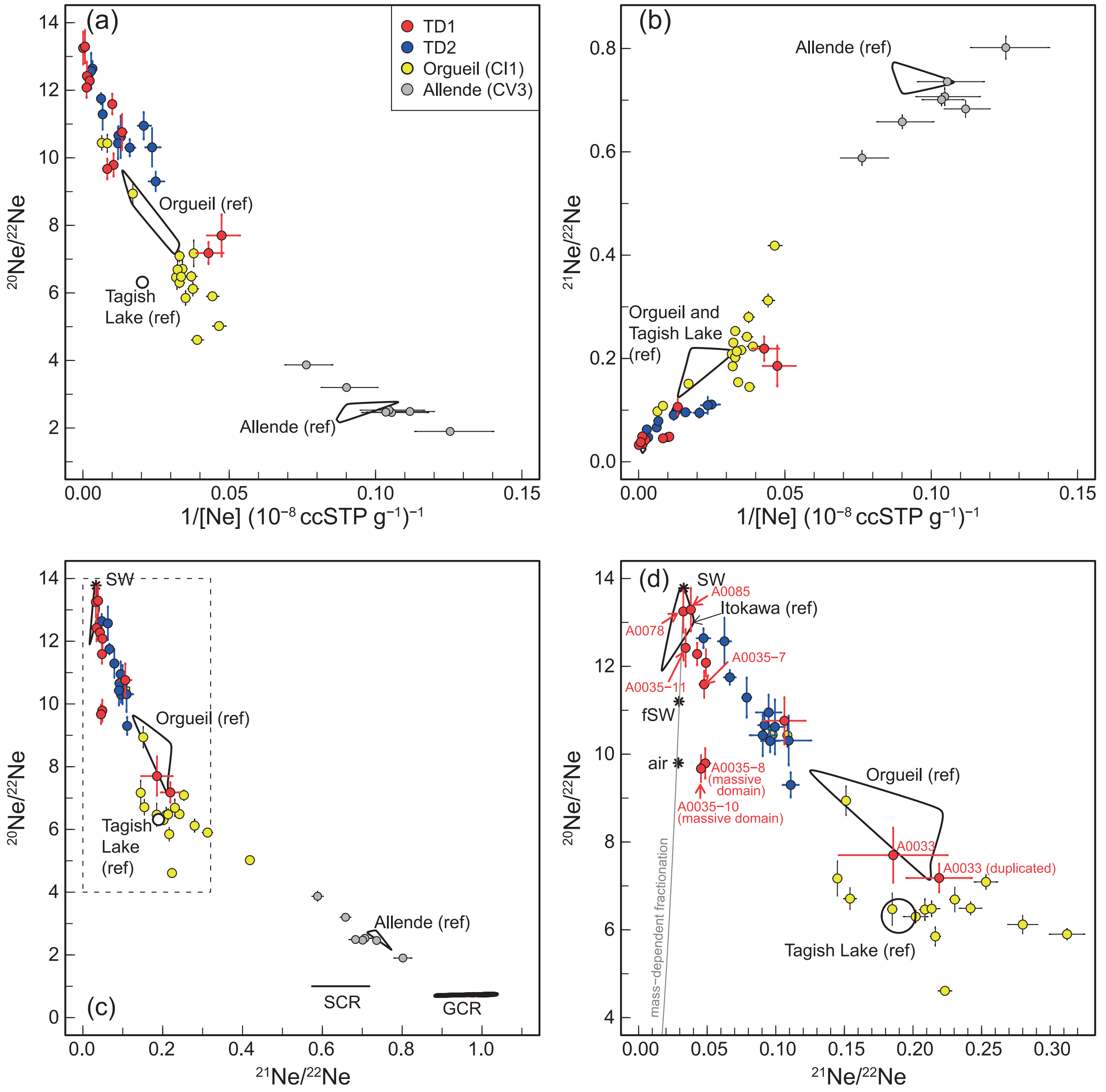

Fig. 18. (a) 1/[Ne] *vs.* ^{20}Ne/^{22}Ne, (b) 1/[Ne] *vs.* ^{21}Ne/^{22}Ne, and (c) ^{21}Ne/^{22}Ne *vs.* ^{20}Ne/^{22}Ne. (d) An enlarged view of the dashed rectangle in (c). The data for Orgueil (CI1) and Allende (CV3) obtained in this study are also shown. The bars labelled GCR and SCR in (c) denote the ranges of ^{20}Ne/^{22}Ne and ^{21}Ne/^{22}Ne of cosmogenic Ne, which would have been produced through irradiation by galactic and solar cosmic rays of Ryugu particles and are calculated using the models of refs. 237 and 238, respectively. For comparison, data obtained by previous studies include Itokawa “ref” [62], Allende (CV3) “ref” [239)–242], Orgueil (CI1) “ref” [64)–66], Tagish Lake (C2 ungrouped) “ref” [243], solar wind (SW),[63] and fractionated SW (f$_{\mathrm{SW}}$, formerly referred as solar energetic particle),[244] and air.[245]

Ne are characterized by the highest and the lowest values, respectively (Figs. 18a and 18b). ^{20}Ne/^{22}Ne and ^{21}Ne/^{22}Ne of the two highest [Ne] particles (A0078 and A0085) are 13.25 (± 0.49) to 13.29 (± 0.50) and 0.0326 (± 0.0011) to 0.0381 (± 0.0005), which are comparable to those of Itokawa (^{20}Ne/^{22}Ne = 13.1–13.6 and ^{21}Ne/^{22}Ne = 0.031–0.033),[62] and to the solar wind[63] (Fig. 18d). ^{20}Ne/^{22}Ne and ^{21}Ne/^{22}Ne of the lowest [Ne] particle (A0033) is comparable to those of Orgueil (CI1).[64)–66]

The heterogeneity of the Ne abundance and isotopic composition within a particle is addressed here. A0035 is a 1-mm-sized particle that contains both typical matrix material and atypical matrix

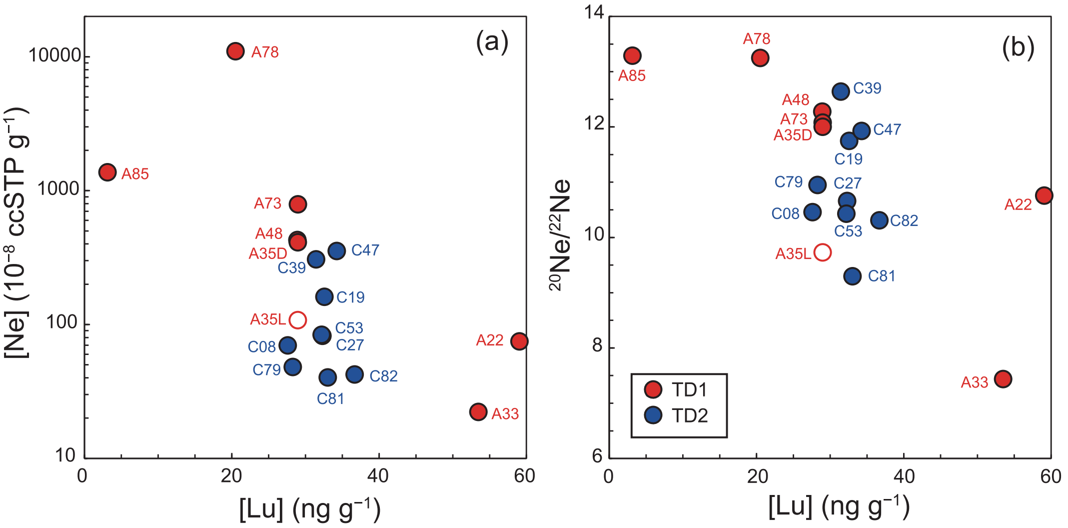

Fig. 19. (a) [Lu] *vs.* [Ne] and (b) [Lu] *vs.* $^{20}Ne/^{22}Ne$. Note that the particle names have the first two zeros removed. A35D (solid circle) and A35L (open circle) indicate the matrix and the massive domain of A0035, respectively. Note that the [Lu] data in A35D and A35L are the same, because [Lu] was obtained from a bulk measurement of A0035.

material, which was termed previously the massive domain (see section 4.1.1) (Figs. 1e and 1f). Using tweezers, aliquots (100–200 µm) of the matrix (A0035-7 and A0035-11) and the massive domain (A0035-8 and A0035-10) were picked up. The aliquots from the matrix and the massive domain yield distinct isotopic compositions Fig. 18. The $^{20}Ne/^{22}Ne$ values of the massive domain (9.7 and 9.8) are significantly lower than those of the matrix (11.6 and 12.4). One of the matrix aliquots (A0035-11) has [Ne] 6–8 times higher than the other three aliquots.

4.3. Characteristics of OM. In order to investigate the OM components within Ryugu particles, DESI-OT-MS (an ambient mass spectrometry imaging technique), UHPLC-OT-MS (a compound specific mass spectrometry technique) and Raman and FTIR spectroscopy were applied. The IOM separated from aliquots of A0035-3 (0.983 mg) and C0008-18 (1.90 mg) were analyzed by FTIR spectroscopy, with the hot water extract from the pre-demineralized C0008-18 being used for UHPLC-OT-MS analysis. Meanwhile, DESI-OT-MS was carried out on 0.5–1 mm-sized aliquots of A0048-10 and C0008-15. Raman spectroscopy was carried out on an aliquot of every particle.

4.3.1. Insoluble organic matter (IOM). The G- and D-band peaks, indicating the sp^2 and sp^3 bonds, respectively, of organic materials obtained by Raman spectroscopy[67] were ubiquitously detected in the phyllosilicate-dominated matrix and the carbonaceous nodules of Ryugu particles (Table S16 and Fig. SA11). According to SEM petrography, micro-OM are heterogeneously distributed in the matrix (Figs. 7, 10a, and 11), but they are not clearly visible as distinct features in Raman spectroscopic maps (Fig. SA11). This result suggests that nano-OM (Fig. 4a) and sub-nanometer-sized IOM are present throughout the phyllosilicate matrix. Nevertheless, there is likely to be heterogeneity of OM at spatial scales below the observed spot diameter (∼0.7 µm).

The extracted G and D-band features from the 2D-Raman mapping results are statistically summarized and shown in Table S16. In Fig. 20a, the peak positions of the G-band and the corresponding full width at half maximum (FWHM) values are within the ranges previously reported from meteorites and interplanetary dust particles (IDPs),[68)–70)] and these values show a negative correlation among the particles, albeit with an overlap of the TD1 and TD2 clusters near the center of the figure. Meanwhile, the peak position of the G-band shows a weak positive correlation with the D/G value ($R^2 = 0.42$, $R = 0.65$) (Fig. 20b). Furthermore, the groups of particles from TD1 and TD2 seem to form loose clusters, respectively, and compared to the particles from the TD2, those from TD1 are characterized by lower G-band peak positions, higher FWHM values, and lower D/G values. The TD2 particles are likely to contain ejecta associated with SCI crater formation (depth estimated to be 1.7 m from the original

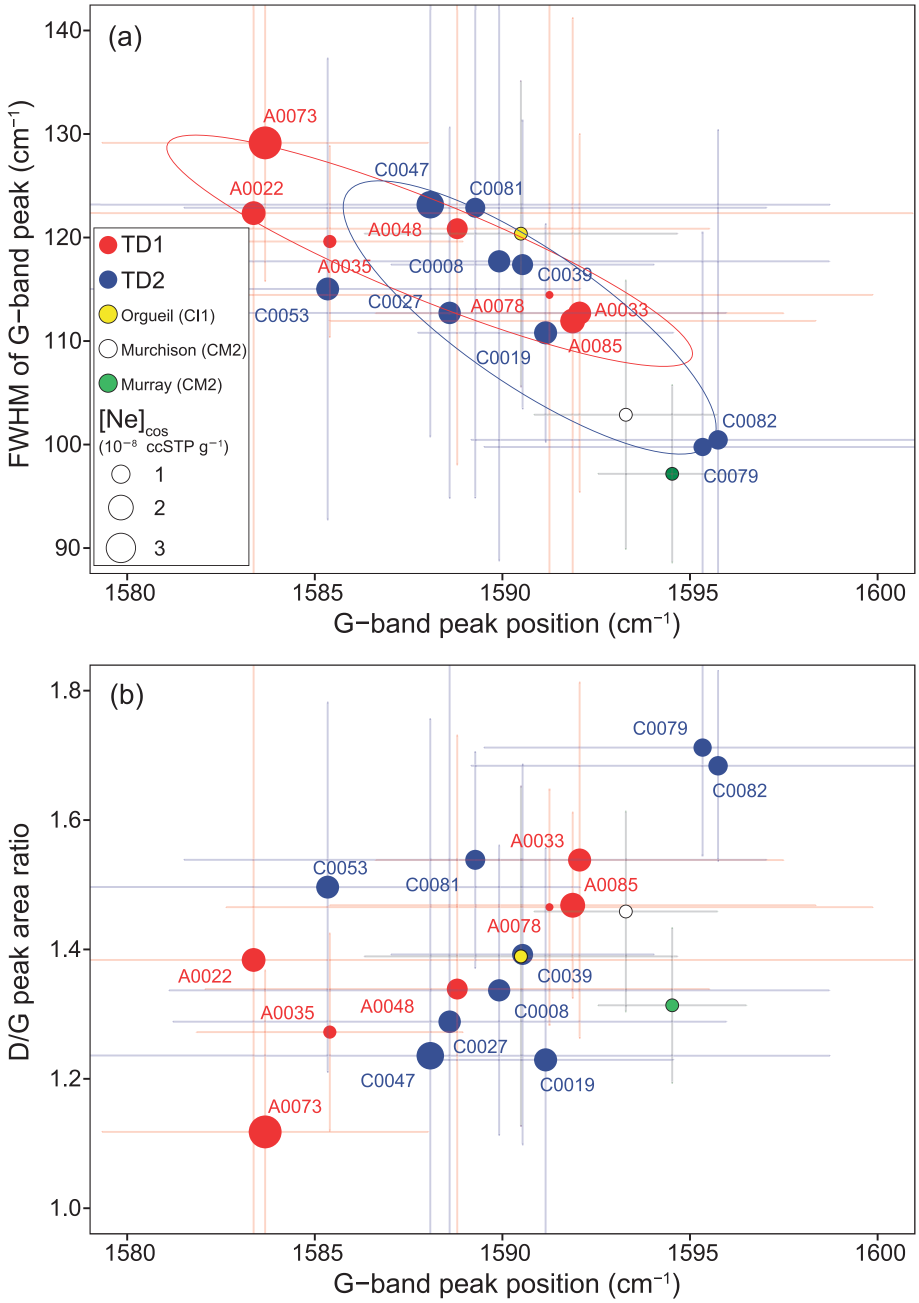

Fig. 20. Plots of the Raman peak parameters from Raman spectroscopy of Ryugu particles and Orgueil (CI1), Murchison (CM2), and Murray (CM2). (a) Peak position (cm^{-1}) *vs.* FWHM (full width at half maximum) of the G-band peak, and (b) Raman shift peak position (cm^{-1}) of the G-band *vs.* the D/G peak area ratio. The error bars are 1SE. In both diagrams, maker sizes for TD1 and TD2 are proportional to the mean [Ne] from cosmogenic (cos) component (in 10^{-8} ccSTP g^{-1}) in each particle.

surface).[16] In contrast, the TD1 particles should represent recovered material that existed closer to the surface.

The FTIR vibrational assignments for the demineralized OM of Ryugu particles A0035-3 and C0008-18 and Orgueil (CI1) were made with reference to the literature.[71)–73)] The Ryugu particles and Orgueil displayed virtually the same vibrational modes, except with the symmetrical C-H_2 and C-H_3 stretching vibration being combined for A0035 in

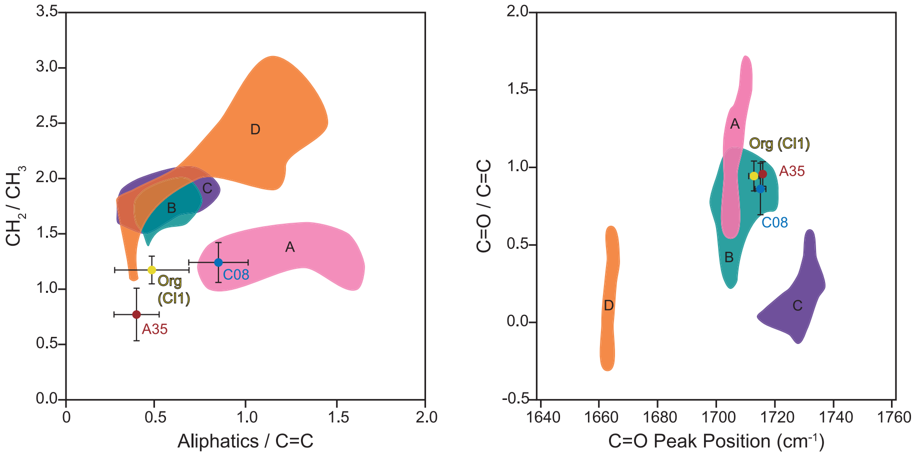

Fig. 21. FTIR vibrational modes for IOM from Ryugu particles and Orgueil (CI1) from this study, isolated via HCl/HF demineralization, and type 1, 2 and 3 carbonaceous chondrites from the literature.72) The groups A to D refer to: A). Type 1 and 2 carbonaceous chondrites that are most representative of their original organic precursors, B). Carbonaceous chondrites that have undergone either low-temperature oxidation or low-grade thermal metamorphism, C). Intense thermal metamorphism with low H_2O activity and D). Intense thermal metamorphism with high H_2O activity. Note that the particle names have the first two zeros removed and aliphatics refers to the sum of the CH_x band intensities.

such a way as to make deconvolution impossible (Fig. SA12). The lower wavenumber region for the Ryugu particles and Orgueil was dominated by modes arising from aromatic and oxygen-containing functionalities, most likely alcohols and/or ethers and ketones71)–73) (Fig. 21). The higher wavenumber region recorded the C-H_x modes arising from the symmetrical and asymmetrical stretching of aliphatic OM and the -OH stretching modes of adsorbed water and hydroxyl groups. However, due to the use of the FTIR instrument in the ambient atmosphere, it was impossible to separate the responses from OH contained within the IOM and that of water from the atmosphere.

Orgueil and the Ryugu particle C0008 were found to record asymmetric C-H_2/C-H_3 stretching ratios similar to other type 1 and 2 carbonaceous chondrites, but Ryugu particle A0035 demonstrated a value that was significantly lower (Table S17 and Fig. SA12). The value for Orgueil is slightly lower than for some previous studies,69),73) but in line with the values reported for another study74) and this likely represents heterogeneity within the meteorite and differences in peak fitting and baseline removal procedures between these studies. The aliphatic abundance, indicated by the summed peak heights of the aliphatic stretching region, to aromatic νC=C ratio is also lower for both A0035 and Orgueil than non-heated type 1 and 2 carbonaceous chondrites, but the value reported for C0008 is similar to these meteorites, and this is due to a low CH_x stretching vibration response for both Orgueil and A0035, compared to that of C0008. The low response may be the result of the low quantity of sample analyzed in this study, the IOM having been isolated from 1.40 mg and 0.983 mg of sample for Orgueil and A0035, respectively and may indicate that C0008 (isolated from 1.90 mg of sample) would have an even higher response if larger amounts of sample were analyzed. Alternatively, the low CH_x stretching vibration response for Orgueil could represent heterogeneity within the Orgueil meteorite or between Orgueil and other primitive type 1 and 2 carbonaceous chondrites. Meanwhile, the C=O/C=C and C=O peak position values for both Orgueil and Ryugu particles A0035 and C0008 are similar to type 1 and 2 carbonaceous chondrites reported previously.72)

4.3.2. The distribution of SOM. The masses of ions detected by DESI-OT-MS for C0008-15 and A0048-10, and Orgueil (CI1) can be found in Table S18 (Ryugu) and Table S19 (Orgueil), respectively, and a representative demonstration of their surface distributions can be found in Fig. 22 (Ryugu, see detail in Figs. SA13 and SA14) and Fig. SA15 (Orgueil). The chemical formulas indicate that the detected SOM are mostly N-containing compounds. The N-containing compounds detected here are likely to be heterocyclic compounds, because the majority of matches for their chemical formulas in the

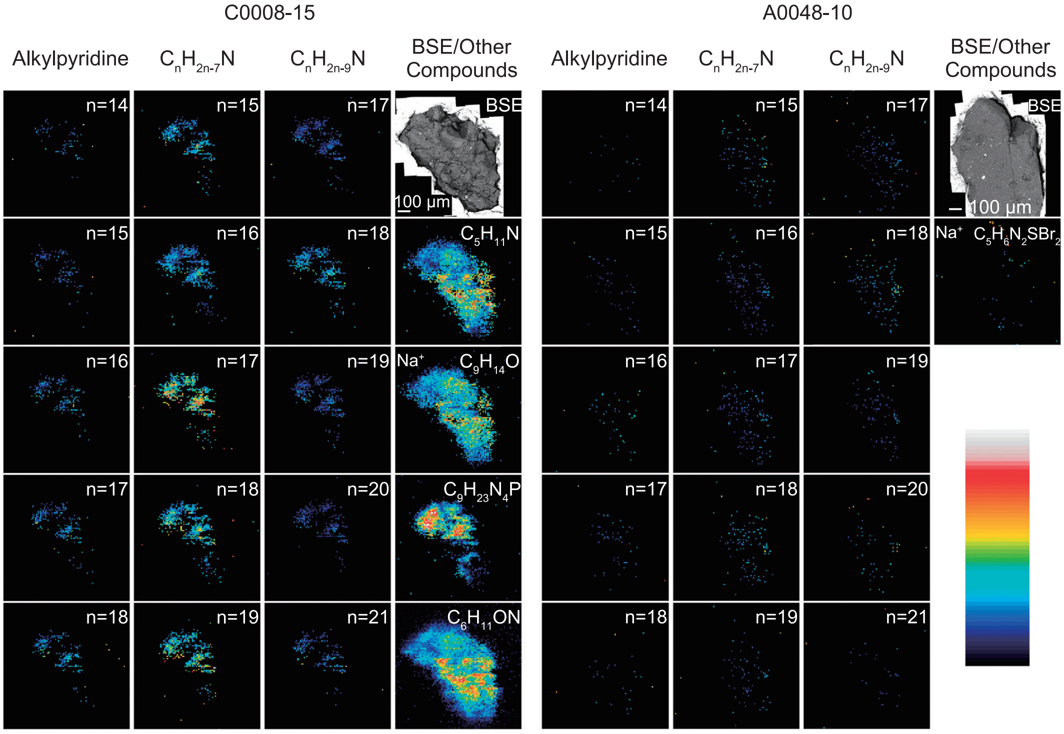

Fig. 22. Representative ion intensity maps from Ryugu particles for the different homologue series and compounds identified, which were normalized to the total ion chromatogram (TIC). Note that the homologue general formula is indicated at the top of each column and the number of C present in each homologue member is represented in the top right corner of each image. For the non-homologue compounds, the chemical formula is indicated in the top right corner of each image and a Na^+ is used to indicate those compounds that were detected as a sodium adduct. For a more detailed representation of the DESI-OT-MS responses of Ryugu particles, please see Fig. SA13 and for the blanks, see Fig. SA14. The color scale has been placed at the righthand side of the figure and it is a rainbow style scale ranging from black (lowest values) to white (highest values).

ChemSpider (https://www.chemspider.com/) and PubChem (https://pubchem.ncbi.nlm.nih.gov/) databases contained heterocyclic moieties in their structures (see details in Supplementary Text ST1.3.7). Furthermore, such compounds were previously reported by a UHPLC-OT-MS study for Murchison (CM2).[75] The presence of N-containing compounds is to be expected, due to the DESI-OT-MS being performed in positive mode, where only compounds that can form positively charged ions are detected. Such an observation is also in agreement with the ubiquitous distribution of N-containing material within the matrix of Ryugu. Nevertheless, some Na adducts were observed for compounds with an O-containing functionality and no N-containing moieties, which would have otherwise not been detected in positive-ion mode.

C0008-15 records many homologue series, including six ($C_nH_{2n-7}N$, $C_nH_{2n-9}N$, $C_nH_{2n-11}N$, $C_nH_{2n-13}N$, $C_nH_{2n-15}N$ and $C_nH_{2n-17}N$) that have not been previously reported by DESI-OT-MS in meteorite samples.[76)–78)] Nevertheless, all homologues detected by DESI-OT-MS here for C0008-15 have been reported previously for Murchison through UHPLC-OT-MS.[75] The UHPLC-OT-MS study identified saturated alkylpyridines ($C_nH_{2n-5}N$) using standards and further tentatively identified alkylquinolines ($C_nH_{2n-11}N$), alkylcarbazoles ($C_nH_{2n-15}N$) and unsaturated alkylpyridines ($C_nH_{2n-5}N$) using tandem mass spectrometry (MS/MS) data and chromatographic information.[75] A0048-10 recorded less of the members of the homologue series found in C0008-15 and one series was not recorded. Furthermore, the surface of A0048-10 yielded a less dense distribution of pixels that gave a response, compared to that of C0008-15.

Meanwhile, although Orgueil may report a response for some of the $C_nH_{2n-7}N$ homologues, the response is very weak and no other homologues were detected in Orgueil. However, Orgueil does record some non-homologue compounds that have not been reported elsewhere. The results show that some compounds can be found in Orgueil that are not present in C0008-15 and A0048-10, and vice versa.

The spatial distribution of homologues in C0008-15 and A0048-10 are clearly demonstrated due to the high resolution of the custom DESI set-up, yielding a 10 µm resolution. The distribution varies between the homologue series detected, indicating that SOM is heterogeneously distributed within the matrix and that its composition is also heterogeneous throughout the sample. In the case of C0008-15, the majority of SOM is concentrated in the top half of the sample, especially in the case of the homologues. Furthermore, SOM homologues and non-homologues demonstrate high-intensity areas within the sample, which are positively correlated in some cases but negatively correlated in others. Such an observation suggests that individual components of the SOM may be sourced from distinct reservoirs. In the case of Orgueil, many of the SOM compounds produce weak signals that make a comparison to C0008-15 and A0048-10 difficult. However, for the SOM compounds that record strong responses, the overall relationships concerning the distribution of SOM are similar to those observed in C0008-15.

4.3.3. Compound specific SOM. Ryugu aliquot (C0008-18) was found to contain at least 23 amino acids and urea and Orgueil (CI1) was found to contain at least 24 amino acids and urea, with tyrosine not being detected in C0008-18, but being detected in Orgueil (Table S20 and Fig. SA16). Alanine and sarcosine and β-aminobutyric and β-aminoisobutyric acid were found to co-elute in both Ryugu and Orgueil samples. As such it is not possible to determine whether there is a contribution from both alanine and sarcosine or β-aminobutyric and β-aminoisobutyric acid to the regions where these amino acids elute in the extracted ion chromatograms (EICs).

Additionally, many peaks were observed in both Ryugu and Orgueil that could not be identified, due to a lack of standards for all the amino acid isomers for a given mass. The unidentified peaks and especially their ratios to one another are different between Ryugu and Orgueil. It is also the case that for the identified amino acids there are clear differences in terms of the ratios between amino acid isomers (Table S21). For example, valine and norvaline are almost 1:1 in Ryugu (ratio of 1.05), but in Orgueil the valine peak is much larger than the norvaline peak (ratio of 7.62). Likewise, in Ryugu the ratio between α-aminobutyric acid and α-aminoisobutyric acid is 0.34, whereas in Orgueil the ratio is significantly higher (0.87).

Another difference between Ryugu and Orgueil is the normalized intensity of their amino acids (Fig. 23). Ryugu records a lower normalized intensity among all amino acids compared to Orgueil. Nevertheless, the overall distribution of amino acids is similar between Ryugu and Orgueil, for example, if one amino acid has a higher intensity compared to another in Ryugu, the same is observed in Orgueil.

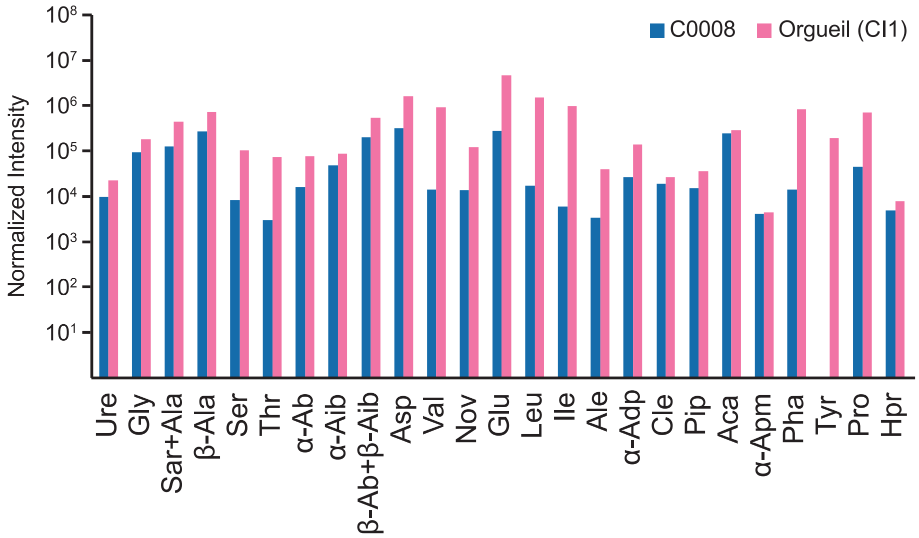

Fig. 23. The amino acids and urea detected in Ryugu and Orgueil (CI1). The intensity of each amino acid was normalized to the sample weight. For the more information concerning the data acquired see Table S20.

5. Discussion

5.1. Nebular components inherited by Ryugu particles.

5.1.1. The carbonaceous vs. non-carbonaceous dichotomy. Concerning the carbonaceous and non-carbonaceous dichotomy, the ε^{54}Cr and ε^{48}Ca values of Ryugu particles indicate that they belong to the carbonaceous group (Fig. 17d), and reveal that the major components of current day Ryugu were probably initially formed in the outer disk reservoirs.[79),80)] The carbonaceous chondrites form a positive trend between ε^{54}Cr and Δ^{17}O (Fig. 17b), a negative trend between ε^{48}Ca and Δ^{17}O (Fig. 17c) and between ε^{54}Cr and ε^{48}Ca (Fig. 17d).[59),60),79)–81)] Ryugu particles plot at the highest ε^{54}Cr and Δ^{17}O values of these trends. It is generally interpreted that the variation in the Δ^{17}O values of early solar system components was ultimately caused by the ultraviolet CO self-shielding effect, which formed ^{16}O-rich CO and ^{16}O-poor H_2O either in the presolar molecular cloud or the early protoplanetary disk.[82),83)] The higher Δ^{17}O values for Ryugu particles relative to carbonaceous chondrites indicate that the Ryugu progenitor body could have formed with a higher amount of the ^{16}O-poor outer solar system component and/or the least abundance of ^{16}O-rich components, such as CAI and chondrules, relative to the parent bodies of carbonaceous group meteorites. Since the Δ^{17}O values of CI chondrites have been modified by terrestrial weathering,[84)] the slight difference in Δ^{17}O values between Ryugu and CI chondrites could have resulted from terrestrial contamination, introduced to CI chondrites during their residence on the Earth.

The heterogeneous inheritance of presolar materials caused the heterogeneity of ε^{54}Cr and ε^{48}Ca among bulk meteorites and their components in meteorites produced by Type Ia and Type II supernovas.[85)–87)] The negative correlation between ε^{54}Cr and ε^{48}Ca values for the carbonaceous group is orthogonal to the trend in the non-carbonaceous group. A similar negative relationship has been identified between ε^{54}Cr and ε^{50}Ti, which was explained due to the mixing of CAI components in the CAI-free protoplanetary disk component defined by the regression line of the non-carbonaceous group meteorites and the Earth.[88)] No significant depletion of volatile lithophile and siderophile elements in Ryugu particles relative to the average CI composition (Fig. 14) was observed. Furthermore, Ryugu particles containing D, ^{13}C and ^{15}N-rich OM likely inherited their isotopic characteristics from material formed in either the interstellar medium (ISM) or outermost part of the PSN. Together, the aforementioned observations demonstrate that the solid from which Ryugu formed suffered little fractionation with the gas during heating within the protoplanetary disk, similar to the solid from which CI chondrites formed.[89)] Among the available meteorite groups, ureilite represents an end-member composition of the inner-disk dust reservoir that was depleted in ^{54}Cr and ^{48}Ca through thermal processing, at least 0.1 Myr after CAI formation.[61),90)] Thus, the ε^{54}Cr and ε^{48}Ca values of protoplanetary material could be controlled by mixing of at least three components: (1) a highly thermally-processed endmember (ureilite-like), (2) an endmember that has experienced low thermal processing (Ryugu-like) and (3) a refractory solar system component, such as CAIs.

The isotope mixing curves determined by the above assumption are shown in Fig. 17d (all the parameters used for the calculations are given in the figure caption). As the normalized elemental abundance patterns for refractory lithophile elements was found to deviate from that of CI chondrites for A0022, the ε^{54}Cr and ε^{48}Ca values of C0081 were used as the representative compositions for Ryugu. By this assumption, the ε^{54}Cr and ε^{48}Ca values of CO, CV, CM, and Tagish Lake (C2 ungrouped) can be explained by adding ~1 to 4 wt% of CAIs while CR, CI, and ordinary chondrites (OC) can be explained by the addition of $\leq$0.1 wt% of CAIs. These estimated values are nearly consistent with the actual modal abundance of CAI in the carbonaceous and ordinary chondrites: CV (3 vol%) $>$ CO (1 vol%) $>$ CM (1.2 vol%) $>$ Tagish Lake (estimated as ~1 vol%) $>$ CR (0.12 vol%) $>$ CI ($\ll$0.01 vol%), OC ($<$0.2 vol%), and enstatite chondrites (EC) ($<$0.1 vol%).[91),92)] Such a result further suggests that the ε^{54}Cr and ε^{48}Ca values of Earth, Mars, and aubrites, plotted above the ureilite-Ryugu line in Fig. 17d, could also be explained by the addition of CAI components.

5.1.2. Inheritance of B and Be from ISM and/or PSN materials. The inheritance of unmodified ISM materials in the Ryugu particles is evidenced by the B and Be compositions of TD2 particles. As mentioned previously (in section 4.2.1), the negative correlation between [B] and [Be] in the TD2 particles (Fig. 15a) cannot be explained by either progenitor body or condensation processes. As such, the variation of [B] and [Be] in TD2 particles must be attributed to the involvement of at least two chemically distinct reservoirs in the materials that formed the Ryugu progenitor body. Solar Be and B were produced by two processes, 1) the interaction of galactic cosmic rays with ISM materials and 2) neutrino (ν)-nucleosynthesis in massive star explosions. As such, all ^{9}Be, all ^{10}B, and ~70% of ^{11}B were produced by the former and ~30% of ^{11}B by the latter process.[93)–95)] Thus, the negative correlation of [Be] and [B] may indicate the inheritance of primordial components having distinct B/Be formed by the above processes in the ISM or outer PSN.

Since spallation processes form ^{10}B and ^{11}B, and massive star explosions only form ^{11}B, ^{11}B/^{10}B may elucidate the relative contribution of these processes to different samples and the distinct components that formed them. However, there is no difference in ^{11}B/^{10}B between the ^{15}N- and D-rich micro-OM (^{11}B/^{10}B ≈ 4.0), which may have formed in the ISM or outer region of PSN, and the ^{15}N- and D-poor matrix (^{11}B/^{10}B ≈ 3.9) analyzed in this study (Fig. 11). The ^{11}B/^{10}B for different extraterrestrial environments are all similar, including the solar value (4.0–4.1),[96)] interstellar diffuse clouds (3.4 ± 0.7),[97)] and early B stars ($4.7^{+1.1}_{-1.0}$ and $3.7^{+0.8}_{-0.6}$).[98)] Therefore, based on the above evidence, even if components with [B]/[Be] from different nucleosynthetic processes are mixed in the local ISM, the ^{11}B/^{10}B of the components that formed Ryugu would have obtained similar values before their accumulation/condensation.

As mentioned above the B/Be among Ryugu components is heterogeneous. The reason for the existence of this heterogeneity in the primordial components of Ryugu particles is not clear. However, the critical finding is that the TD2 particles inherited the primordial material derived from the ISM, without undergoing any modifications in the solar nebular or under progenitor body conditions. Consequently, the elemental abundances of TD2 particles are likely to represent the involvement of two end-member components, with one of these components representing PSN material that has undergone the least thermal processing. The origin of the other end-member component is unclear but may represent a distinct component in the ISM.

TD1 particles do not show a [B]-[Be] correlation, instead these particles display a scattered distribution in Fig. 15a. Such a distribution could be related to a progenitor body process, but this will be discussed later.

5.1.3. O isotope heterogeneity from accreted ice preserved in Ryugu particles. The TD1 particle A0022 records heterogeneity in the isotopic composition of its fluid compared to other TD1 particles. The δ^{18}O value of A0022 is >1‰ higher than the other Ryugu particles. However, the [H] and δD values of A0022 are not significantly different from the values of the other particles. Thus, the elevated δ^{18}O value of A0022 was unlikely to arise from differences in the degree of aqueous alteration, compared to the other Ryugu particles. Instead, the distinct δ^{18}O value of A0022, compared to the other Ryugu particles, may relate to its high modal abundance of carbonate (Fig. 2), higher bulk [REE] (Fig. 14), distinctly high $\delta^{13}C_{TC}$ value (Fig. 16c), and the higher δ^{18}O values of carbonate and magnetite present in this particle (Fig. 8). Whereas, another Ryugu particle A0033 demonstrates a similar modal abundance of carbonate (Table S2), but a lower δ^{18}O value (Fig. 17a). Thus, the higher δ^{18}O value of A0022 is not only explained by the higher modal abundance of carbonate. Instead, the fluid during aqueous alteration must have contained a higher δ^{18}O value, which could have originated from an ^{18}O and ^{13}C enriched CO- or CO_2-rich phase. Thus, the differences in the bulk δ^{18}O value of A0022 from other Ryugu particles can be explained if A0022 accreted ice components, which had higher amounts of CO or CO_2 compared to that in the other particles. Furthermore, the enrichment of carbonate nodules and an absence of carbonaceous nodules in A0022 may imply that the OM within this particle was oxidized via fluid-rock interaction processes.[99)]

Furthermore, the Δ^{17}O values of magnetite and dolomite are higher than that of bulk Ryugu. Such a difference may indicate that the fluids, which caused the widespread aqueous alteration in Ryugu particles, were more elevated in Δ^{17}O relative to the anhydrous silicate materials accreted by the Ryugu progenitor body.

5.1.4. Inheritance of OM from the ISM and/or PSN. The heterogeneous distribution of δD, δ^{13}C and δ^{15}N causes significant variations in the bulk H-C-N isotopic compositions of the Ryugu particles (Figs. 10, 11, and 16), with the regions associated with ^{15}N-hotspots or ^{15}N-coldspots being the major controllers of the bulk C, H, and N isotopic compositions. Such ^{15}N-hotspots or ^{15}N-coldspots are associated with micro-OM in the matrix. Furthermore, whilst the ^{15}N-hotspot from A0073-5 (δD $= 2983 \pm 84$‰ and δ^{15}N $= 610 \pm 78$‰, Fig. 11) is enriched in D (correlated δD and δ^{15}N), the ^{15}N-coldspot in C0053-1 (δD $= 158 \pm 30$‰ and δ^{15}N $= -147 \pm 10$‰, Fig. 10) records a δD value within the bulk Ryugu range (negatively correlated δD and

δ^{15}N). Correlated D and ^{15}N enrichments in IOM have been proposed to originate from interstellar photochemistry involving the organic-rich ice mantles of dust grains.[100)–103)] The highest δ^{15}N values, reaching up to ∼4000‰, are reported in the matrix of CB/CH-like chondrites.[104)] The ^{15}N-hotspots are typically found in the IOM of primitive meteorites[105)] and interplanetary dust particles (IDPs),[106)] as well as in the nano-OM globules of the Tagish Lake and Bells (C2 ungrouped) meteorites.[107),108)]

However, like Ryugu negatively correlated δD and δ^{15}N values are observed in carbonaceous chondrites and this suggests that the ion-molecule reactions, indicative of the ISM and outer PSN, might not be the sole contributor of IOM H and N.[109),110)] An alternative explanation for the ^{15}N enrichments could be the photodissociation of N_2 in the solar nebular or ISM, which can give very high δ^{15}N values (up to 13400‰).[111),112)] In light of the potential for both PSN and ISM origins for IOM D and ^{15}N, it is possible that multiple IOM sources contribute to the H-C-N isotopic signatures observed in Ryugu and carbonaceous chondrites.

Micro-OM, such as that discussed above, cannot be distinguished from the surrounding matrix via Raman spectroscopy, likely due to the presence of ubiquitous sub-µm-sized OM. In this respect and in terms of their Raman D-band/G-band intensity ratios (Fig. 20b), most Ryugu particles are similar to other primitive extraterrestrial samples, including the Orgueil (CI1) and, Murchison and Murray (CM2) carbonaceous chondrites. The Raman response of Ryugu and chondritic meteorite OM is likely to arise almost entirely from the refractory organic matter (ROM) portion of IOM.[70)] The ROM fraction of IOM is aromatic rich and heteroatom poor, in comparison to the labile organic matter (LOM) fraction, which is less aromatic rich and thought to break down during aqueous alteration to form some SOM compounds.[113),114)]

Currently, it is still unclear what mechanism formed ROM-like OM in the matrix of Ryugu, as well as in chondritic meteorites. Previous studies have argued for origins of IOM prior to[33),115)] or during parent body processing.[116),117)] Of the studies that have argued for a pre-parent body origin of IOM, several have proposed an origin in the PSN via plasma discharge style reactions.[110),115),118)] Such studies were able to simulate some of the hydrogen and noble gas isotopic fractionations observed in carbonaceous chondrites, including D hotspots and coldspots, but not the ^{15}N enrichments or ^{15}N-hotspots and coldspots. Nevertheless, plasma discharge experiments have not yet demonstrated that the elemental abundances and functional group chemistry of the synthesized IOM are within the range displayed by meteoritic IOM. Alternatively, some portion of IOM could have been synthesized as mentioned above through ion-molecule reactions and subsequent photochemistry involving the ice mantles of dust grains within the ISM or outer PSN.[100)–103)] Meanwhile, it is also possible that, like the amino acids, the IOM of Ryugu could have formed *in situ* through aqueous alteration involving primitive organic precursor compounds.[116),117),119)] As such, multiple origins for the IOM of Ryugu are possible and it is likely that several of the above processes have contributed to the origination of current day Ryugu OM.

The morphologies and textures associated with the micro-OM and nano-OM reported here are suggestive of IOM that was deposited after the melting of ice or which formed *in situ* from simpler organic precursors and infilled pore spaces.[120),121)] The OM may have been partially mobilized during aqueous alteration, allowing the relocation of OM to fill the pore spaces and yield OM regions up to 10's of µm in size. Alternatively, if aggregates of OM rich material were accreted then these could also explain the µm-sized OM regions observed here. Furthermore, the sharp contacts between the carbonaceous nodule in C0053-1 and the surrounding matrix (Fig. 7a) could indicate that the initial OM bearing material was accreted into the matrix during the formation of the Ryugu progenitor body and subsequently aqueously altered. On the other hand, the carbonaceous nodule could have joined after the main phase of aqueous alteration and represent an exogenous component.

5.2. Progenitor body/asteroidal processes recorded in Ryugu particles.

5.2.1. Density and porosity measurements: implications for the formation of Ryugu. The textural characteristics and elemental abundances of the 16 Ryugu particles are comparable and controlled by the voids and sub-µm-sized particles in their phyllosilicate-dominated matrix (*e.g.*, Table S3 and Fig. SB). The Ryugu particles on average are composed of 41 vol% voids, 9 vol% coarse-grained (∼100 µm) components, and 50 vol% matrix on average, which yields a bulk density of 1530 kg m^{-3} and a porosity of 41%, as mentioned in section 4.1.2. The average porosity estimated in this study supports the porosity inferred from the thermophysical models of Ryugu surface material (30–52 vol%).[122] The formation of sub-µm-sized voids in the matrix likely relates to the original presence of ice in those spaces that have subsequently been lost through sublimation. If such a hypothesis is correct, then the water to rock ratio should be $\gtrsim$0.7, after the main phase of aqueous alteration.

To understand how the current mineral assemblage (except for the olivine and low-Ca pyroxene) of the Ryugu particles formed, a thermodynamic calculation was performed using the geochemical thermodynamics software PHREEQC version 3.[123] The calculation used the average bulk composition of Ryugu particles (Table S12), the equilibrium temperature at the end of aqueous alteration, the initial anhydrous mineral assemblage determined for a CI composition[124],[125] and self-gravity, porosity, pressure, and water-to-rock ratio values.[126] The temperature at the end of aqueous alteration was input as 0–30 °C, which was based on O isotope thermometry (Table S9). The aforementioned values were used as inputs in physical modeling to simulate the conditions capable of reproducing the current day Ryugu mineral assemblage and their modal abundances. For a progenitor body of radius 1–10 km, a minimum water-to-rock ratio of 0.35 is required. For a progenitor body of radius 28–40 km, a minimum water-to-rock ratio of 0.5–1.0 is required. The water-to-rock ratio is consistent with the water-to-rock ratio of $\gtrsim$0.7, estimated on the assumption that the voids, which define the porosity of Ryugu, were fully occupied by ice.

Furthermore, to achieve the bulk density of the asteroid Ryugu ($1190 \pm 20\,\mathrm{kg\,m^{-3}}$)[9] using materials with densities equivalent to the particle measured in this study ($\sim 1530\,\mathrm{kg\,m^{-3}}$), approximately 22% of macroporosity is required. The macroporosity estimated here suggests that current day Ryugu contains either macro-void space relating to its rubble pile structure or less dense material within its interior, such as ice. In the latter hypothesis, Ryugu may represent a dormant cometary nucleus or fragment of an icy planetesimal.[6],[127],[128] Indeed, some of the near-Earth asteroids are thought to be extinct/dormant nuclei of comets that no longer experience outgassing.[129]–[133]

5.2.2. The geochemical differences between the TD1 and TD2 sites. Particles from the TD1 site demonstrate differences in several geochemical data when compared to those of the TD2 site (Figs. 14, 15, 18, and 19), which can be attributed to geological differences among the sampling sites. It was found that the abundance of phosphate minerals significantly contributed to the heterogeneous bulk trace element abundances of the TD1 particles. Mass balance calculations demonstrate that the addition of up to 1 wt% apatite to A0048 reproduces the enrichments of REE observed in A0022 (Fig. SA17). However, to account for the low [P], [Y], and [REE] of A0085 compared to A0048, the absence of a phase containing an excess of [LREE] and [HREE] and a deficit of [P], [Sr], [Y], and [MREE] is required (Fig. SA17). The modal abundance of phosphates (Fig. 2 and Table S2) is poorly correlated with [P] in these particles (Fig. 14 and Table S13). Practically, phases >1–2 µm in size were counted in the modal analysis; if sub-µm-sized phases such as precursors of hydroxyapatite and amorphous phosphate compounds in the matrix are enriched in REEs, these unidentified phases would control the variation of the elemental abundances.

Apatite crystals fringed with phyllosilicates lacking apatite were observed in A0033 (Fig. 3d), whilst secondary Fe-sulfides were observed in A0035 (Fig. 5f). Such an observation suggests that P-bearing components, originally present within the now phosphate-component-poor phyllosilicate material, may have been dissolved by fluids to yield the large apatite grains in A0033. Meanwhile, S-bearing components present in the matrix, associated with the void spaces of A0035, would have led to the formation of the Fe-sulfides, which infilled these voids. However, such textures were not observed in TD2 particles, with the TD2 particles appearing much more uniform in terms of their textural characteristics overall, when compared to TD1 particles. The above observations and interpretations suggest that some TD1 particles recorded migration of P and S beyond the sample scale (mm), but this was not observed for TD2 particles. Furthermore, the scattered variation of [B] *vs.* [Be] for the TD1 particles (Fig. 15a) could be explained by migration of B beyond the sample scale, because the solubility of B in an aqueous fluid is much higher than that of Be. Accordingly, the elemental abundances would be expected to vary more among the TD1 particles, compared with the TD2 particles, which is what is observed here (Figs. 14a and 14b). This observation suggests that the TD1 particles include materials that experienced more heterogeneous aqueous alteration, compared to the TD2 particles. Accordingly, since the major phase of aqueous alteration occurred prior to or at 2–3 Myr after the formation of CAI (Fig. 13), the two sites could have inherited materials that were modified to different degrees by aqueous alteration on the Ryugu progenitor body.

If the geochemical differences in the particles are related to the current locations of the TD1 and TD2 sites, the cause must be found in more recent events on the surface of Ryugu, than the period during which aqueous alteration occurred. A numerical simulation[127)] suggested that current day Ryugu could have originated from a porous cometary nucleus composed of rocky fragments and OM, with sublimation of water ice, occurring over a geologically short interval (*e.g.*, 0.05–1 Myr), giving rise to its spinning top-shape and rubble-pile structure.

In such a scenario, fractures associated with thermal stress[134)] could have led to the release of jets associated with ice sublimation near the TD1 site. The jets would be formed of water vapor, other volatiles, and interior dust[134),135)] from multiple depths. While a portion of the jet material would be lost to space, some could be deposited onto the surface and sintered by the refreezing of volatiles.[136)] The sintered dust and ice could thus form layers that covered the surface of the comet-like Ryugu near to the fractures. An experimental study revealed that phyllosilicate sublimation residues form a porous and cohesive structure, which allow the passage of volatiles, such as those arising from sublimation.[137)] Accordingly, some portion of the dust layers could remain behind after the complete sublimation of surface ice. Cycles of sublimation and re-deposition could form a layered structure, which would locally include aqueously altered particles from the interior of the Ryugu cometary nucleus, possibly representing TD1-like particles. Subsequent voids generated between the dust layers and the thermal stress fractures that generated the jets, could lead to the fragmentation, collapse and brecciation of earlier-consolidated thin layers to form slab-like fragments, which would eventually be deposited on the surface.

On the other hand, TD2 material could represent more massive layers of dust deposited from ice simply by sublimation, without the influence of jets and thus represent material sourced from a more similar region of the comet-like body. Indeed, the video footage of the two Ryugu sampling sites demonstrates a much higher density of slab-like material at the TD1 site, compared to the TD2 site, suggesting that the TD1 site may contain a larger amount of the post-sublimation dust layer materials and possibly be more physically disturbed.

In other words, the geochemical difference between the TD1 and TD2 sites could be related to the presence of particles sourced from varying depths and lithologies inside the progenitor body of Ryugu for the TD1 site, but from a more constrained region for the TD2 site. During the fracturing and jetting processes and the cycles of sintering and sublimation, exogenous materials perhaps derived from micrometeorite impacts could also be incorporated into the dust layers and thus the Ryugu particles. The exogenous material could represent the olivine fragments of chondrules and AOA reported here and potentially the massive domain from A0035. Subsequently, during collection at the TD1 site surface slab-like material recording the influence of sublimation jets was collected, but at the TD2 site more subsurface material without the influence of jet processes was sampled.

5.2.3. Geological processes operating on the Ryugu progenitor body/asteroid. The variation in surface morphology and internal texture among the Ryugu particles provides clues that enable an understanding of the processes that have affected the components of Ryugu from their accretion up until the formation of the current day asteroid Ryugu. The irregularly-cracked surface, and the striated and curved smooth surfaces (Figs. 1a to 1d) are products of contrastive stress fields with compression-extension, and shearing, respectively. Particularly, the curved smooth surface implies that it has formed under a moderate confining pressure. Furthermore, the planar fractures on a TD2 particle (Fig. 1b) suggest that the uncovered interior of Ryugu has also been modified in texture, but retained its primordial chemical composition. As for the internal texture, the distinctive massive domains in the matrix (Figs. 1e and 1f) are representative of a structure formed when a stiff layer and its weaker matrix are subject to layer-parallel extension, or layer-normal shortening, such as pinch-and-swell structures. The phyllosilicate-dominated matrix is foliated along the boundary with the massive domain (Fig. 6a). The above surface and internal textures, which are common to both the TD1 and TD2 particles, are comparable to the textures in terrestrial permafrost soils, which are caused by alternating freeze-thaw cycles, as suggested for the evolution of the Orgueil (CI1) parent body.[138)] Thermal fatigue is a known mechanism of rock weathering and fragmentation, producing the regolith structure of small asteroids,[*e.g.*, 139)] but is unlikely to cause the smooth and planar textures in the phyllosilicate-dominated matrix of Ryugu particles.

The coarse-grained components (*e.g.*, nodules) in the Ryugu particles vary in size and chemistry and are scattered in the matrix, but adjacent to one another within a few 10's of µm (*e.g.*, Fig. 5a). The magnetite nodules are composed of magnetite grains with different crystal habits, and framboidal magnetite, of different sizes, cluster at the ~10 µm-scale (Figs. 5b, 6d, and 6e). To produce these objects, which could not have formed at the same time in the same system, it is likely that multiple isolated systems with differing bulk compositions are necessary. Therefore, an individual cluster of magnetite with a specific crystal habit represents one system, which would have been isolated temporally from the others and can thus be spatially related. Accordingly, each isolated system individually regulates its own crystal nucleation and growth, likely during repeated freeze-thaw cycles, as described above. Ice crystals nucleate and grow in the freeze-thaw cycles, pushing the matrix constituents including amorphous silicate and phyllosilicate particles out of the way and compressing them. As the matrix heats up and the ice melts, an open space filled with fluid is formed where nucleation and growth of magnetite, carbonate, and inter-crystalline phyllosilicate can occur. At the start of the next cycle, crystals could have been redissolved, either fully or partially. The partially dissolved crystals could then later grow as the fluid cooled down. In this way larger crystals could grow over multiple cycles, with the smaller crystals representing nucleation in the final cycle recorded by the Ryugu progenitor (Figs. 5b and 5c). Such a process is termed Ostwald ripening.140) In this way, the complex textures of the coarse-grained components, such as magnetite-carbonate nodules, could have been formed at the scale of 1 to 10's of µm, under low temperatures of 0–30 °C.

On the other hand, the Ryugu particles are dominated by their phyllosilicate-matrix, which is mainly composed of homogeneous, sub-µm-sized components. This observation indicates the Ryugu progenitor body experienced pervasive, aqueous alteration. However, the overall chemical homogeneity of the Ryugu particles indicates that element migration during aqueous alteration should have been limited, even for fluid-mobile elements, for them not to migrate beyond the mm-scale. The only exceptions are for the cases of the P- and S-bearing sub-µm-sized components in some of the TD1 particles. Such a finding suggests that the building blocks of the Ryugu progenitor body would be mechanical mixtures of icy components that were uniformly mixed with lithic components at the sub-µm scale, but with very limited high-temperature products from the inner solar system, such as chondrules and CAIs. In addition, to achieve the freeze-thaw cycles, the system must be maintained under sufficient pressure and temperature conditions around the freezing point of the fluid within the body. One of the possible environments to satisfy these requirements is an icy planetesimal that formed outside of the water snow line.

Numerical simulations of the thermal evolution of icy planetesimals have revealed that an icy planetesimal 10's of km in size could achieve melting of ice through the heat supplied by radioactive nuclei (*e.g.*, ^{26}Al) contained within its rocky components, which would lead to pervasive aqueous alteration of the interior.*e.g.*, 141) Moreover, as suggested by the analysis of SOM reported here (see section 5.2.6 in detail), if the icy components of Ryugu were composed of not only pure H_2O, but also ammonia and other chemical species, the aqueous alteration could have proceeded at lower temperatures below the freezing point of pure water.142)

After the radioactive nuclei had sufficiently decayed, the thermal boundary between the outer domain of ice-rich components and the inner domain of water-rich components would migrate inward, causing the icy outer domain to grow inwards and the ice-to-water volume to increase. The water-rich inner domain contains vast quantities of phyllosilicates produced by aqueous alteration of anhydrous materials. The high porosity of the Ryugu particles, composed mainly of phyllosilicates, suggests that the Ryugu progenitor body would have a water-rich inner domain with a high water-to-rock ratio $\gtrsim$0.7, even after aqueous alteration. The phyllosilicates, loosely distributed in the water-rich domain, would have been pressed by the outer ice-rich domain that had grown inward. As a result, the phyllosilicates would be compressed against the coarse-grained components, until the interior of the Ryugu progenitor body froze completely. During this cooling period, the slab-like materials characteristic of the TD1 site and the layered structures on the surface of current Ryugu could have been formed.

A nanoscale paleomagnetic study on the framboidal magnetite in Tagish Lake (C2 ungrouped) suggests that the framboidal magnetite nanoparticles could have been formed, not during the main stage of aqueous alteration, but from the last droplets of aqueous solution just before the complete exhaustion of water in a local system within a hydrous parent body.24) In such a scenario, the phyllosilicate-dominated matrix of Ryugu particles would have been formed during the main stage of aqueous alteration, while the coarse-grained components such as the magnetite nodules could have been formed during cooling after exhaustion of the planetesimal's heat source. Furthermore, the formation of phyllosilicates, such as serpentine-group minerals, via aqueous alteration is a hydration reaction, which would produce further heat for ice to melt or water to remain liquid, and so once ice began to melt, this could result in the pervasive aqueous alteration observed in Ryugu particles.[*e.g.*, 141] On the other hand, supersaturation of magnetite and carbonate components in the aqueous solution and their precipitation during the cooling stage could have caused the chemical compositions of the aqueous solution remaining in the local systems to vary. As a result, icy grains in the muddy matrix and droplets of aqueous solution in the frozen matrix could coexist, which corresponds to the textures characterized by the freeze-thaw cycles observed in this study. Accordingly, the freeze-thaw cycles would have been associated with the migrating location of the thermal boundary zone near the freezing point of the aqueous solution within the Ryugu progenitor body.

5.2.4. Exposure to solar wind and cosmic ray. Like other extraterrestrial materials, Ryugu particles contain Ne of at least three origins. The first type of Ne originated through spallation of Ryugu material by a combination of solar and galactic cosmic rays and is referred to as cosmogenic Ne. The second type of Ne is that which became trapped within components when they formed, prior to their accretion within the Ryugu progenitor body, and is referred to as trapped Ne. The third type of Ne was formed through implantation by solar wind (SW) either in the early solar system (*e.g.*, in chondrites[64]) or in more recent times (*e.g.*, in lunar regoliths[143]). This study found a massive domain in particle A0035, which was lighter in color than the encapsulating matrix. Dark- and light-colored domains in Nogoya (CM2) were also analyzed previously.[64] It was found that the dark-colored domains in this meteorite, which correspond to the matrix in this study, were characterized by SW Ne and that the light-colored domains were characterized by Ne with lower ^{20}Ne/^{22}Ne. Ne in aliquots from the matrix and the massive domain in this study show the same isotope characteristics (Fig. 18).

Contributions of the three types of Ne were estimated as abundances of SW Ne ($[\mathrm{Ne}]_{\mathrm{SW}}$), cosmogenic Ne ($[\mathrm{Ne}]_{\mathrm{cos}}$), and trapped Ne ($[\mathrm{Ne}]_{\mathrm{trap}}$) (Tables SA22 and SA23, see Supplementary Text ST1.4.11 for details concerning the estimation calculation). $[\mathrm{Ne}]_{\mathrm{SW}}$ is dominant in most particles, and $[\mathrm{Ne}]_{\mathrm{SW}}$ relative to $[\mathrm{Ne}]_{\mathrm{total}}$ ranges from 57 to 95%, except for A0033-14, A0033-13, A0035-10, and A0035-8 where it is 7, 15, 32, and 35%, respectively. A0035-10 and A0035-8 are aliquots of the massive domain, and $[\mathrm{Ne}]_{\mathrm{trap}}$ relative to $[\mathrm{Ne}]_{\mathrm{total}}$ for these aliquots is estimated to be 79 and 85%, which is the highest among the Ryugu particles.

The $[\mathrm{Ne}]_{\mathrm{SW}}$ calculated for Ryugu particles does not correlate with the level of irradiation indicated by Raman spectroscopy (Figs. 18d and 20a). However, the position and width of the G-band peak of OM does correlate with the $[\mathrm{Ne}]_{\mathrm{cos}}$, with the exception of two outliers, A0035 and A0078. As such, differing amounts of cosmic ray exposure, relating to the depth of a particle within the Ryugu regolith, would seem to be responsible for the different levels of irradiation experienced by the OM in Ryugu particles. Whereas, normal solar wind irradiation is not linked to the differences in irradiation observed between Ryugu particles, likely due to the limited penetration depth of this style of irradiation (<500 nm[63]).

Accordingly, the variation in $[\mathrm{Ne}]_{\mathrm{SW}}$ observed between Ryugu particles cannot be explained by the irradiation they experienced at the surface of current day Ryugu. Instead, the differences likely relate to the initial $[\mathrm{Ne}]_{\mathrm{SW}}$ individual Ryugu components experienced prior to their accretion within the Ryugu progenitor body. Subsequently, aqueous alteration may have mobilized Ne contained within these phases for TD1 site particles evidenced by their negatively correlated [Lu] and [Ne] (Fig. 19), in line with the observation that TD1 site particles experienced more heterogenous aqueous alteration. After the formation of the current day Ryugu the $\mathrm{Ne}_{\mathrm{cos}}$ signatures of Ryugu particles were overwritten by cosmic ray exposure near the surface of Ryugu, but the limited penetration depth of $\mathrm{Ne}_{\mathrm{SW}}$ meant that the $\mathrm{Ne}_{\mathrm{SW}}$ could not be overwritten. The only exceptions being for A0078 and A0085, which may have been at the very surface of Ryugu. Nevertheless, both A0078 and A0085 record large negative [HREE] anomalies relative to CI chondrites, which indicates that they were highly modified by aqueous alteration. As a result of the above phenomena, the TD1 particles maintain their negatively correlated [Lu] and [Ne], and the $[\mathrm{Ne}]_{\mathrm{SW}}$ for Ryugu particles does not correlate with their irradiation signatures indicated by Raman spectroscopy.

Due to the comprehensive geochemical analysis of Ryugu particles reported here, including the acquisition of Ne isotope and [Ne] data, it is clear that some Ne was inherited by the Ryugu progenitor body from its accreted components. As such it is impossible to separate the ancient inherited Ne from the recently acquired Ne on the surface of Ryugu. Therefore, cosmic ray exposure (CRE) ages will not be discussed here. Nevertheless, CRE ages were calculated and are reported in the Supplementary Text ST1.4.11.

5.2.5. Evolution of OM on the surface of Ryugu. The surface of Ryugu has been exposed to the conditions of space within our solar system and thus records the effects of solar irradiation. The albedo characteristics for Ryugu were found to be indicative of the space weathering of organic and silicate materials.6) Accordingly, the TD1 particles, which were collected from the surface of Ryugu, have an increased Raman G-band FWHM and decreased D/G value compared to TD2 particles (subsurface ejecta collected from near the artificial crater formed by the SCI) (Fig. 20). Bruenetto *et al.*68) demonstrated that the G-band peak position tended to be lower and the corresponding FWHM larger after organic molecules were altered by energetic particle irradiation. As such, the observations from Raman spectroscopy are consistent with the TD1 particles having been collected from the surface of Ryugu and having experienced the effects of space weathering.

While the penetration depth of most solar wind particles is limited to depths of 1 µm or less, and thus it may be difficult to affect the OM in an entire ~mm-sized sample with such particles alone, high-energy particles present in the solar cosmic rays are able to penetrate to depths of several cm.62),144) As such, if the flux of high-energy particles were enough, then the interiors of the TD1 particles could have been altered by space weathering in sufficient amounts to explain the observations reported here.

Similarly, the DESI-OT-MS responses for a particle from TD1 (A0048-10) and TD2 (C0008-15) are different, with the TD1 particle recording less members of a given homologues series and one less homologue series. Lower densities of pixels showing a response were also recorded for the TD1 particle. Such observations could be explained by the destruction of some SOM in the TD1 particles through the effects of solar irradiation.

The asymmetric $C\text{-}H_2/C\text{-}H_3$ stretching ratio of isolated IOM, determined by FTIR spectroscopy, for C0008 (1.24 ± 0.18) is similar to that of Orgueil (CI1) (1.17 ± 0.13). However, the ratio for A0035 (0.77 ± 0.24) is lower than any carbonaceous chondrite (1.1–2.6)69),72) and indeed the ISM value of between 2.0 and 2.5145),146) and the IDP range of 1.0–5.6.147),148) Such an observation is difficult to explain through either a difference in the peak fitting procedures or potentially those relating to the low quantity of aliquot used, because Orgueil (analyzed by this study) records an asymmetric $C\text{-}H_2/C\text{-}H_3$ stretching ratio in line with previous studies (Fig. 21). Therefore, Ryugu particle A0035 may contain IOM that is distinct form that of carbonaceous chondrites and C0008. One potential reason could be that the particle received large amounts of irradiation that could have preferentially destroyed aliphatic CH_2 bonds and thus created an IOM that contains aliphatic material either shorter in chain length or less branched than that which is found in type 1 or 2 carbonaceous chondrites. Accordingly, irradiated IDPs were found to have decreased $C\text{-}H_2/C\text{-}H_3$ ratios compared to their values prior to irradiation.149) Such irradiation could have occurred on Ryugu, due to the particle originating from the surface of Ryugu (TD1).

5.2.6. Evolution of SOM on the Ryugu progenitor body.

Nitrogen heterocycles. The results reported here for DESI-OT-MS indicate that Ryugu (Fig. SA13) is rich in N-containing heterocyclic SOM compounds, yielding the highest number of homologues identified by a DESI-OT-MS study to date. Some N-containing heterocyclic compounds, such as pyridine and quinoline, have been proposed to form in ice grains that were exposed to UV irradiation in either interstellar or circumstellar environments.150) Although it may be possible that subsequent irradiation could create the more complex alkylated homologue series reported here, as is the case with polyaromatic hydrocarbons,151) such a phenomenon has not been demonstrated experimentally for N-heterocycles. Alternatively, it is possible that the alkylated homologue series formed as a result of aqueous processing on Ryugu (Fig. 24). Indeed, alkylpyridines in Murchison (CM2) have been theorized to form as a result of Chichibabin synthesis (a Fischer-Tropsch type synthesis) involving aliphatic aldehydes and ammonia.152),153)

In comparison to Orgueil (CI1) (Fig. SA15), the Ryugu aliquots C0008-15 and A0048-10 record a much larger array of N-containing heterocyclic compounds and appear more similar to Murchison in terms of the homologues identified.75),78) A greater diversity of homologues for C0008-15 and A0048-10 compared to Orgueil indicates a significant difference

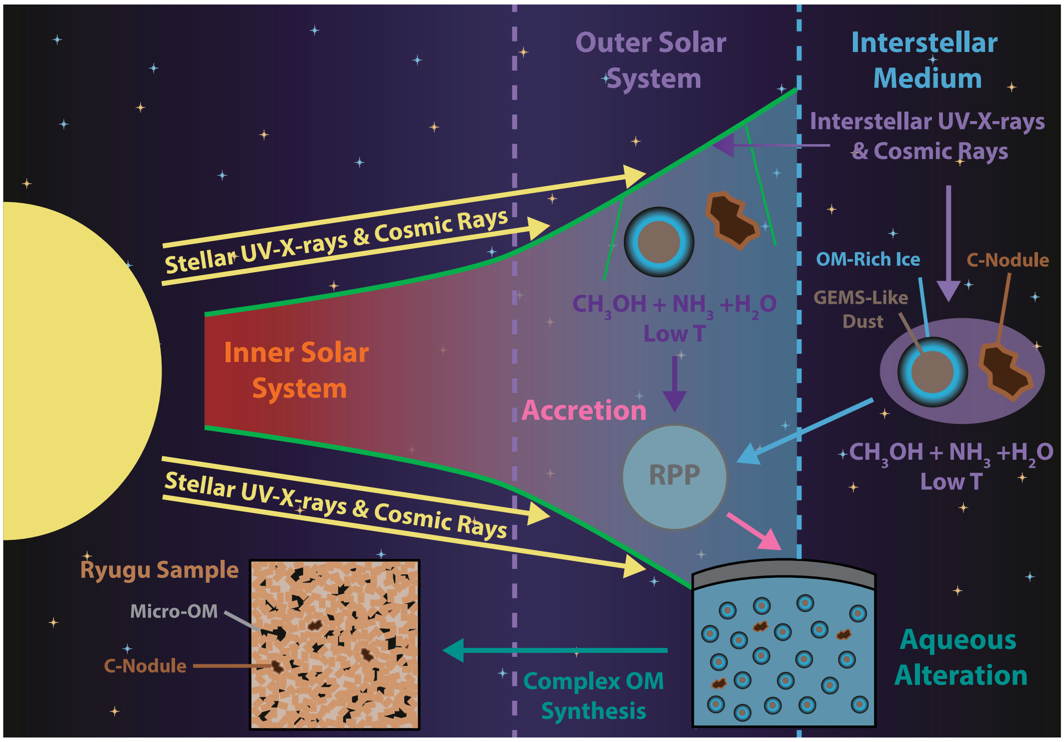

Fig. 24. The origin and evolution of OM within Ryugu particles. UV-X-rays from the protosun interact with the surface of the PSN. In the outer PSN temperatures are low enough for water, ammonia and simple organic molecules, such as methanol, to condense and form ices on dust grains. The ice mixtures are then irradiated by both stellar and interstellar UV-X-rays and also by galactic and solar cosmic rays, producing both SOM and IOM. A similar mechanism can also form OM in the ISM, but through only interstellar UV-X-rays and galactic cosmic rays. Carbonaceous nodules (C-nodule) could be formed through aggregation of dust and OM. All the aforementioned organic components and their dust grain hosts, as well as the ice mixtures, could then be accreted into the Ryugu progenitor planetesimal (RPP). Heating from the decay of ^{26}Al would then melt the ice to yield water-rich fluids that in turn initiate aqueous alteration. During aqueous alteration a variety of organic syntheses, such as formose, condensation, Michael addition, hydrolysis and carbonisation reactions and Strecker and Chichiban synthesis, would yield complex SOM and IOM. In combination the above processes can explain the variation in the types of OM present within Ryugu, as well as their isotopic composition.

in either the initial OM accreted by Orgueil and Ryugu or the processes operating in the regions of their progenitor bodies where these extraterrestrial samples originated. If the latter is the case, then significant differences in either the initial reactants, mineral catalysts, thermodynamic conditions and/or chemistry of the aqueous media are necessary to explain the observed differences between the Ryugu particles and Orgueil DESI-OT-MS responses. Both the bulk mineralogy and petrology reported here for Ryugu is similar to that of Orgueil and so it is unlikely that the differences arise from phenomena simply related to mineral-organic interactions. Instead, either the initial organic reservoirs or fluid properties, such as temperature and composition, may be responsible. It is also possible that non-indigenous material could have been introduced via small impacts and these may have contributed to the SOM of the Ryugu particles. Nevertheless, the particles from the TD2 site, such as C0008, likely represent material that was buried and so it not clear whether external material could have contributed to the SOM inventory of these particles.

The distribution of SOM observed through DESI-OT-MS demonstrates that different types of SOM are negatively correlated, with some appearing in one part of the sample, while other SOM components appear in other parts (separated by 10's to 100's of µm). Furthermore, certain SOM show high-intensity areas that are 10's to 100's of µm in size. The SOM high-intensity areas represent regions where the SOM is more abundant and may thus represent either sites of OM accretion or formation. The SOM could have been originally housed within the ice mantles of ISM or PSN dust grains, with the more water-soluble SOM being transported into the matrix and the less soluble SOM remaining closer to the point of accretion and forming the high-intensity areas.[78] Such differences in the concentration or type of SOM present within fluids, from different areas of the matrix of Ryugu, may also be able to explain the differences in the number of facets of framboidal magnetite that formed during aqueous alteration.[25] Alternatively, simple organic compounds or polycyclic aromatic hydrocarbons (PAHs) inherited from OM-bearing ice could have reacted with H_2, generated by the alteration of primary phases to secondary ones, to yield more complex OM,[154],[155] including the homologues recorded here. Such reactions could be heavily influenced by mineral catalysts, with later reactions being potentially mediated by the phyllosilicates generated during alteration.[156]

Amino acids. Ryugu particle C0008-15 contains a diverse array of both α- and β-amino acids, which demonstrate both similarities and differences to those measured for Orgueil by this study. The proteinogenic essential amino acids, valine leucine, isoleucine, threonine and phenylalanine and the non-essential proteinogenic amino acids glycine, alanine (likely), serine, aspartic acid, glutamic acid, proline and hydroxyproline[157],[158] were observed for both Ryugu and Orgueil, with Orgueil additionally having the non-essential amino acid Tyrosine. Such a finding is significant, because some doubt has been cast on the indigeneity of proteinogenic amino acids, due to terrestrial contamination being plausible in falls and finds alike, which have most certainly been in contact with the Earths biosphere.[159],[160] The discovery of proteinogenic amino acids, in conjunction with N-heterocycles, significantly above background levels is proof that Ryugu and thus other extraterrestrial materials can provide organic molecules essential for the origin of life on Earth. Furthermore, such a discovery highlights the importance of sample return missions in providing un-contaminated extraterrestrial materials to Earth, which can allow for an investigation and reassessment of contamination within meteorite samples.

The UV processing of outer PSN/ISM composition ices has produced simple amino acids, such as glycine, alanine and β-alanine (all present in C0008-15) at carbonaceous chondrite like abundances.[161] However, more complex arrays of α- and β-amino acids, such as some of those found in C0008-15, are thought to form during parent body aqueous alteration through Strecker type synthesis involving ammonia, aldehydes and ketones,[162] and via Michael addition of ammonia to α,β-unsaturated nitriles, with subsequent hydrolysis,[163] respectively. More recently, it was shown that a variety of α-, β- and γ-amino acids could be formed from comet-like ice compositions involving formose, condensation and carbonization style reactions on an extraterrestrial parent body.[116] As such, a significant proportion of the amino acids in C0008-15 likely formed during aqueous alteration on the Ryugu progenitor body. A similar interpretation can be drawn for Orgueil, which has been previously proposed to originate from a comet-like body, due to the strikingly distinct amino acid composition to that of CM meteorites.[164]

Furthermore, a cometary/interstellar ice analogue compound hexamethylenetetramine (HMT) was shown to react to form similar types of amino acids to those produced previously during hydrothermal experiments[116] and the types of amino acids were found to be dependent on the presence of certain types of phyllosilicates.[156] Fe-rich smectites hampered the production of amino acids, whereas Al-rich smectites enhanced them. Such a finding is of particular interest to this study, because Ryugu and Orgueil phyllosilicates are composed of an Al-rich rather than Fe-rich smectite composition. Therefore, the interaction between fluids and Al-rich smectites may be a very important factor for defining the amino acids formed on the progenitor body of Ryugu and the Orgueil parent body.

The β-alanine/glycine absolute intensity ratio is also similar between Ryugu particle C0008 (2.94) and Orgueil (4.02). Furthermore, whilst this study does not quantify the detected amino acid concentrations, the intensity ratios reported here for Ryugu and Orgueil are much more similar to those concentration ratios reported for Orgueil (2.90[164] and 3.16[165]) than for Murchison (0.43[164] and 0.41[165]). Accordingly, the distribution of amino acids within carbonaceous chondrites has been shown to differ with respect to their petrographic type. β-alanine for example contributes much more strongly to the amino acid inventories of more aqueously altered type 1 chondrites, than it does to the less aqueously altered types 2 and 3.[166],[167] It may be that α-amino acids are more readily destroyed by oxidation during high levels of aqueous alteration than β-amino acids, or that α-amino acids are more readily produced via Strecker synthesis in carbonaceous chondrites that have experienced lower levels of aqueous alteration.[167] Therefore, the β-alanine/glycine value for Ryugu is in agreement with the mineralogical and petrological results reported here, which indicate Ryugu is highly aqueously altered and similar to Orgueil.

Nevertheless, differences are apparent between C0008 and Orgueil, such as the overall lower responses for C0008 amino acids compared to Orgueil and the different ratios between certain amino acid isomers. Currently, it is unclear how amino acid compositions and distributions vary within the Orgueil parent body and Ryugu and as such the differences may be explainable by sample heterogeneity. However, in the context of the bulk O, Ca, and Cr isotopic compositions reported here (section 4.2.4), a possible reason for the differences between Ryugu and Orgueil amino acids could be the inclusion of different materials during their accretion. If the Ryugu progenitor body accreted ice components that were different from Orgueil, as indicated by the higher ^{18}O contribution to Ryugu, then the organic components may represent different compositions that have enabled a different amino acid abundance and distribution to those found in Orgueil. Nevertheless, previous studies have indicated that the sulfate veins present in Orgueil arise from terrestrial weathering and thus it has been suggested that this may have affected the O-isotope values of whole rock Orgueil.84)

Alternatively, fundamental differences in terms of thermodynamic parameters, such as temperature, could result in different yields of reaction products. Accordingly, one key difference between Orgueil and Ryugu discovered by this study, is the range in the temperature estimates for the fluids of these two bodies. A temperature range of 50–150 °C has been proposed for Orgueil,168) whereas the estimates for Ryugu reported here suggest a lower temperature range of 0–30 °C. Nevertheless, the temperature range calculated for Ryugu here, most likely represents that of the end of the heating that melted the water ice. As such, the peak temperature for Ryugu aqueous alteration is not currently known. However, if the aqueous alteration occurred at lower temperature, then this may be able to explain the difference in amino acid content and the ratios between isomers.

Another possible explanation for the differences in the amino acid abundances observed between C0008 and Orgueil could be related to the terrestrial contamination of Orgueil. As mentioned previously, Orgueil has experienced modification of its mineralogy via oxidation from terrestrial water. Such water could have altered the O isotopes and also introduced some amino acids. It may thus be the case that Orgueil records Ryugu-like amino acid abundances, but with an additional contribution from the Earth's biosphere.

5.3. On the formation of Ryugu. Hydrated extraterrestrial objects, such as C-type asteroids, carbonaceous chondrite meteorites and comets are thought to have accreted as planetesimals (or cometesimals) consisting of aggregates of dust and ice beyond the water ice snow line169),170) (Fig. 25). Evidence from the Ne isotopes and abundances reported here suggests that the Ryugu progenitor body would have accreted components that had already experienced the effects of irradiation, both solar and cosmogenic in nature. Furthermore, the H, Be, B, N, Ca and Cr characteristics of these components indicate that they would have come from multiple sources, likely including both ISM and PSN material. Radioactive heating would have then melted the ice in the parent bodies of meteorites and possibly the interiors of large (> several 10's of km sized) cometary bodies.141),170),171) Ryugu was found by this study to mostly consist of hydrated silicates and is thus likely to have also accreted as part of a larger (> several 10's of km sized) planetesimal with a significant proportion of ice. The accretion of the Ryugu progenitor planetesimal must have occurred early in the solar systems history (<2.6 Myr after CAI formation), due to the ^{53}Mn-^{53}Cr ages of carbonates. Subsequently, aqueous alteration on the Ryugu progenitor planetesimal would have generated the current mineral assemblage of Ryugu and originated/altered the OM components. Any proposed mechanism for how aqueous alteration occurred on the Ryugu progenitor planetesimal must be able to explain the textures observed within Ryugu particles, including the occurrence of framboidal magnetite and the distinctive massive domains surrounded by foliated phyllosilicates. Such features suggest that the Ryugu progenitor planetesimal was subject to series of freezing and thawing, potentially related to the presence of a migrating thermal boundary zone during cooling.

Whilst the action of water in Ryugu particles and type 1 and 2 chondrite samples is clear, the location at which the progenitor planetesimals of these objects accreted is not. Previously, the parent bodies of chondritic meteorites were thought to form within or near to the current day main belt due to the composition of the main belt seemingly recording a preserved water ice snowline.172) However, it is now known that the main belt is not a simple representation of anhydrous inner main belt S-type asteroids and hydrated outer main belt C-type asteroids, there is in fact substantial mixing of these types of bodies

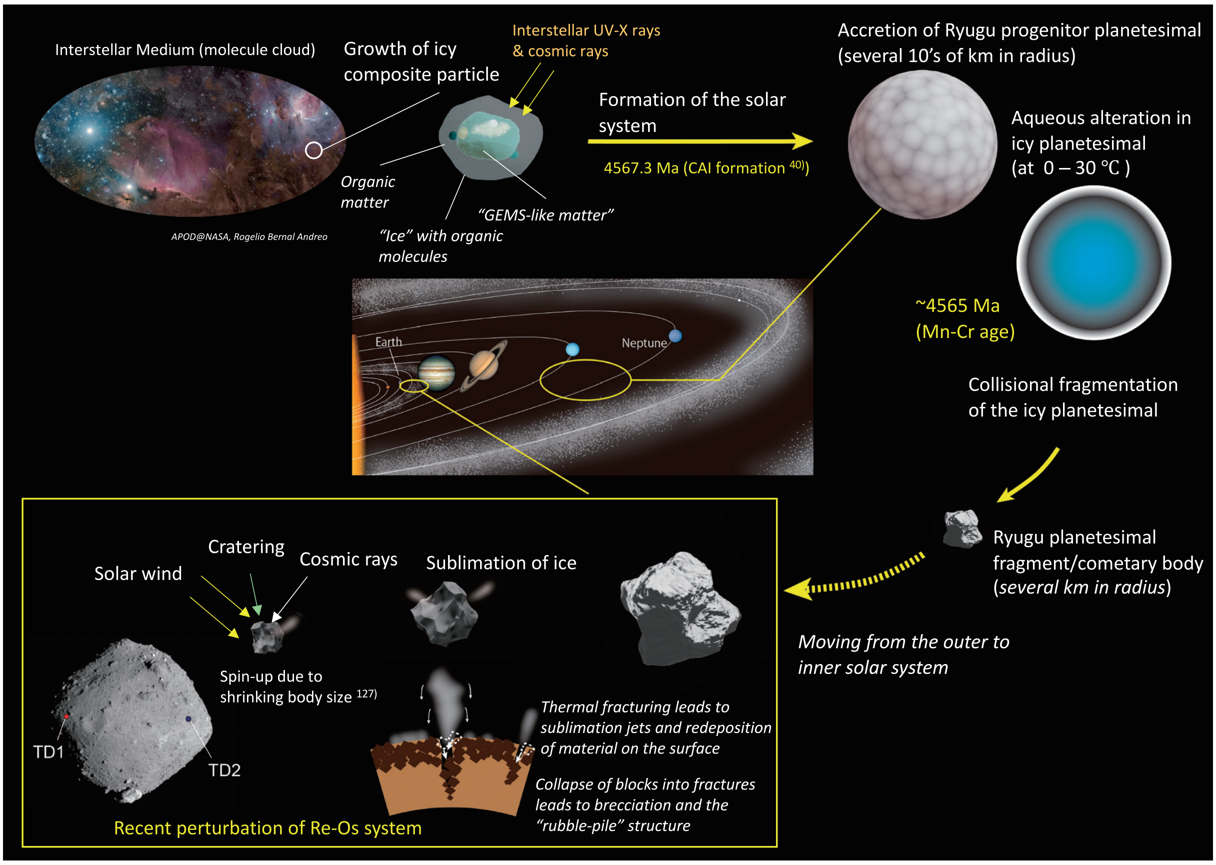

Fig. 25. The evolutional history of the asteroid Ryugu. The Ryugu progenitor body is thought to have been an icy planetesimal (several 10's of km in size) that may have formed in the trans-Neptunian region (TNR) through the accretion of icy particles. The accreted components record various origins, likely including both those in the ISM and PSN. The interior of the icy planetesimal melted due to the heat generated from radioactive decay of mainly ^{26}Al. As a result, rocky materials that were accreted with the icy particles underwent aqueous alteration (~4565 Ma). As the heat from radiative decay decreased, the icy planetesimal was again frozen. Although the timing is unknown, the icy planetesimal was fragmented, forming a cometary body, which represents the precursor of the asteroid Ryugu. Subsequently, as a result of solar system dynamics, the cometary body moved into the interior of the solar system. Due to the sublimation of ice caused by solar radiation, the cometary body gradually decreased in size. Thermal fracturing and sublimation jets, as well as the dynamics associated with the spin up of the body, led to the brecciation of rocky material and re-accumulation of dust at the surface of the body. The accumulated dust was then sintered in place, forming layers that would become the slab like material at the TD1 site. After the complete sublimation of ice from the surface of the body, the current day Ryugu was formed.

throughout the main belt.172) Accordingly, studies have proposed a non-*in situ* origin for primitive meteorite parent bodies, potentially within the outer solar system beyond the main belt.173)–176) Indeed, several studies have argued for a cometary origin of the Orgueil (CI1),138),164),177) as well as the OSIRIS-REx target asteroid, Bennu.132)

The formation location of the Ryugu progenitor planetesimal is thus unknown and could have been close to or far away from the current day position of the main belt. As such, here we will discuss several potential origins for Ryugu based on the results reported here and current theories of solar system geochemistry and dynamics. The widely accepted formation hypothesis for Ryugu5) suggests that it was formed as the result of catastrophic collision, presumably within the main belt between asteroidal bodies.11),12) The re-accreted material would have then formed a rubble pile asteroid that became deformed to yield a spinning top shape, as a result of the high rotation rate imparted during the collision or possibly due to the Yarkovsky-O'Keefe-Radzievskii-Paddack (YORP) effect.9),178) In such a scenario, the Ryugu progenitor planetesimal would have likely been disrupted to yield smaller asteroidal bodies, which in turn could either reaccumulate to yield current day Ryugu or themselves be disrupted later to form Ryugu.

Nevertheless, the Ryugu progenitor planetesimal could itself have been formed elsewhere and moved by the dynamical forces associated with either Nice[179)–181)] or Grand tack style models.[173),182)] If the Ryugu progenitor planetesimal did form further out than the main belt it could have accreted significant abundances of ice, as the hydrated mineral phases and abundance of voids suggest, and primitive organic and inorganic phases. After aqueous alteration, the icy Ryugu progenitor planetesimal could have been either catastrophically disrupted in the outer solar system or implanted into the main belt. The implantation of the Ryugu progenitor planetesimal into the main belt, could have occurred in a similar fashion to the implantation of trans-Neptunian objects[183)] or even potentially main belt comets.[175),184)] Subsequently, the planetesimal could have been disrupted to give Ryugu in a similar way to that proposed above.

Another possibility is that the Ryugu progenitor planetesimal accreted much further out than the main belt, within the trans-Neptunian disk.[175),184)] The body could have then been catastrophically or sub-catastrophically disrupted to yield comet-like material[185),186)] (Fig. 25). A recent model proposed that a fragment of several km in diameter would be sufficient to explain the features of current day Ryugu.[127)] Such material could have then been dispersed into either the Oort cloud or Kuiper belt where it remained until far more recently. Alternatively, the disrupted material or planetesimal itself could have been implanted into the main belt, thus representing a main belt comet-like object. A cometary Ryugu progenitor could have then been ejected from either the Oort cloud, Kuiper belt or main belt and evolved into a near earth orbit where the increased solar flux would have led to the sublimation of surface ice and the possible production of fractures associated with thermal stress.[134)] Such fractures are likely the source of some of the jets emanating from cometary surfaces, which are formed of water vapor, other volatiles, and dust.[134),135)] While a portion of the jet material is lost to space, some are redeposited onto the surface and are likely sintered (fixed in place) by the refreezing of volatiles.[136)] Accordingly, the sourcing of particles from multiple depths of this fragment of the Ryugu progenitor planetesimal for TD1 particles, but not TD2 particles, could explain the geochemical differences between the two sets of particles. The TD2 particles could instead have been eventually deposited simply by sublimation (similar to freeze drying), without the effects of the jets, when the ice was lost from the surface of Ryugu. If such a process took place on a cometary or comet-like Ryugu planetesimal fragment (Fig. 25) then the fracturing process could have led to the collapse of blocks into the space left behind, thus brecciating the material. Furthermore, any exogenous material picked-up, as the body passed through the aftermaths of catastrophic collisions within the inner solar system, could be deposited into the fractures or incorporated into the sintered layers of dust and ice. In this way, both the rubble pile structure and the implantation of exogenous materials, such as the unaltered olivine grains, and possibly the carbonaceous nodule in C0053 and the massive domain in A0035, observed within Ryugu, can be explained.

Furthermore, sublimation of ice would cause the cometary nucleus to shrink and the moment of inertia to decrease, resulting in the spin-up of the cometary nucleus.[187)] Once a fast enough rotation speed was acquired, the spinning top-shape of Ryugu could be formed through deformation related to the high centrifugal force.[127)] Subsequently, repeated exposure to solar radiation would lead to the complete sublimation of ice at the surface of Ryugu, leaving the iceless surface observed today. Once exposed, the surface materials of Ryugu could be affected by solar wind and solar cosmic ray irradiation, as evidenced by the albedo of Ryugu and the Raman responses of OM in the Ryugu particles reported here. Such a scenario could support studies that have proposed a cometary origin for Orgueil,[138),164),177)] since Orgueil has many similarities in terms of its petrography, mineralogy, geochemistry, and OM to the Ryugu particles. Moreover, the cometary origin for Ryugu outlined here explains how the fragment of an icy planetesimal, which would evolve into Ryugu, lost its ice and volatile components. Such a process is important, because many volatile enriched bodies still remain in the main belt today, as indicated by the presence of the main belt comets. Furthermore, there is strong evidence that some carbonaceous chondrites experienced fluid flow within the past 1 Myr (as recently as 0.1 Myr), with the fluid mobilization ages in some cases being after they were ejected from their parent bodies.[188)] Similarly, the Chelyabinsk meteorite also records the effects of recent aqueous alteration, possibly between a comet nucleus and a LL6 OC.[189)]

6. Conclusions

This study includes the observations and interpretations from a comprehensive analysis of 16 representative particles, undertaken at the P2C-PML, returned from the C-type asteroid Ryugu. The conclusions are outlined below.

Petrography: The Ryugu particle is composed of 50% matrix and 9% coarse-grained components, with an average porosity of 41%. The matrix is predominantly composed of phyllosilicate minerals with minor amounts of OM and Fe-sulfide, carbonate, and phosphate minerals. The coarse-grained components include grains of olivine, low-Ca pyroxene, and phosphate, and mono-phase or poly-phase nodular aggregates of phyllosilicates, carbonate, phosphate, Fe-sulfide, and magnetite, and OM. The olivine and low-Ca pyroxenes, and possibly one carbonaceous nodule and massive domain, were found to be exogeneous materials, incorporated after aqueous alteration. The average values of the bulk density and grain densities of Ryugu particles are $1528 \pm 242\,\mathrm{kg\,m^{-3}}$ and $2594 \pm 32\,\mathrm{kg\,m^{-3}}$ (1SD), respectively.

Temperature and Mn-Cr age: Oxygen isotope thermometry of magnetite-dolomite pairs yielded temperature estimates of 20^{+14}_{-12} and 9^{+15}_{-13} °C for the examined TD1 and TD2 particles, respectively. The ^{53}Mn-^{53}Cr age of dolomite estimated by those in TD1 and TD2 particles was $2.6^{+1.0}_{-0.8}$ Myr after formation of CAI.

Neon: The Ryugu particles contain Ne that was inherited from their accreted components and which in turn was likely affected by aqueous alteration. The particles also record Ne that was implanted more recently. As such it was not possible to distinguish between these two sources of Ne and estimate reliable CRE ages.

Elemental abundances: The abundances of the elements in Ryugu particles are in close agreement with the composition of CI chondrites, for three out of seven TD1 particles and all TD2 particles. For the remaining four TD1 particles, elemental fractionation of lithophile elements, which are compatible in the phosphate minerals, and B were observed. Aqueous alteration in the Ryugu progenitor planetesimal resulted in elemental fractionation beyond the sample size at the TD1 site but not at the TD2 site. Thus, elemental abundances of TD2 particles would represent the least modified bulk composition of Ryugu. Furthermore, the B and Be abundances of TD2 particles are likely to represent the involvement of two end-member components, with one of these components representing PSN material that has undergone the least thermal processing.

H-C-N isotopes: The multi-scale δD, δ^{13}C and δ^{15}N measurements revealed that IOM compatible with both PSN and ISM origins is present in the Ryugu particles. Most of the abundances of H, C, and N and their isotopic compositions, measured for bulk particles, are within the ranges of carbonaceous chondrites. The variation of δD, δ^{13}C and δ^{15}N for bulk compositions were largely controlled by the abundance of IOM, in particular for those identified as ^{15}N-hotspots and ^{15}N-coldspots. The δD, δ^{13}C, and δ^{15}N values of ^{15}N-hotspots range up to ~3000‰, ~70‰ and ~1100‰, respectively. The δ^{13}C and δ^{15}N values of ^{15}N-coldspots range up to ~100‰ and down to ~−150‰, respectively. The δD value of the ^{15}N-coldspot is indistinguishable from that of the matrix. The ^{15}N-hotspots that are also enriched in D could have inherited their OM from the ISM. Nevertheless, photodissociation of N_2 in the outer PSN cannot be precluded. Meanwhile, ^{15}N-coldspots may be derived from the outer PSN or ISM and as such multiple origins for OM in Ryugu are plausible.

Cr-Ca-O isotopes: Bulk O-Ca-Cr isotopic compositions of the Ryugu particles yielded as $\delta^{18}\mathrm{O} = 17.72$–20.08‰, $\Delta^{17}\mathrm{O} = 0.503$–0.614‰, $\varepsilon^{54}\mathrm{Cr} = 1.49$ and 1.77, and $\varepsilon^{48}\mathrm{Ca} = 1.97$ and 2.21. These data mostly resemble the CI chondrites out of all known meteorite groups, but show higher δ^{18}O, Δ^{17}O, and ε^{54}Cr values than those of CI chondrites. These isotopic data suggest that Ryugu sampled the most primitive and least-thermally processed PSN reservoir(s) and indicate that there was minimal involvement from thermally processed inner PSN components. Moreover, evidence that higher amounts of ^{18}O-enriched CO or CO_2 were incorporated into one Ryugu particle, suggests heterogeneity among the δ^{18}O values of the icy components accreted by the Ryugu progenitor planetesimal.

Surface evolution of OM: TD1 and TD2 site OM record differences in their Raman parameters that are indicative of a higher exposure to solar irradiation for TD1 particles. Furthermore, the isolated IOM of a TD1 and TD2 particle record differences in the intensity of their CH_X stretching responses and CH_2/CH_3 ratio that suggest solar irradiation has affected the TD1 particle, but not the TD2 particle. Such observations are in agreement with a higher pixel density and number of SOM homologues being recorded for a TD2 particle, compared to a TD1 particle, via DESI-OT-MS. As such, the OM of TD2 particles is considered to record a more primitive composition, having escaped the effects of solar weathering, compared to that in TD1 particles. This is in line with TD2 particles being sourced from the subsurface and TD1 particles from the immediate surface of current day Ryugu.

Evolution of OM on the Ryugu progenitor planetesimal: The presence of abundant amino acids, including complex α- and β-amino acids, indicates the synthesis of these amino acids on the Ryugu progenitor planetesimal through Strecker synthesis (α-amino acids) and Michael addition of ammonia to unsaturated nitriles, with subsequent hydrolysis. Amino acid synthesis may have also been mediated by the interaction between the Al-rich smectites found in Ryugu particles, as these phyllosilicates were found to improve amino acid yields in laboratory experiments. The presence of abundant proteinogenic amino acids supports the theory that the ingredients essential for the origin of life on Earth could have been sourced from extraterrestrial materials and an indigenous origin for such amino acids in meteorites. Nevertheless, some contribution of amino acids from the Earth's biosphere to Orgueil (CI1) may explain its higher abundance of amino acids compared to Ryugu. Furthermore, the presence of abundant N-containing SOM, most likely N-heterocyles, suggests that Fischer-Tropsch type synthesis of OM was a common process on the parent body of Ryugu. Aqueous alteration of anhydrous silicates to phyllosilicates would have produced H_2. Subsequently, chemical reactions involving H_2 and simple OM (such as formadehyde) could have led to the creation of more complex OM, including some IOM and SOM compounds.

Formation of Ryugu: The asteroid Ryugu was originally an icy body formed in the outer region of solar system <2.6 Myr after CAI formation and most likely the solar system. Exactly where Ryugu formed with respect to the current day main belt is unclear. However, the results reported here are compatible with an origin via a catastrophic collision that formed either a rubble pile asteroid through reaccumulation of the debris or a comet-like body that evolved through sublimation to yield a rubble pile asteroid. The latter is preferred here, due to the ability of the model to explain the loss of volatiles from the Ryugu progenitor body, the dynamical evolution of Ryugu into its current state and the geochemical, and petrological data reported here for Ryugu particles. Without the return of uncontaminated samples with known sample locations from the primitive asteroid Ryugu, the formulation of such a hypothesis would not have been possible.

Finally, the authors emphasize that the Ryugu particle datasets obtained by the application of the comprehensive analytical strategy reported here will enable a better understanding of the formation and evolution of Ryugu, from the nano to solar system scale and from the beginning of the solar system to the current day. From the results reported here it is also possible to draw clearer links between extraterrestrial organic matter and water and that of the Earth. Furthermore, it is our wish for the findings presented here to stimulate interdisciplinary discussion and cooperation, which will enable a better understanding of our solar system and beyond.

Acknowledgements

We are deeply indebted to Dr. Ikuo Kushiro, M.J.A. and Dr. Yoshio Fukao, M.J.A. for reviewing and handling this paper as Editors. We are also deeply grateful to the three anonymous reviewers who patiently reviewed such a long and wide-ranging paper, resulting in a significant improvement in the quality of the paper. We thank Drs. Noboru Nakamura, Akira Kouchi, Toshihiko Kadono, Eiichiro Kokubo and Tetsuo Yamamoto for discussions concerning the elemental abundances of chondrites, physical properties of ice, evolution of comets and the destruction processes of planetary materials. We acknowledge Drs. Zhao-Feng Zhang, Yongsheng He, and Shichun Huang for kindly arranging and providing the Ca standard. We also thank Dr. Ingo Leya for kindly providing advice on how to calculate cosmogenic Ne productivity. We would like to thank Takahiro Sato and Shinichi Kimura for designing the powder sample saucer on the microtome, making it possible to carry out our comprehensive geochemical analysis. We are grateful to Kayo Tanaka, Kazuyuki Tanaka, and Dr. Elena Kalinina for their technical assistance. This study was supported by the programs for "Promoting the Enhancement of Research Universities" and "National University Innovation Creation" to Okayama University by the MEXT and the Cabinet Office of Japan, respectively.

Finally, we would like to express our sincere gratitude to Okayama University Headquarters and the MEXT, for replacing many analytical facilities damaged by the earthquake that occurred on October 21, 2016 with the latest machines. Without such support, a comprehensive analysis of the Ryugu

samples presented in this paper would not have been possible.

Supplementary materials

Supplementary materials are available at https://doi.org/10.2183/pjab.98.015.

References

1) Kawaguchi, J., Uesugi, K. and Fujiwara, A. (2003) The MUSES-C mission for the sample and return—its technology development status and readiness. Acta Astronaut. **52**, 117–123.
2) Nakamura, E., Makishima, A., Moriguti, T., Kobayashi, K., Tanaka, R., Kunihiro, T. *et al.* (2012) Space environment of an asteroid preserved on micrograins returned by the Hayabusa spacecraft. Proc. Natl. Acad. Sci. U.S.A. **109**, E624–E629.
3) Tsuda, Y., Saiki, T., Terui, F., Nakazawa, S., Yoshikawa, M., Watanabe, S. *et al.* (2020) Hayabusa2 mission status: Landing, roving and cratering on asteroid Ryugu. Acta Astronaut. **171**, 42–54.
4) Kitazato, K., Milliken, R.E., Iwata, T., Abe, M., Ohtake, M., Matsuura, S. *et al.* (2019) The surface composition of asteroid 162173 Ryugu from Hayabusa2 near-infrared spectroscopy. Science **364**, eaav7432.
5) Sugita, S., Honda, R., Morota, T., Kameda, S., Sawada, H., Tatsumi, E. *et al.* (2019) The geomorphology, color, and thermal properties of Ryugu: Implications for parent-body processes. Science **364**, eaaw0422.
6) Potiszil, C., Tanaka, R., Kobayashi, K., Kunihiro, T. and Nakamura, E. (2020) The albedo of Ryugu: Evidence for a high organic abundance, as inferred from the Hayabusa2 touchdown maneuver. Astrobiology **20**, 916–921.
7) Yada, T., Abe, M., Okada, T., Nakato, A., Yogata, K., Miyazaki, A. *et al.* (2021) Preliminary analysis of the Hayabusa2 samples returned from C-type asteroid Ryugu. Nat. Astron. **6**, 214–220.
8) Watanabe, S., Tsuda, Y., Yoshikawa, M., Tanaka, S., Saiki, T. and Nakazawa, S. (2017) Hayabusa2 mission overview. Space Sci. Rev. **208**, 3–16.
9) Watanabe, S., Hirabayashi, M., Hirata, N., Hirata, N., Noguchi, R., Shimaki, Y. *et al.* (2019) Hayabusa2 arrives at the carbonaceous asteroid 162173 Ryugu—A spinning top–shaped rubble pile. Science **364**, 268–272.
10) Fujiwara, A., Kawaguchi, J., Yeomans, D.K., Abe, M., Mukai, T., Okada, T. *et al.* (2006) The rubble-pile asteroid Itokawa as observed by Hayabusa. Science **312**, 1330–1334.
11) Michel, P., Benz, W., Tanga, P. and Richardson, D.C. (2001) Collisions and gravitational reaccumulation: forming asteroid families and satellites. Science **294**, 1696–1700.
12) Walsh, K.J. (2018) Rubble pile asteroids. Annu. Rev. Astron. Astrophys. **56**, 593–624.
13) Morota, T., Sugita, S., Cho, Y., Kanamaru, M., Tatsumi, E., Sakatani, N. *et al.* (2020) Sample collection from asteroid (162173) Ryugu by Hayabusa2: Implications for surface evolution. Science **368**, 654–659.
14) Kokotanekova, R., Snodgrass, C., Lacerda, P., Green, S.F., Lowry, S.C., Fernandez, Y.R. *et al.* (2017) Rotation of cometary nuclei: new light curves and an update of the ensemble properties of Jupiter-family comets. Mon. Not. R. Astron. Soc. **471**, 2974–3007.
15) Saiki, T., Imamura, H., Arakawa, M., Wada, K., Takagi, Y., Hayakawa, M. *et al.* (2017) The small carry-on impactor (SCI) and the Hayabusa2 impact experiment. Space Sci. Rev. **208**, 165–186.
16) Arakawa, M., Saiki, T., Wada, K., Ogawa, K., Kadono, T., Shirai, K. *et al.* (2020) An artificial impact on the asteroid 162173 Ryugu formed a crater in the gravity-dominated regime. Science **368**, 67–71.
17) Saiki, T., Takei, Y., Mimasu, Y., Sawada, H., Ogawa, N., Ono, G. *et al.* (2020) Hayabusa2's kinetic impact experiment: Operational planning and results. Acta Astronaut. **175**, 362–374.
18) Kadono, T., Arakawa, M., Honda, R., Ishibashi, K., Ogawa, K., Sakatani, N. *et al.* (2020) Impact experiment on asteroid (162173) Ryugu: Structure beneath the impact point revealed by in situ observations of the ejecta curtain. Astrophys. J. Lett. **899**, L22.
19) Kikuchi, S., Saiki, T., Takei, Y., Terui, F., Ogawa, N., Mimasu, Y. *et al.* (2021) Hayabusa2 pinpoint touchdown near the artificial crater on Ryugu: Trajectory design and guidance performance. Adv. Space Res. **68**, 3093–3140.
20) Honda, R., Arakawa, M., Shimaki, Y., Shirai, K., Yokota, Y., Kadono, T. *et al.* (2021) Resurfacing processes on asteroid (162173) Ryugu caused by an artificial impact of Hayabusa2's Small Carry-on Impactor. Icarus **366**, 114530.
21) Arakawa, M., Wada, K., Saiki, T., Kadono, T., Takagi, Y., Shirai, K. *et al.* (2017) Scientific objectives of Small Carry-on Impactor (SCI) and Deployable Camera 3 Digital (DCAM3-D): Observation of an ejecta curtain and a crater formed on the surface of Ryugu by an artificial high-velocity impact. Space Sci. Rev. **208**, 187–212.
22) Alfing, J., Patzek, M. and Bischoff, A. (2019) Modal abundances of coarse-grained (>5 µm) components within CI-chondrites and their individual clasts—Mixing of various lithologies on the CI parent body(ies). Geochemistry **79**, 125532.
23) Chan, Q.H.S., Zolensky, M.E., Martinez, J.E., Tsuchiyama, A. and Miyake, A. (2016) Magnetite plaquettes are naturally asymmetric materials in meteorites. Am. Mineral. **101**, 2041–2050.
24) Kimura, Y., Sato, T., Nakamura, N., Nozawa, J., Nakamura, T., Tsukamoto, K. *et al.* (2013) Vortex magnetic structure in framboidal magnetite reveals existence of water droplets in an ancient asteroid. Nat. Commun. **4**, 2649.

25) Xu, Y.Y., Hao, H.Y., Liu, P., Wang, Q., Sun, Y.Q. and Zhang, G.Y. (2014) Facile synthesis, shape evolution and magnetic properties of polyhedral 50-facet Fe_3O_4 nanocrystals partially enclosed by {311} high-index planes. CrystEngComm **16**, 10451–10459.

26) Atencio, D., Chukanov, N.V., Nestola, F., Witzke, T., Coutinho, J.M.V., Zadov, A.E. *et al.* (2012) Mejillonesite, a new acid sodium, magnesium phosphate mineral, from Mejillones, Antofagasta, Chile. Am. Mineral. **97**, 19–25.

27) Ward, D., Bischoff, A., Roszjar, J., Berndt, J. and Whitehouse, M.J. (2017) Trace element inventory of meteoritic Ca-phosphates. Am. Mineral. **102**, 1856–1880.

28) Kunihiro, T., Ota, T. and Nakamura, E. (2019) Lithium- and oxygen-isotope compositions of chondrule constituents in the Allende meteorite. Geochim. Cosmochim. Acta **252**, 107–125.

29) Krot, A.N., Nagashima, K., Fintor, K. and Pal-Molnar, E. (2019) Evidence for oxygen-isotope exchange in refractory inclusions from Kaba (CV3.1) carbonaceous chondrite during fluid-rock interaction on the CV parent asteroid. Geochim. Cosmochim. Acta **246**, 419–435.

30) Macke, R.J., Consolmagno, G.J. and Britt, D.T. (2011) Density, porosity, and magnetic susceptibility of carbonaceous chondrites. Meteorit. Planet. Sci. **46**, 1842–1862.

31) Zolensky, M.E., Nakamura, K., Gounelle, M., Mikouchi, T., Kasama, T., Tachikawa, O. *et al.* (2002) Mineralogy of Tagish Lake: An ungrouped type 2 carbonaceous chondrite. Meteorit. Planet. Sci. **37**, 737–761.

32) Grott, M., Biele, J., Michel, P., Sugita, S., Schröder, S., Sakatani, N. *et al.* (2020) Macroporosity and grain density of rubble pile asteroid (162173) Ryugu. J. Geophys. Res. Planet. **125**, e2020JE006519.

33) Alexander, C.M.O., Fogel, M., Yabuta, H. and Cody, G.D. (2007) The origin and evolution of chondrites recorded in the elemental and isotopic compositions of their macromolecular organic matter. Geochim. Cosmochim. Acta **71**, 4380–4403.

34) Mahon, K.I. (1996) The new "York" regression: Application of an improved statistical method to geochemistry. Int. Geol. Rev. **38**, 293–303.

35) Lugmair, G.W. and Shukolyukov, A. (1998) Early solar system timescales according to ^{53}Mn-^{53}Cr systematics. Geochim. Cosmochim. Acta **62**, 2863–2886.

36) Glavin, D.P., Kubny, A., Jagoutz, E. and Lugmair, G.W. (2004) Mn-Cr isotope systematics of the D'Orbigny angrite. Meteorit. Planet. Sci. **39**, 693–700.

37) Honda, M. and Imamura, M. (1971) Half-life of Mn^{53}. Phys. Rev. C **4**, 1182–1188.

38) Amelin, Y. (2008) U–Pb ages of angrites. Geochim. Cosmochim. Acta **72**, 221–232.

39) Brennecka, G.A. and Wadhwa, M. (2012) Uranium isotope compositions of the basaltic angrite meteorites and the chronological implications for the early Solar System. Proc. Natl. Acad. Sci. U.S.A. **109**, 9299–9303.

40) Connelly, J.N., Bizzarro, M., Krot, A.N., Nordlund, Å., Wielandt, D. and Ivanova, M.A. (2012) The absolute chronology and thermal processing of solids in the solar protoplanetary disk. Science **338**, 651–655.

41) Fujiya, W., Sugiura, N., Sano, Y. and Hiyagon, H. (2013) Mn–Cr ages of dolomites in CI chondrites and the Tagish Lake ungrouped carbonaceous chondrite. Earth Planet. Sci. Lett. **362**, 130–142.

42) Visser, R., John, T., Whitehouse, M.J., Patzek, M. and Bischoff, A. (2020) A short-lived ^{26}Al induced hydrothermal alteration event in the outer solar system: Constraints from Mn/Cr ages of carbonates. Earth Planet. Sci. Lett. **547**, 116440.

43) Lodders, K. (2020) Solar elemental abundances. *In* The Oxford Research Encyclopedia of Planetary Science. Oxford University Press, https://doi.org/10.1093/acrefore/9780190647926.013.145.

44) Wood, B.J., Smythe, D.J. and Harrison, T. (2019) The condensation temperatures of the elements: A reappraisal. Am. Mineral. **104**, 844–856.

45) Phelan, N., Day, J.M.D., Dhaliwal, J.K., Liu, Y., Corder, C.A., Strom, C. *et al.* (2022) A ^{187}Re-^{187}Os, ^{87}Rb-^{87}Sr, highly siderophile and incompatible trace element study of some carbonaceous, ordinary and enstatite chondrite meteorites. Geochim. Cosmochim. Acta **318**, 19–54.

46) Zhou, X., Tanaka, R., Yamanaka, M., Sakaguchi, C. and Nakamura, E. (2019) A method to suppress isobaric and polyatomic Interferences for measurements of highly siderophile elements in desilicified geological samples. Geostand. Geoanal. Res. **43**, 611–633.

47) Day, J.M.D., Brandon, A.D. and Walker, R.J. (2016) Highly siderophile elements in Earth, Mars, the Moon, and asteroids. Rev. Mineral. Geochem. **81**, 161–238.

48) Smoliar, M.I., Walker, R.J. and Morgan, J.W. (1996) Re-Os ages of group IIA, IIIA, IVA, and IVB iron meteorites. Science **271**, 1099–1102.

49) Alexander, C.M.O.D., Bowden, R., Fogel, M.L., Howard, K.T., Herd, C.D.K. and Nittler, L.R. (2012) The provenances of asteroids, and their contributions to the volatile inventories of the terrestrial planets. Science **337**, 721–723.

50) Vacher, L.G., Piani, L., Rigaudier, T., Thomassin, D., Florin, G., Piralla, M. *et al.* (2020) Hydrogen in chondrites: Influence of parent body alteration and atmospheric contamination on primordial components. Geochim. Cosmochim. Acta **281**, 53–66.

51) Kerridge, J.F. (1985) Carbon, hydrogen and nitrogen in carbonaceous chondrites: Abundances and isotopic compositions in bulk samples. Geochim. Cosmochim. Acta **49**, 1707–1714.

52) King, A.J., Solomon, J.R., Schofield, P.F. and Russell, S.S. (2015) Characterising the CI and CI-like carbonaceous chondrites using thermogravimetric analysis and infrared spectroscopy. Earth

Planets Space **67**, 198.

53) Shimaki, Y., Senshu, H., Sakatani, N., Okada, T., Fukuhara, T., Tanaka, S. *et al.* (2020) Thermophysical properties of the surface of asteroid 162173 Ryugu: Infrared observations and thermal inertia mapping. Icarus **348**, 113835.

54) Jensen, S.S., Jørgensen, J.K., Kristensen, L.E., Furuya, K., Coutens, A., van Dishoeck, E.F. *et al.* (2019) ALMA observations of water deuteration: a physical diagnostic of the formation of protostars. Astron. Astrophys. **631**, A25.

55) Bonnand, P., Williams, H.M., Parkinson, I.J., Wood, B.J. and Halliday, A.N. (2016) Stable chromium isotopic composition of meteorites and metal–silicate experiments: Implications for fractionation during core formation. Earth Planet. Sci. Lett. **435**, 14–21.

56) Shukolyukov, A. and Lugmair, G.W. (2006) Manganese–chromium isotope systematics of carbonaceous chondrites. Earth Planet. Sci. Lett. **250**, 200–213.

57) Qin, L., Alexander, C.M.O.D., Carlson, R.W., Horan, M.F. and Yokoyama, T. (2010) Contributors to chromium isotope variation of meteorites. Geochim. Cosmochim. Acta **74**, 1122–1145.

58) Schoenberg, R., Merdian, A., Holmden, C., Kleinhanns, I.C., Haßler, K., Wille, M. *et al.* (2016) The stable Cr isotopic compositions of chondrites and silicate planetary reservoirs. Geochim. Cosmochim. Acta **183**, 14–30.

59) Huang, S. and Jacobsen, S.B. (2017) Calcium isotopic compositions of chondrites. Geochim. Cosmochim. Acta **201**, 364–376.

60) Dauphas, N., Chen, J.H., Zhang, J., Papanastassiou, D.A., Davis, A.M. and Travaglio, C. (2014) Calcium-48 isotopic anomalies in bulk chondrites and achondrites: Evidence for a uniform isotopic reservoir in the inner protoplanetary disk. Earth Planet. Sci. Lett. **407**, 96–108.

61) Schiller, M., Bizzarro, M. and Fernandes, V.A. (2018) Isotopic evolution of the protoplanetary disk and the building blocks of Earth and the Moon. Nature **555**, 507–510.

62) Nagao, K., Okazaki, R., Nakamura, T., Miura, Y.N., Osawa, T., Bajo, K. *et al.* (2011) Irradiation history of Itokawa regolith material deduced from noble gases in the Hayabusa samples. Science **333**, 1128–1131.

63) Heber, V.S., Wieler, R., Baur, H., Olinger, C., Friedmann, T.A. and Burnett, D.S. (2009) Noble gas composition of the solar wind as collected by the Genesis mission. Geochim. Cosmochim. Acta **73**, 7414–7432.

64) Black, D.C. (1972) On the origins of trapped helium, neon and argon isotopic variations in meteorite—II. Carbonaceous meteorites. Geochim. Cosmochim. Acta **36**, 377–394.

65) Jeffery, P.M. and Anders, E. (1970) Primordial noble gases in separated meteoritic minerals—I. Geochim. Cosmochim. Acta **34**, 1175–1198.

66) Mazor, E., Heymann, D. and Anders, E. (1970) Noble gases in carbonaceous chondrites. Geochim. Cosmochim. Acta **34**, 781–824.

67) Ferrari, A.C. and Robertson, J. (2000) Interpretation of Raman spectra of disordered and amorphous carbon. Phys. Rev. B **61**, 14095–14107.

68) Brunetto, R., Pino, T., Dartois, E., Cao, A.T., d'Hendecourt, L., Strazzulla, G. *et al.* (2009) Comparison of the Raman spectra of ion irradiated soot and collected extraterrestrial carbon. Icarus **200**, 323–337.

69) Quirico, E., Bonal, L., Beck, P., Alexander, C.M.O.D., Yabuta, H., Nakamura, T. *et al.* (2018) Prevalence and nature of heating processes in CM and C2-ungrouped chondrites as revealed by insoluble organic matter. Geochim. Cosmochim. Acta **241**, 17–37.

70) Potiszil, C., Montgomery, W. and Sephton, M.A. (2021) Heterogeneity within refractory organic matter from CM2 Carbonaceous Chondrites: Evidence from Raman spectroscopy. Earth Planet. Sci. Lett. **574**, 117149.

71) Socrates, G. (2004) Infrared and Raman Characteristic Group Frequencies: Tables and Charts, 3rd ed. Wiley, Chichester.

72) Kebukawa, Y., Alexander, C.M.O.D. and Cody, G.D. (2011) Compositional diversity in insoluble organic matter in type 1, 2 and 3 chondrites as detected by infrared spectroscopy. Geochim. Cosmochim. Acta **75**, 3530–3541.

73) Orthous-Daunay, F.R., Quirico, E., Beck, P., Brissaud, O., Dartois, E., Pino, T. *et al.* (2013) Mid-infrared study of the molecular structure variability of insoluble organic matter from primitive chondrites. Icarus **223**, 534–543.

74) Ehrenfreund, P., Robert, F., D'hendecourt, L. and Behar, F. (1991) Comparison of interstellar and meteoritic organic matter at 3.4 microns. Astron. Astrophys. **252**, 712–717.

75) Naraoka, H., Yamashita, Y., Yamaguchi, M. and Orthous-Daunay, F.-R. (2017) Molecular evolution of N-containing cyclic compounds in the parent body of the Murchison meteorite. ACS Earth Space Chem. **1**, 540–550.

76) Naraoka, H. and Hashiguchi, M. (2018) In situ organic compound analysis on a meteorite surface by desorption electrospray ionization coupled with an Orbitrap mass spectrometer. Rapid Commun. Mass Spectrom. **32**, 959–964.

77) Hashiguchi, M. and Naraoka, H. (2018) High-mass resolution molecular imaging of organic compounds on the surface of Murchison meteorite. Meteorit. Planet. Sci. **17**, 1–17.

78) Potiszil, C., Tanaka, R., Ota, T., Kunihiro, T., Kobayashi, K. and Nakamura, E. (2020) Concentration of meteoritic free organic matter by fluid transport and adsorption. Geochem. Perspect. Lett. **13**, 30–35.

79) Trinquier, A., Birck, J.-L. and Allègre, C.J. (2007) Widespread ^{54}Cr heterogeneity in the inner solar system. Astrophys. J. **655**, 1179–1185.

80) Warren, P.H. (2011) Stable-isotopic anomalies and the accretionary assemblage of the Earth and

Mars: A subordinate role for carbonaceous chondrites. Earth Planet. Sci. Lett. **311**, 93–100.

81) Yin, Q.-Z., Yamashita, K., Yamakawa, A., Tanaka, R., Jacobsen, B., Ebel, D. *et al.* (2009) ^{53}Mn-^{53}Cr systematics of Allende chondrules and epsilon ^{54}Cr-Δ^{17}O correlation in bulk carbonaceous chondrites. *In* Proceedings of 40th Lunar and Planetary Science Conference, 2009. The Woodlands, TX, Paper No. 2006.

82) Yurimoto, H. and Kuramoto, K. (2004) Molecular cloud origin for the oxygen isotope heterogeneity in the solar system. Science **305**, 1763–1766.

83) Lyons, J.R. and Young, E.D. (2005) CO self-shielding as the origin of oxygen isotope anomalies in the early solar nebula. Nature **435**, 317–320.

84) Airieau, S.A., Farquhar, J., Thiemens, M.H., Leshin, L.A., Bao, H. and Young, E. (2005) Planetesimal sulfate and aqueous alteration in CM and CI carbonaceous chondrites. Geochim. Cosmochim. Acta **69**, 4167–4172.

85) Meyer, B.S., Krishnan, T.D. and Clayton, D.D. (1996) ^{48}Ca Production in Matter Expanding from High Temperature and Density. Astrophys. J. **462**, 825–838.

86) Woosley, S.E., Heger, A. and Weaver, T.A. (2002) The evolution and explosion of massive stars. Rev. Mod. Phys. **74**, 1015–1071.

87) Schiller, M., Paton, C. and Bizzarro, M. (2015) Evidence for nucleosynthetic enrichment of the protosolar molecular cloud core by multiple supernova events. Geochim. Cosmochim. Acta **149**, 88–102.

88) Trinquier, A., Elliott, T., Ulfbeck, D., Coath, C., Krot, A.N. and Bizzarro, M. (2009) Origin of nucleosynthetic isotope heterogeneity in the solar protoplanetary disk. Science **324**, 374–376.

89) Alexander, C.M.O.D., Nittler, L.R., Davidson, J. and Ciesla, F.J. (2017) Measuring the level of interstellar inheritance in the solar protoplanetary disk. Meteorit. Planet. Sci. **52**, 1797–1821.

90) Sugiura, N. and Fujiya, W. (2014) Correlated accretion ages and ε^{54}Cr of meteorite parent bodies and the evolution of the solar nebula. Meteorit. Planet. Sci. **49**, 772–787.

91) Hezal, D.C., Russell, S.S., Ross, A.J. and Kersley, A.T. (2008) Modal abundances of CAIs: Implications for bulk chondrite element abundances and fractionations. Meteorit. Planet. Sci. **43**, 1879–1894.

92) Desch, S.J., Kalyaan, A. and Alexander, C.M.O.D. (2018) The effect of Jupiter's formation on the distribution of refractory elements and inclusions in meteorites. Astrophys J. Suppl. S. **238**, 11.

93) Prantzos, N. (2012) Production and evolution of Li, Be, and B isotopes in the Galaxy. Astron. Astrophys. **542**, A67.

94) Woosley, S.E., Hartmann, D.H., Hoffman, R.D. and Haxton, W.C. (1990) The ν-Process. Astrophys. J. **356**, 272–301.

95) Domogatskii, G.V., Eramzhian, R.A. and Nadezhin, D.K. (1978) Production of the light elements due to neutrinos emitted by collapsing stellar cores. Astrophys. Space Sci. **58**, 273–299.

96) Zhai, M., Nakamura, E., Shaw, D.M. and Nakano, T. (1996) Boron isotopic ratios in meteorites and lunar rocks. Geochim. Cosmochim. Acta **60**, 4877–4881.

97) Lambert, D.L., Sheffer, Y., Federman, S.R., Cardelli, J.A., Sofia, U.J. and Knauth, D.C. (1998) The ^{11}B/^{10}B ratio of local Interstellar Diffuse Clouds. Astrophys. J. **494**, 614–622.

98) Proffitt, C.R., Jonsson, P., Litzen, U., Pickering, J.C. and Wahlgren, G.M. (1999) Goddard high-resolution spectrograph observations of the B III resonance doublet in early B Stars: Abundances and Isotope Ratios. Astrophys. J. **516**, 342–348.

99) Chan, Q.H.S., Zolensky, M.E., Bodnar, R.J., Farley, C. and Cheung, J.C.H. (2017) Investigation of organo-carbonate associations in carbonaceous chondrites by Raman spectroscopy. Geochim. Cosmochim. Acta **201**, 392–409.

100) Alexander, C.M.O., Russell, S.S., Arden, J.W., Ash, R.D., Grady, M.M. and Pillinger, C.T. (1998) The origin of chondritic macromolecular organic matter: A carbon and nitrogen isotope study. Meteorit. Planet. Sci. **33**, 603–622.

101) Messenger, S. (2000) Identification of molecular-cloud material in interplanetary dust particles. Nature **404**, 968–971.

102) Rodgers, S.D. and Charnley, S.B. (2008) Nitrogen superfractionation in dense cloud cores. Mon. Not. R. Astron. Soc. **385**, L48–L52.

103) Rodgers, S.D. and Charnley, S.B. (2008) Nitrogen isotopic fractionation of interstellar nitriles. Astrophys. J. **689**, 1448–1455.

104) Bonal, L., Huss, G.R., Krot, A.N., Nagashima, K., Ishii, H.A. and Bradley, J.P. (2010) Highly ^{15}N-enriched chondritic clasts in the CB/CH-like meteorite Isheyevo. Geochim. Cosmochim. Acta **74**, 6590–6609.

105) Busemann, H., Young, A.F., Alexander, C.M.O., Hoppe, P., Mukhopadhyay, S. and Nittler, L.R. (2006) Interstellar chemistry recorded in organic matter from primitive meteorites. Science **312**, 727–730.

106) Floss, C., Stadermann, F.J., Bradley, J.P., Dai, Z.R., Bajt, S., Graham, G. *et al.* (2006) Identification of isotopically primitive interplanetary dust particles: A NanoSIMS isotopic imaging study. Geochim. Cosmochim. Acta **70**, 2371–2399.

107) Nakamura-Messenger, K., Messenger, S., Keller, L.P., Clemett, S.J. and Zolensky, M.E. (2006) Organic globules in the Tagish Lake meteorite: Remnants of the protosolar disk. Science **314**, 1439–1442.

108) van Kooten, E.M.M.E., Cavalcante, L.L., Nagashima, K., Kasama, T., Balogh, Z.I., Peeters, Z. *et al.* (2018) Isotope record of mineralogical changes in a spectrum of aqueously altered CM chondrites. Geochim. Cosmochim. Acta **237**, 79–102.

109) Aléon, J. (2010) Multiple origins of nitrogen isotopic anomalies in meteorites and comets. Astrophys. J.

722, 1342–1351.

110) Kuga, M., Marty, B., Marrocchi, Y. and Tissandier, L. (2015) Synthesis of refractory organic matter in the ionized gas phase of the solar nebula. Proc. Natl. Acad. Sci. U.S.A. **112**, 7129–7134.

111) Visser, R., Bruderer, S., Cazzoletti, P., Facchini, S., Heays, A.N. and van Dishoeck, E.F. (2018) Nitrogen isotope fractionation in protoplanetary disks. Astron. Astrophys. **615**, A75.

112) Chakraborty, S., Muskatel, B.H., Jackson, T.L., Ahmed, M., Levine, R.D. and Thiemens, M.H. (2014) Massive isotopic effect in vacuum UV photodissociation of N_2 and implications for meteorite data. Proc. Natl. Acad. Sci. U.S.A. **111**, 14704–14709.

113) Sephton, M.A., Verchovsky, A.B., Bland, P.A., Gilmour, I., Grady, M.M. and Wright, I.P. (2003) Investigating the variations in carbon and nitrogen isotopes in carbonaceous chondrites. Geochim. Cosmochim. Acta **67**, 2093–2108.

114) Sephton, M.A., Verchovsky, A.B. and Wright, I.P. (2004) Carbon and nitrogen isotope ratios in meteoritic organic matter: indicators of alteration processes on the parent asteroid. Int. J. Astrobiol. **3**, 221–227.

115) Bekaert, D.V., Derenne, S., Tissandier, L., Marrocchi, Y., Charnoz, S., Anquetil, C. *et al.* (2018) High-temperature ionization-induced synthesis of biologically relevant molecules in the protosolar nebula. Astrophys. J. **859**, 142.

116) Kebukawa, Y., Chan, Q.H.S., Tachibana, S., Kobayashi, K. and Zolensky, M.E. (2017) One-pot synthesis of amino acid precursors with insoluble organic matter in planetesimals with aqueous activity. Sci. Adv. **3**, e1602093.

117) Vinogradoff, V., Bernard, S., Le Guillou, C. and Remusat, L. (2018) Evolution of interstellar organic compounds under asteroidal hydrothermal conditions. Icarus **305**, 358–370.

118) Robert, F., Derenne, S., Lombardi, G., Hassouni, K., Michau, A., Reinhardt, P. *et al.* (2017) Hydrogen isotope fractionation in methane plasma. Proc. Natl. Acad. Sci. U.S.A. **114**, 870–874.

119) Furukawa, Y., Iwasa, Y. and Chikaraishi, Y. (2021) Synthesis of ^{13}C-enriched amino acids with ^{13}C-depleted insoluble organic matter in a formose-type reaction in the early solar system. Sci. Adv. **7**, eabd3575.

120) Le Guillou, C. and Brearley, A. (2014) Relationships between organics, water and early stages of aqueous alteration in the pristine CR3.0 chondrite MET 00426. Geochim. Cosmochim. Acta **131**, 344–367.

121) Le Guillou, C., Bernard, S., Brearley, A.J. and Remusat, L. (2014) Evolution of organic matter in Orgueil, Murchison and Renazzo during parent body aqueous alteration: In situ investigations. Geochim. Cosmochim. Acta **131**, 368–392.

122) Hamm, M., Pelivan, I., Grott, M. and de Wiljes, J. (2020) Thermophysical modelling and parameter estimation of small Solar system bodies via data assimilation. Mon. Not. R. Astron. Soc. **496**, 2776–2785.

123) Parkhurst, D.L. and Appelo, C.A.J. (2013) Description of input and examples for PHREEQC version 3: a computer program for speciation, batch-reaction, one-dimensional transport, and inverse geochemical calculations. USGS Techniques and Methods **6**, 497–519.

124) Ebel, D.S. (2006) Condensation of rocky material in astrophysical environments. *In* Meteorites and the Early Solar System II (eds. Lauretta, D.S. and McSween, H.Y.). The University of Arizona Press, Tucson, AZ, pp. 253–277.

125) Ebel, D.S. (2000) Variations on solar condensation: Sources of interstellar dust nuclei. J. Geophys. Res. Space **105**, 10363–10370.

126) Young, E.D., Zhang, K.K. and Schubert, G. (2003) Conditions for pore water convection within carbonaceous chondrite parent bodies — implications for planetesimal size and heat production. Earth Planet. Sci. Lett. **213**, 249–259.

127) Miura, H., Nakamura, E. and Kunihiro, T. (2022) The asteroid 162173 Ryugu: a cometary origin. Astrophys. J. Lett. **925**, L15.

128) Havishk, Potiszil, C., Tanaka, R. and Nakamura, E. (2022) The ice-organic-silicate contents of small solar system bodies: indicators for a comet to asteroid. Mon. Not. R. Astron. Soc. **513**, 3734–3741.

129) Binzel, R.P., Rivkin, A.S., Stuart, J.S., Harris, A.W., Bus, S.J. and Burbine, T.H. (2004) Observed spectral properties of near-Earth objects: results for population distribution, source regions, and space weathering processes. Icarus **170**, 259–294.

130) Bottke, W.F., Morbidelli, A., Jedicke, R., Petit, J.M., Levison, H.F., Michel, P. *et al.* (2002) Debiased orbital and absolute magnitude distribution of the near-earth objects. Icarus **156**, 399–433.

131) Gounelle, M., Spurny, P. and Bland, P.A. (2006) The orbit and atmospheric trajectory of the Orgueil meteorite from historical records. Meteorit. Planet. Sci. **41**, 135–150.

132) Nuth, J.A., Abreu, N., Ferguson, F.T., Glavin, D.P., Hergenrother, C., Hill, H.G.M. *et al.* (2020) Volatile-rich asteroids in the inner solar system. Planet. Sci. J. **1**, 82.

133) Whitman, K., Morbidelli, A. and Jedicke, R. (2006) The size-frequency distribution of dormant Jupiter family comets. Icarus **183**, 101–114.

134) Fornasier, S., Hoang, V.H., Hasselmann, P.H., Feller, C., Barucci, M.A., Deshapriya, J.D.P. *et al.* (2019) Linking surface morphology, composition, and activity on the nucleus of 67P/Churyumov-Gerasimenko. Astron. Astrophys. **630**, A7.

135) Syal, M.B., Schultz, P.H., Sunshine, J.M., A'Hearn, M.F., Farnham, T.L. and Dearborn, D.S.P. (2013) Geologic control of jet formation on Comet 103P/Hartley 2. Icarus **222**, 610–624.

136) Davidsson, B.J.R., Sierks, H., Guttler, C., Marzari, F., Pajola, M., Rickman, H. *et al.* (2016) The primordial nucleus of comet 67P/Churyumov-

Gerasimenko. Astron. Astrophys. **592**, A63.

137) Stephen Saunders, R., Fanale, F.P., Parker, T.J., Stephens, J.B. and Sutton, S. (1986) Properties of filamentary sublimation residues from dispersions of clay in ice. Icarus **66**, 94–104.

138) Gounelle, M. and Zolensky, M.E. (2014) The Orgueil meteorite: 150 years of history. Meteorit. Planet. Sci. **49**, 1769–1794.

139) Delbo, M., Libourel, G., Wilkerson, J., Murdoch, N., Michel, P., Ramesh, K.T. *et al.* (2014) Thermal fatigue as the origin of regolith on small asteroids. Nature **508**, 233–236.

140) Ostwald, W. (1897) Studies on the formation and transformation of solid bodies. Z. Phys. Chem. **22**, 289–330.

141) Wakita, S. and Sekiya, M. (2011) Thermal evolution of icy planetesimals in the solar nebula. Earth Planets Space **63**, 1193–1206.

142) Zandanel, A., Hellmann, R., Truche, L., Roddatis, V., Mermoux, M., Choblet, G. *et al.* (2022) Geologically rapid aqueous mineral alteration at subfreezing temperatures in icy worlds. Nat. Astron. https://doi.org/10.1038/s41550-022-01613-2.

143) Pepin, R.O., Becker, R.H. and Schlutter, D.J. (1999) Irradiation records in regolith materials. I: Isotopic compositions of solar-wind neon and argon in single lunar mineral grains. Geochim. Cosmochim. Acta **63**, 2145–2162.

144) McKay, D.S., Heiken, G., Basu, A., Blanford, G., Simon, S., Reedy, R. *et al.* (1991) The Lunar Regolith. *In* Lunar Sourcebook, A User's Guide to the Moon (eds. Heiken, G.H., Vaniman, D.T. and French, B.M.). Cambridge University Press, Cambridge, pp. 285–356.

145) Sandford, S.A., Allamandola, L.J., Tielens, A.G.G.M., Sellgren, K., Tapia, M. and Pendleton, Y. (1991) The interstellar C-H stretching band near 3.4 microns: constraints on the composition of organic material in the diffuse interstellar medium. Astrophys. J. **371**, 607.

146) Pendleton, Y., Sandford, S.A., Allamandola, L.J., Tielens, A. and Sellgren, K. (1994) Near-infrared absorption spectroscopy of interstellar hydrocarbon grains. Astrophys. J. **437**, 683.

147) Flynn, G.J., Keller, L.P., Feser, M., Wirick, S. and Jacobsen, C. (2003) The origin of organic matter in the solar system: evidence from the interplanetary dust particles. Geochim. Cosmochim. Acta **67**, 4791–4806.

148) Matrajt, G., Muñoz Caro, G.M., Dartois, E., d'Hendecourt, L., Deboffle, D. and Borg, J. (2005) FTIR analysis of the organics in IDPs: Comparison with the IR spectra of the diffuse interstellar medium. Astron. Astrophys. **433**, 979–995.

149) Muñoz Caro, G.M., Matrajt, G., Dartois, E., Nuevo, M., d'Hendecourt, L., Deboffle, D. *et al.* (2006) Nature and evolution of the dominant carbonaceous matter in interplanetary dust particles: effects of irradiation and identification with a type of amorphous carbon. Astron. Astrophys. **459**, 147–159.

150) Materese, C.K., Nuevo, M. and Sandford, S.A. (2015) N- and O-heterocycles produced from the irradiation of benzene and naphthalene in H_2O/NH_3-containing ices. Astrophys. J. **800**, 116.

151) Mahajan, T.B., Elsila, J.E., Deamer, D.W. and Zare, R.N. (2003) Formation of carbon-carbon bonds in the photochemical alkylation of polycyclic aromatic hydrocarbons. Orig. Life Evol. Biosph. **33**, 17–35.

152) Frank, R.L. and Seven, R.P. (1949) Pyridines. IV. A study of the chichibabin synthesis. J. Am. Chem. Soc. **71**, 2629–2635.

153) Stoks, P.G. and Schwartz, A.W. (1982) Basic nitrogen-heterocyclic compounds in the Murchison meteorite. Geochim. Cosmochim. Acta **46**, 309–315.

154) Shock, E.L. and Schulte, M.D. (1990) Amino-acid synthesis in carbonaceous meteorites by aqueous alteration of polycyclic aromatic hydrocarbons. Nature **343**, 728–731.

155) Schulte, M. and Shock, E. (2004) Coupled organic synthesis and mineral alteration on meteorite parent bodies. Meteorit. Planet. Sci. **39**, 1577–1590.

156) Vinogradoff, V., Remusat, L., McLain, H.L., Aponte, J.C., Bernard, S., Danger, G. *et al.* (2020) Impact of phyllosilicates on amino acid formation under asteroidal conditions. ACS Earth Space Chem. **4**, 1398–1407.

157) Ambrogelly, A., Palioura, S. and Söll, D. (2007) Natural expansion of the genetic code. Nat. Chem. Biol. **3**, 29–35.

158) Young, V.R. (1994) Adult amino acid requirements: The case for a major revision in current recommendations. J. Nutr. **124**, 1517S–1523S.

159) Sephton, M.A. and Hazen, R.M. (2013) On the origins of deep hydrocarbons. Rev. Mineral. Geochem. **75**, 449–465.

160) Burton, A.S., Stern, J.C., Elsila, J.E., Glavin, D.P. and Dworkin, J.P. (2012) Understanding prebiotic chemistry through the analysis of extraterrestrial amino acids and nucleobases in meteorites. Chem. Soc. Rev. **41**, 5459–5472.

161) Modica, P., Martins, Z., Meinert, C., Zanda, B. and d'Hendecourt, L.L.S. (2018) The amino acid distribution in laboratory analogs of extraterrestrial organic matter: A comparison to CM chondrites. Astrophys. J. **865**, 41.

162) Peltzer, E.T., Bada, J.L., Schlesinger, G. and Miller, S.L. (1984) The chemical conditions on the parent body of the Murchison meteorite: some conclusions based on amino, hydroxy and dicarboxylic acids. Adv. Space Res. **4**, 69–74.

163) Miller, S.L. (1957) The mechanism of synthesis of amino acids by electric discharges. Biochim. Biophys. Acta **23**, 480–489.

164) Ehrenfreund, P., Glavin, D.P., Botta, O., Cooper, G. and Bada, J.L. (2001) Extraterrestrial amino acids in Orgueil and Ivuna: Tracing the parent body of CI type carbonaceous chondrites. Proc. Natl. Acad. Sci. U.S.A. **98**, 2138–2141.

165) Glavin, D.P., Callahan, M.P., Dworkin, J.P. and Elsila, J.E. (2010) The effects of parent body processes on amino acids in carbonaceous chondrites. Meteorit. Planet. Sci. **45**, 1948–1972.

166) Glavin, D.P., Dworkin, J.P., Aubrey, A., Botta, O., Doty, J.H., III, Martins, Z. *et al.* (2006) Amino acid analyses of Antarctic CM2 meteorites using liquid chromatography-time of flight-mass spectrometry. Meteorit. Planet. Sci. **41**, 889–902.

167) Martins, Z., Modica, P., Zanda, B. and D'Hendecourt, L.L. (2015) The amino acid and hydrocarbon contents of the Paris meteorite: Insights into the most primitive CM chondrite. Meteorit. Planet. Sci. **50**, 926–943.

168) Glavin, D.P., Alexander, C.M.O.D., Aponte, J.C., Dworkin, J.P., Elsila, J.E. and Yabuta, H. (2018) The origin and evolution of organic matter in carbonaceous chondrites and links to their parent bodies. Chapter 3. *In* Primitive Meteorites and Asteroids (ed. Abreu, N.). Elsevier, Amsterdam, pp. 205–271.

169) Weissman, P.R. and Lowry, S.C. (2008) Structure and density of cometary nuclei. Meteorit. Planet. Sci. **43**, 1033–1047.

170) Trigo-Rodríguez, J.M., Rimola, A., Tanbakouei, S., Soto, V.C. and Lee, M. (2019) Accretion of water in carbonaceous chondrites: current evidence and implications for the delivery of water to early Earth. Space Sci. Rev. **215**, 18.

171) Prialnik, D. and Podolak, M. (1995) Radioactive heating of porous comet nuclei. Icarus **117**, 420–430.

172) DeMeo, F.E. and Carry, B. (2014) Solar System evolution from compositional mapping of the asteroid belt. Nature **505**, 629–634.

173) Walsh, K.J., Morbidelli, A., Raymond, S.N., O'Brien, D.P. and Mandell, A.M. (2012) Populating the asteroid belt from two parent source regions due to the migration of giant planets—"The Grand Tack". Meteorit. Planet. Sci. **47**, 1941–1947.

174) Raymond, S.N. and Izidoro, A. (2017) The empty primordial asteroid belt. Sci. Adv. **3**, e1701138.

175) Levison, H.F., Bottke, W.F., Gounelle, M., Morbidelli, A., Nesvorný, D. and Tsiganis, K. (2009) Contamination of the asteroid belt by primordial trans-Neptunian objects. Nature **460**, 364–366.

176) Tsuchiyama, A., Miyake, A., Okuzumi, S., Kitayama, A., Kawano, J., Uesugi, K. *et al.* (2021) Discovery of primitive CO_2-bearing fluid in an aqueously altered carbonaceous chondrite. Sci. Adv. **7**, eabg9707.

177) Gounelle, M., Morbidelli, A., Bland, P.A., Spurny, P., Young, E.D. and Sephton, M. (2008) Meteorites from the outer solar system? *In* The Solar System Beyond Neptune (eds. Barucci, M.A., Boehnhardt, H., Cruikshank, D.P., Morbidelli, A. and Dotson, R.). The University of Arizona Press, Tucson, AZ, pp. 525–541.

178) Michel, P., Ballouz, R.L., Barnouin, O.S., Jutzi, M., Walsh, K.J., May, B.H. *et al.* (2020) Collisional formation of top-shaped asteroids and implications for the origins of Ryugu and Bennu. Nat. Commun. **11**, 2655.

179) Gomes, R., Levison, H.F., Tsiganis, K. and Morbidelli, A. (2005) Origin of the cataclysmic Late Heavy Bombardment period of the terrestrial planets. Nature **435**, 466–469.

180) Tsiganis, K., Gomes, R., Morbidelli, A. and Levison, H.F. (2005) Origin of the orbital architecture of the giant planets of the Solar System. Nature **435**, 459–461.

181) Nesvorny, D. and Morbidelli, A. (2012) Statistical study of the early solar system's instability with four, five, and six giant planets. Astron. J. **144**, 117.

182) Walsh, K.J., Morbidelli, A., Raymond, S.N., O'Brien, D.P. and Mandell, A.M. (2011) A low mass for Mars from Jupiter's early gas-driven migration. Nature **475**, 206–209.

183) Hasegawa, S., Marsset, M., DeMeo, F.E., Bus, S.J., Geem, J., Ishiguro, M. *et al.* (2021) Discovery of two TNO-like bodies in the asteroid belt. Astrophys. J. Lett. **916**, L6.

184) Dones, L., Brasser, R., Kaib, N. and Rickman, H. (2015) Origin and evolution of the cometary reservoirs. Space Sci. Rev. **197**, 191–269.

185) Stern, S.A. and Weissman, P.R. (2001) Rapid collisional evolution of comets during the formation of the Oort cloud. Nature **409**, 589–591.

186) Morbidelli, A. and Rickman, H. (2015) Comets as collisional fragments of a primordial planetesimal disk. Astron. Astrophys. **583**, A43.

187) Watanabe, J. (1992) Ice-Skater model for the nucleus of comet Levy 1990c: Spin-up by a shrinking nucleus. Publ. Astron. Soc. Jpn. **44**, 163–166.

188) Turner, S., McGee, L., Humayun, M., Creech, J. and Zanda, B. (2021) Carbonaceous chondrite meteorites experienced fluid flow within the past million years. Science **371**, 164–167.

189) Nakamura, E., Kunihiro, T., Ota, T., Sakaguchi, C., Tanaka, R., Kitagawa, H. *et al.* (2019) Hypervelocity collision and water-rock interaction in space preserved in the Chelyabinsk ordinary chondrite. Proc. Jpn. Acad. Ser. B **95**, 165–177.

190) Clayton, R.N. and Mayeda, T.K. (1999) Oxygen isotope studies of carbonaceous chondrites. Geochim. Cosmochim. Acta **63**, 2089–2104.

191) Greenwood, R.C. and Franchi, I.A. (2004) Alteration and metamorphism of CO3 chondrites: evidence from oxygen and carbon isotopes. Meteorit. Planet. Sci. **39**, 1823–1838.

192) Greenwood, R.C., Franchi, I.A., Kearsley, A.T. and Alard, O. (2010) The relationship between CK and CV chondrites. Geochim. Cosmochim. Acta **74**, 1684–1705.

193) Brown, P.G., Hildebrand, A.R., Zolensky, M.E., Grady, M., Clayton, R.N., Mayeda, T.K. *et al.* (2000) The fall, recovery, orbit, and composition of the Tagish Lake meteorite: a new type of carbonaceous chondrite. Science **290**, 320–325.

194) Russell, S.D.J., Longstaffe, F.J., King, P.L. and

Larson, T.E. (2010) The oxygen-isotope composition of chondrules and isolated forsterite and olivine grains from the Tagish Lake carbonaceous chondrite. Geochim. Cosmochim. Acta **74**, 2484–2499.

195) Clayton, R.N., Onuma, N., Grossman, L. and Mayeda, T.K. (1983) Oxygen isotopic compositions of chondrules in Allende and ordinary chondrites. *In* Chondrules and Their Origins (ed. King, E.A.). Lunar and Planetary Institute, Houston, TX, pp. 37–43.

196) Rubin, A.E., Wasson, J.T., Clayton, R.N. and Mayeda, T.K. (1990) Oxygen isotopes in chondrules and coarse-grained chondrule rims from the Allende meteorite. Earth Planet. Sci. Lett. **96**, 247–255.

197) Tenner, T.J., Kimura, M. and Kita, N.T. (2017) Oxygen isotope characteristics of chondrules from the Yamato-82094 ungrouped carbonaceous chondrite: Further evidence for common O-isotope environments sampled among carbonaceous chondrites. Meteorit. Planet. Sci. **52**, 268–294.

198) Kunihiro, T., Rubin, A.E., McKeegan, K.D. and Wasson, J.T. (2004) Oxygen-isotopic compositions of relict and host grains in chondrules in the Yamato 81020 CO3.0 chondrite. Geochim. Cosmochim. Acta **68**, 3599–3606.

199) Scott, E.R.D. and Krot, A.N. (2014) 1.2 - Chondrites and Their Components. *In* Treatise on Geochemistry, Second Edition (eds. Holland, H.D. and Turekian, K.K.). Elsevier, Oxford, pp. 65–137.

200) Clayton, R.N., Onuma, N., Grossman, L. and Mayeda, T.K. (1977) Distribution of the pre-solar component in Allende and other carbonaceous chondrites. Earth Planet. Sci. Lett. **34**, 209–224.

201) Tanaka, R. and Nakamura, E. (2013) Determination of ^{17}O-excess of terrestrial silicate/oxide minerals with respect to Vienna Standard Mean Ocean Water (VSMOW). Rapid Commun. Mass Spectrom. **27**, 285–297.

202) De Gregorio, B.T., Stroud, R.M., Nittler, L.R., Alexander, C.M.O.D., Bassim, N.D., Cody, G.D. *et al.* (2013) Isotopic and chemical variation of organic nanoglobules in primitive meteorites. Meteorit. Planet. Sci. **48**, 904–928.

203) McKeegan, K.D., Aléon, J., Bradley, J., Brownlee, D., Busemann, H., Butterworth, A. *et al.* (2006) Isotopic compositions of cometary matter returned by Stardust. Science **314**, 1724–1728.

204) Alexander, C.M.O., Howard, K.T., Bowden, R. and Fogel, M.L. (2013) The classification of CM and CR chondrites using bulk H, C and N abundances and isotopic compositions. Geochim. Cosmochim. Acta **123**, 244–260.

205) Pearson, V.K., Sephton, M.A., Franchi, I.A., Gibson, J.M. and Gilmour, I. (2006) Carbon and nitrogen in carbonaceous chondrites: Elemental abundances and stable isotopic compositions. Meteorit. Planet. Sci. **41**, 1899–1918.

206) Grady, M.M., Verchovsky, A.B., Franchi, I.A., Wright, I.P. and Pillinger, C.T. (2002) Light element geochemistry of the Tagish Lake CI2 chondrite: Comparison with CI1 and CM2 meteorites. Meteorit. Planet. Sci. **37**, 713–735.

207) Harju, E.R., Rubin, A.E., Ahn, I., Choi, B.-G., Ziegler, K. and Wasson, J.T. (2014) Progressive aqueous alteration of CR carbonaceous chondrites. Geochim. Cosmochim. Acta **139**, 267–292.

208) Schrader, D.L., Nagashima, K., Krot, A.N., Ogliore, R.C. and Hellebrand, E. (2014) Variations in the O-isotope composition of gas during the formation of chondrules from the CR chondrites. Geochim. Cosmochim. Acta **132**, 50–74.

209) Clayton, R.N., Mayeda, T.K., Goswami, J.N. and Olsen, E.J. (1991) Oxygen isotope studies of ordinary chondrites. Geochim. Cosmochim. Acta **55**, 2317–2337.

210) Schulze, H., Bischoff, A., Palme, H., Spettel, B., Dreibus, G. and Otto, J. (1994) Mineralogy and chemistry of Rumuruti — the 1st meteorite fall of the new R chondrite group. Meteoritics **29**, 275–286.

211) McCanta, M.C., Treiman, A.H., Dyar, M.D., Alexander, C.M.O., Rumble, D. and Essene, E.J. (2008) The LaPaz Icefield 04840 meteorite: Mineralogy, metamorphism, and origin of an amphibole- and biotite-bearing R chondrite. Geochim. Cosmochim. Acta **72**, 5757–5780.

212) Greenwood, R.C., Franchi, I.A., Jambon, A. and Buchanan, P.C. (2005) Widespread magma oceans on asteroidal bodies in the early Solar System. Nature **435**, 916–918.

213) Scott, E.R.D., Greenwood, R.C., Franchi, I.A. and Sanders, I.S. (2009) Oxygen isotopic constraints on the origin and parent bodies of eucrites, diogenites, and howardites. Geochim. Cosmochim. Acta **73**, 5835–5853.

214) Wiechert, U.H., Halliday, A.N., Palme, H. and Rumble, D. (2004) Oxygen isotope evidence for rapid mixing of the HED meteorite parent body. Earth Planet. Sci. Lett. **221**, 373–382.

215) Franchi, I.A., Wright, I.P., Sexton, A.S. and Pillinger, C.T. (1999) The oxygen-isotopic composition of Earth and Mars. Meteorit. Planet. Sci. **34**, 657–661.

216) Newton, J., Franchi, I.A. and Pillinger, C.T. (2000) The oxygen-isotopic record in enstatite meteorites. Meteorit. Planet. Sci. **35**, 689–698.

217) Clayton, R.N. and Mayeda, T.K. (1996) Oxygen isotope studies of achondrites. Geochim. Cosmochim. Acta **60**, 1999–2017.

218) Greenwood, R.C., Franchi, I.A., Gibson, J.M. and Benedix, G.K. (2012) Oxygen isotope variation in primitive achondrites: The influence of primordial, asteroidal and terrestrial processes. Geochim. Cosmochim. Acta **94**, 146–163.

219) Tanaka, R., Potiszil, C. and Nakamura, E. (2021) Silicon and oxygen isotope evolution of the inner solar system. Planet. Sci. J. **2**, 102.

220) Greenwood, R.C., Burbine, T.H., Miller, M.F. and Franchi, I.A. (2017) Melting and differentiation of early-formed asteroids: The perspective from high precision oxygen isotope studies. Chem. Erde

77, 1–43.

221) Göpel, C., Birck, J.-L., Galy, A., Barrat, J.-A. and Zanda, B. (2015) Mn–Cr systematics in primitive meteorites: Insights from mineral separation and partial dissolution. Geochim. Cosmochim. Acta **156**, 1–24.

222) Zhu, K., Moynier, F., Schiller, M., Alexander, C.M.O.D., Barrat, J.-A., Bischoff, A. *et al.* (2021) Mass-independent and mass-dependent Cr isotopic composition of the Rumuruti (R) chondrites: Implications for their origin and planet formation. Geochim. Cosmochim. Acta **293**, 598–609.

223) Zhu, K., Liu, J., Moynier, F., Qin, L., Alexander, C.M.O.D. and He, Y. (2019) Chromium isotopic evidence for an early formation of chondrules from the Ornans CO chondrite. Astrophys. J. **873**, 82.

224) Larsen, K.K., Trinquier, A., Paton, C., Schiller, M., Wielandt, D., Ivanova, M.A. *et al.* (2011) Evidence for magnesium isotope heterogeneity in the solar protoplanetary disk. Astrophys. J. Lett. **735**, L37.

225) Zhu, K., Moynier, F., Schiller, M. and Bizzarro, M. (2020) Dating and tracing the origin of enstatite chondrite chondrules with Cr isotopes. Astrophys. J. **894**, L26.

226) Sanborn, M.E. and Yin, Q.Z. (2015) Investigating a common source for brachinites and Graves Nunataks 06128 and 06129 meteorites using high precision chromium isotopes. *In* Proceedings of 46th Lunar and Planetary Science Conference, 2015. The Woodlands, TX, Paper No. 2241.

227) Schmitz, B., Yin, Q.Z., Sanborn, M.E., Tassinari, M., Caplan, C.E. and Huss, G.R. (2016) A new type of solar-system material recovered from Ordovician marine limestone. Nat. Commun. **7**, ncomms11851.

228) Yamakawa, A., Yamashita, K., Makishima, A. and Nakamura, E. (2010) Chromium isotope systematics of achondrites: Chronology and isotopic heterogeneity of the inner solar system bodies. Astrophys. J. **720**, 150–154.

229) Petitat, M., Birck, J.L., Luu, T.H. and Gounelle, M. (2011) The chromium isotopic composition of the ungrouped carbonaceous chondrite Tagish Lake. Astrophys. J. **736**, 23.

230) Chen, H.-W., Lee, T., Lee, D.-C., Shen, J.J.-S. and Chen, J.-C. (2011) ^{48}Ca heterogeneity in differentiated meteorites. Astrophys. J. Lett. **743**, L23.

231) Ivanova, M.A., Krot, A.N., Nagashima, K. and MacPherson, G.J. (2012) Compound ultrarefractory CAI-bearing inclusions from CV3 carbonaceous chondrites. Meteorit. Planet. Sci. **47**, 2107–2127.

232) Bermingham, K.R., Gussone, N., Mezger, K. and Krause, J. (2018) Origins of mass-dependent and mass-independent Ca isotope variations in meteoritic components and meteorites. Geochim. Cosmochim. Acta **226**, 206–223.

233) Huang, S., Farkaš, J., Yu, G., Petaev, M.I. and Jacobsen, S.B. (2012) Calcium isotopic ratios and rare earth element abundances in refractory inclusions from the Allende CV3 chondrite. Geochim. Cosmochim. Acta **77**, 252–265.

234) Birck, J.-L. and Allègre, C.J. (1988) Manganese—chromium isotope systematics and the development of the early Solar System. Nature **331**, 579–584.

235) Bogdanovski, O., Papanastassiou, D. and Wasserburg, G. (2002) Cr isotopes in Allende Ca-Al-rich inclusions. *In* Proceedings of 33th Lunar and Planetary Science, 2002. Houston, TX, Paper No. 1802.

236) Warren, P.H. and Kallemeyn, G.W. (1992) Explosive volcanism and the graphite-oxygen fugacity buffer on the parent asteroid(s) of the ureilite meteorites. Icarus **100**, 110–126.

237) Leya, I., Neumann, S., Wieler, R. and Michel, R. (2001) The production of cosmogenic nuclides by galactic cosmic-ray particles for 2π exposure geometries. Meteorit. Planet. Sci. **36**, 1547–1561.

238) Trappitsch, R. and Leya, I. (2014) Depth-dependent solar cosmic ray induced cosmogenic production rates. *In* Proceedings of 45th Lunar and Planetary Science Conference, 2014. The Woodlands, TX, Paper No. 1894.

239) Smith, S.R.P., Huneke, J.C., Rajan, R.S. and Wasserburg, G.J. (1977) Neon and argon in the Allende meteorite. Geochim. Cosmochim. Acta **41**, 627–647.

240) Srinivasan, B., Lewis, R.S. and Anders, E. (1978) Noble gases in the Allende and Abee meteorites and a gas-rich mineral fraction: investigation by stepwise heating. Geochim. Cosmochim. Acta **42**, 183–198.

241) Ott, U., Mack, R. and Sherwood, C. (1981) Noble-gas-rich separates from the Allende meteorite. Geochim. Cosmochim. Acta **45**, 1751–1788.

242) Göbel, R., Begemann, F. and Ott, U. (1982) On neutron-induced and other noble gases in Allende inclusions. Geochim. Cosmochim. Acta **46**, 1777–1792.

243) Nakamura, T., Noguchi, T., Zolensky, M.E. and Tanaka, M. (2003) Mineralogy and noble-gas signatures of the carbonate-rich lithology of the Tagish Lake carbonaceous chondrite: evidence for an accretionary breccia. Earth Planet. Sci. Lett. **207**, 83–101.

244) Benkert, J., Baur, H., Signer, P. and Wieler, R. (1993) He, Ne, and Ar from the solar wind and solar energetic particles in lunar ilmenites and pyroxenes. J. Geophys. Res. Planet. **98**, 13147–13162.

245) Eberhardt, P., Eugster, O.J. and Marti, K. (1965) A redetermination of the isotopic composition of atmospheric neon. Z. Naturforsch. A **20**, 623–624.

(Received Jan. 31, 2022; accepted May 6, 2022)